Bijan Zahedi

Shipboard DC Hybrid Power Systems

Modeling, efficiency analysis and stability control

Thesis for the degree of Philosophiae Doctor

Trondheim, October 2014

Norwegian University of Science and Technology
Faculty of Information Technology, Mathematics and Electrical Engineering
Department of Electric Power Engineering

NTNU – Trondheim
Norwegian University of
Science and Technology

NTNU
Norwegian University of Science and Technology

Thesis for the degree of Philosophiae Doctor

Faculty of Information Technology, Mathematics and Electrical Engineering
Department of Electric Power Engineering

ISBN 978-82-326-0514-9 (printed ver.)
ISBN 978-82-326-0515-6 (electronic ver.)
ISSN 1503-8181

Doctoral theses at NTNU, 2014:301

Printed by NTNU-trykk

Acknowledgements

I would like to express my gratitude to my research supervisor, Prof. Lars E. Norum for giving me the opportunity to accomplish this research, and for all his supports throughout my PhD program. His industry-oriented attitude made possible several joint works with major industrial companies during the course of my studies, which conducted this research against main practical challenges in the subject. This project has been financially supported by the Research Council of Norway and Det Norske Veritas (DNV) through Project 179519, entitled "Integrated Marine Electrical Power and Control Systems." Helpful information and supports from Dr. Kristine L. Bruun from DNV is gratefully acknowledged.

I also wish to express my sincere appreciation to Prof. Babak Nahid-Mobarakeh for allowing me to do experiments in his lab at university of Lorraine, Nancy, France. His valuable advice and support made it possible to accomplish the stability studies of the project. I would like to thank Prof. Serge Pierfederici as well for the helpful discussions and advice during my stay in Nancy. My thanks also go to the PhD students and staff of university of Lorraine who supported me for both work-related and non-work-related matters during my visit.

My special thanks go to my friends and colleagues at Energy Conversion Group and Department of Power Engineering at NTNU for valuable discussions and enjoyable friendship. We had memorable social gatherings and group ski trips which I miss a lot. I also wish to particularly thank Hossein Farahmand for proof reading of this thesis.

I would like to thank my greatest friend whom I am sharing my life with, Zahra, my beloved wife. I am truly grateful for all her tender support, encouragement, and patience during the past years, and for her belief in me. I would also like to thank Nikan, my lovely son, for bringing joy in my life. Finally, my deepest sense of gratitude goes to my parents whose love is the most truthful feeling I have ever experienced. Without their support and sacrifices, nothing of who I am today could have been possible.

Abstract

DC hybrid power systems are currently of interest for ship commercial marine vessels to enable low-emission and fuel-efficient operation. The benefit of using these systems is also to provide space and weight savings onboard ships. However, a shipboard dc hybrid power system requires effective analysis tools to realize the advantages.

Modeling and simulation are essential tools to facilitate design, analysis, optimization, and control of the dc hybrid power systems. The standard power system simulators need excessive computation time to simulate the above power-electronic-based power distribution systems. The limiting factor in terms of computation time is the switching behavior of the power electronic converters, which requires extremely small time steps. In order to overcome this limitation, reduced-order converter models can be used to provide time-efficient simulations. The reduced-order models are used only when studying the exact switching behavior is not necessary. In this dissertation, appropriate modeling of the converters and other elements of a shipboard dc hybrid power system is presented. The derived models are used in the development of a simulator program for system-level analysis of all-electric ships.

Fuel saving is a major motivation in the development of commercial shipboard dc power systems with onboard energy storage. Analysis of fuel consumption and efficiency modeling enable investigation of fuel saving potentials. The system efficiency is analyzed by enhancing the simulator models through including the power loss components. An on-line control strategy is proposed that optimizes the fuel consumption of the multi-generator shipboard power system. The energy storage is a key element in development of the optimization control system.

The shipboard dc power systems may consist of several power electronic converters connecting sources and loads to the grid. The stability of such power electronic-based systems is an essential issue in both design and control due to potential negative incremental resistance introduced by power electronic converters. This property is a consequence of the converter behaving as an instantaneous Constant Power Load (CPL), which can drive the system to instability. Stability analysis and control of the shipboard dc grid is another main focus in this dissertation.

Contents

LIST OF ABBREVIATIONS

AC	Alternating Current
AGS	Active Global Stabilization
AH	Anchor Handling
AVM	Average Value Model
BP	Bullard Pull
CCM	Continuous Conduction Mode
CPL	Constant Power Load
DC	Direct Current
DE	Diesel Engine
DG	Diesel Generator
ESAC	Energy Systems Analysis Consortium
ESS	Energy Storage System
FCS	Fuel Cell System
GMPM	Gain Margin Phase Margin
GSSAM	Generalized State Space Average Model
H	Harbor
HDP	High Dynamic Positioning
HV	High Voltage
ICE	Internal Combustion Engine
LDP	Low Dynamic Positioning
Li	Lithium
LMI	Linear Matrix Inequality
LV	Low Voltage
M	Motor

NiMH	Nickel-Metal Hydride
NO_x	Mono-Nitrogen Oxides
OSV	Offshore Support Vessel
PAVM	Parametric Average Value Model
PI	Proportional Integral
PM	Particulate Matter
PMSG	Permanent Magnet Synchronous Generator
PMSM	Permanent Magnet Synchronous Motor
PWM	Pulse Width Modulation
RGS	Robust Global Stabilization
RESC	Root Exponential Stability Criterion
SC	Supercapacitor
SFC	Specific Fuel Consumption
SG	Synchronous Generator
SOC	State Of Charge
SO_x	Sulphur Oxide gasses
SSAVM	State Space Average Value Model
TS	Transit Supply
TT	Transit Towing
VSD	Variable Speed Drive
VSI	Voltage Source Inverter

NOMENCLATURE

a, b, C_0	Polynomial coefficients of fuel consumption relation
C	Capacitance
$C(t)$	Fuel consumption over time "t"
C_1	Hourly fuel consumption
C_C	Clamping capacitor
c_{Fe}	Iron loss coefficient of generator core
c_m	Mechanical loss coefficient of generator
C_O	Output capacitor of transistor switch
D	Design value of "Duty cycle"
d	Instantaneous "duty cycle"
d'	Complement of instantaneous duty ratio
D'_s	Complement of duty ratio of dc source
$d_{a,b,c}$	Switching functions of inverter
D_p	Propeller diameter
D_s	Duty ratio of dc source
F_1	Current waveform factor of rectifier
f_{sw}	Switching frequency of the dc-dc converter
H_c	Transfer function of the dc link capacitor
H_L	Transfer function of the dc link inductor
I, i	Current
$\mathbf{K}$	abc-to-dq transformation matrix
K_q	Propeller thrust coefficient
K_T	Propeller torque coefficient
K_Y	Engine torque constant

L	Inductance
m	Modulation index of PWM voltage source inverter
N	Number of engine cylinders
n	Transformer turns ratio
P,p	Power
Q_p	Propeller torque
R	Resistance
R_c	Equivalent resistance of generator core losses
R_{eq}	Power ripple equivalent
T	Filter time constant
T_c	Time period of an on-off cycle of dc source (charge-discharge cycle)
T_{ch}	Charge time period
T_{dis}	Discharge time period
T_{em}	Electromagnetic torque
T_m	Engine mechanical torque
T_p	Propeller thrust
V, v	Voltage
V_A	Propeller advance velocity
V_{fw}	Forward voltage of diode
V_S	Ship velocity
w	Taylor's wake fraction
x	state variables
X_{md}	d-axis magnetizing Reactance of generator
X_{mq}	q-axis magnetizing Reactance of generator
Y	Fuel index (governor setting)

z	dc load of Genrator-rectifier system
α	Voltage ratio between dc side and ac side of three-phase diode rectifier
α_k, α_{k+1}	Power ripple ratio of dc source with k and k+1 active engines respectively
β	Current ratio between dc side and ac side of three-phase diode rectifier
θ	Angular displacement of reference frame
λ_m	Magnetizing flux linkage of generator
ρ	Water density
τ	Engine time delay
τ_c	Engine mechanical time constant
τ_{fb}	Feedback time constant of exciter
τ_{ff}	Feed-forward time constant of exciter
φ	Phase shift between fundamental harmonics of generator voltage and current
φ_1	Transformation angle of abc to dq
φ_2	Initial phase angle of sinusoidal PWM
$\boldsymbol{\phi}_{ji}$	Right eigenvector of state matrix
$\boldsymbol{\psi}_{ik}$	Left eigenvector of state matrix
ω	Mechanical rotation speed
ω_e	Angular frequency

Subscripts

$_0$	Steady state (equilibrium)
$_a$	Average estimate (used mainly for power)
$_{avg}$	Average value of variables
$_b$	Battery
$_{bid}$	Bidirectional converter

Comp	Compensator
Cu	Copper losses
d	d-axis of dq reference frame
D	Diode
ess	Energy storage system
f	Field winding
Fe	Core losses
fw	Forward
G	Generator
hv	High voltage
k, k+1	Number of active engines
L	Inductor (or Load)
l	Losses
lv	Low voltage
m	Mechanical
on	On-state
q	q-axis of dq reference frame
rec	Rectifier
rms	Root mean square
S	DC Source
sc	Supercapacitor
su	Start-up
Sw	Switches
sw	Switching
T	Transformer

1 Introduction

1.1 Background

The concept of electric propulsion in marine vessels dates back to over 100 years ago. However, it was only after development of high power Variable Speed Drives (VSDs) in 1970's-1980's that electrically propelled ships became increasingly popular [1, 2]. The development of electric propulsion enabled to establish an onboard power system as a common electrical platform for propulsion and ship service loads. This shipboard power system is also called Integrated Power System (IPS), which is the characterizing element of an All Electric Ship (AES) [3, 4].

Fig. 1-1 depicts mechanical propulsion in comparison with the electrical propulsion concept. In the mechanical propulsion system, main combustion engines are directly coupled to the propellers. A mechanically-propelled ship normally uses auxiliary combustion engines to generate electrical power. In an AES, however, the main prime movers that form the generation modules of the IPS, supply the ship service loads as well as the ship propulsion system.

The overwhelming majority of present all-electric ships use ac distribution systems. With the penetration of power electronic converters in power systems, shipboard dc networks have also received attention in recent years [5-7]. The idea of dc distribution onboard ships seems to have distinct advantages over ac distribution at least in certain applications such as offshore support vessels. On the one hand, there is an increasing

interest in integration of energy sources and storage devices with dc outputs [6, 8]. The dc distribution system helps to reduce the number of conversion stages when incorporating these dc sources and devices. On the other hand, there still exist challenges with the ship ac power systems, such as the need for synchronization of the generation units, reactive power flow, inrush currents of transformers, harmonic currents, and three-phase imbalances. The shipboard dc power system enables the prime movers to operate at their optimal speeds, providing significant fuel saving in comparison to the conventional ac systems. It also offers further advantages, such as space and weight savings, and flexible arrangement of equipment [9].

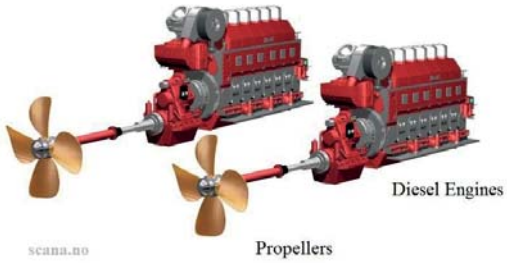

(a)

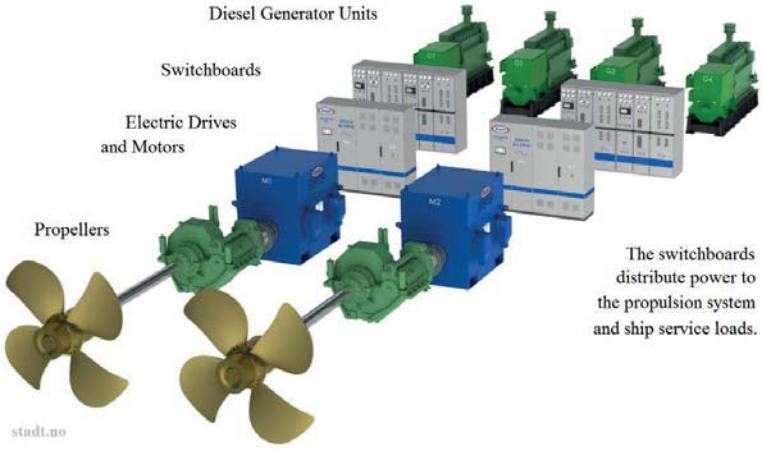

(b)

Fig. 1-1. Mechanical Propulsion (a) vs. Electrical propulsion (b).

There still exist different schools of thought on the top-level design decisions of the shipboard power networks including the choice between ac and dc distribution systems. The above-mentioned advantages, however, motivated an exclusive focus on shipboard dc grids in this dissertation.

1.2 Scope

Modeling and simulation of the shipboard dc power systems are essential in their design, analysis, power management, and control. As the standard power system analysis packages need excessive computation time to simulate these systems, an appropriate modeling for all modules is required. Derivation of the appropriate models and development of a system simulator is the first task that is pursued in this research.

A key motivation for the idea of shipboard dc power systems has been its potential for efficiency improvement and fuel saving. Enhancing the derived models of the simulator by including power loss models, the efficiency analysis of the onboard dc grids is included in this thesis. The fuel saving potentials will be investigated, and an optimized efficiency control strategy will be presented.

Several power electronic converters may make up the shipboard dc power systems to link different sources and loads to the grid. The stability is a major design and control consideration of such power systems due to potential negative incremental resistance introduced by power electronic converters. The power converters act as instantaneous Constant Power Loads (CPLs), which can drive the system to instability. This dissertation also deals with stability analysis and control of the shipboard dc grids.

The mentioned research tasks mainly target commercial marine vessels. Military applications and warships are not in the scope of this research, as they have different distribution architecture and power management requirements.

1.3 Contributions

The contributions of this dissertation are divided in three categories of modeling and simulation, efficiency analysis and optimization, and stability control.

A simulation platform is developed for time-domain studies of shipboard integrated dc power and propulsion systems. Models are derived for different mechanical and electrical elements including prime movers, generator-rectifier units, dc-dc converters, propellers, and ship hydrodynamics. In order to reduce the computation burden and time, averaging methods are applied to model power electronic converters. The simulation results of an integrated power and propulsion system are presented for three modes of operation. Providing significant savings in computational intensity and time, the simulation platform is effective in long-term or repetitive simulations of the studied systems.

Analysis of efficiency and fuel consumption of a shipboard dc power system is carried out. A numerical optimization algorithm is proposed to minimize fuel consumption of the multi-generator ship power systems by integration of energy storage. In order to evaluate practical fuel saving of the dc power system, an online optimization strategy is implemented. As a case study, an Offshore Support Vessel (OSV) is simulated over its seven operating modes under online optimization control. The fuel consumption is compared with the conventional ac power system as well as with the dc power system without energy storage. The study results demonstrate significant fuel saving potentials in OSVs through transition from ac to dc power systems, and integration of energy storage devices.

Regarding stability control, a robust large-signal stabilization technique is proposed to ensure global stability of a dc network with controllable loads. Taking into account measurement and parameters uncertainties, the proposed control method broadens the stability margins of isolated dc networks. This stabilization method allows having reduced-size capacitors for dc link and LC filters, which is particularly desirable for transportation systems. The proposed control method is validated through simulation and experimental results.

1.4 List of publications

The main research results of this PhD project are published in the following papers.

Journal papers:

B. Zahedi and L. E. Norum, “Modeling and Simulation of All-Electric Ships with Low Voltage DC Hybrid Power Systems”, *IEEE Transactions on Power Electronics,* vol. 28, pp. 4525-4537, 2013.

B. Zahedi, L. E. Norum, K. B. Ludvigsen, "Optimized Efficiency of All-Electric Ships by DC Hybrid Power Systems," *Journal of Power Sources*, vol. 255, pp. 341-354, 2014.

B. Zahedi, B. Nahid-mobarakeh, S. Pierrefederici, and L. E. Norum, “Robust Active Global Stabilization of DC Microgrids with Tightly Controlled Loads”, submitted to *IEEE Transactions on Industrial Electronics*.

Conference papers:

B. Zahedi; L. E. Norum; “Modeling, Analysis and Control of an Isolated Boost Converter for System Level Studies”, in *Proceedings of Aegean Conference of Electrical Machines and Power Electronics 2011* (ACEMP’11), pp. 179-184, September, 2011.

B. Zahedi, O. C. Nebb and L. E. Norum, “An Isolated Bidirectional Converter Modeling for Hybrid Electric Ship Simulations”, in *Proceedings of IEEE Transportation Electrification Conference and Expo 2012* (ITEC 2012), Dearborn MI, June 17-20, 2012.

O. C. Nebb, B. Zahedi, J. O. Lindtjorn, and L. E. Norum, “Increased Fuel Efficiency in Ship LVDC Power Distribution Systems”, in *proceedings of the IEEE Vehicle Power and Propulsion Conference 2012* (VPPC 2012), Seoul, Oct. 9-12, 2012.

B. Zahedi and L. E. Norum; “Modelling and Simulation of Hybrid Electric Ships with DC Distribution Systems”, in *Proceedings of the Power Electronics and Applications (EPE 2013),* Lille, Sept. 2013

B. Zahedi and L. E. Norum; “Voltage Regulation and Power Sharing Control in Ship LVDC Power Distribution Systems”, in *Proceedings of the Power Electronics and Applications (EPE 2013),* Lille, Sept. 2013

B. Zahedi and L. E. Norum, "Efficiency Analysis of Shipboard dc power systems," in *Proceedings of IEEE Inductrial Electronics Conference*, Vienna, Nov. 2013

B. Zahedi, L. E. Norum, and K. B. Ludvigsen, "Optimization of fuel Consumption of Shipboard Power systems," in *Proceedings of IEEE Industrial Electronics Conference*, Vienna, Nov. 2013.

M. K. Zadeh, B. Zahedi, M. Molinas, and L. E. Norum, “Centralized Stabilizer for Marine DC Microgrids”, in *Proceedings of IEEE Inductrial Electronics Conference*, Vienna, Nov. 2013.

1.5 Thesis outline

Chapter 2 of this thesis is focused on modeling and simulation of shipboard dc hybrid power systems. Models of different electrical and mechanical elements are derived. Power electronic converters are modeled through nonlinear averaging techniques to give an effective solution with the accuracy and speed of simulation for system-level analysis. In section 2.4, a simulation platform is developed in MATLAB/Simulink® for time-domain analysis of integrated dc power systems. As a case study, a hybrid electric ship is simulated in different modes of operation. The simulation results of a power sharing control among two diesel generators, a fuel cell unit, and an energy storage system are demonstrated.

Benefited from the established simulation platform, the overall efficiency of the onboard power system is analyzed in chapter 3. The shipboard dc power system is assumed to have four diesel generators and an energy storage system. An optimization algorithm is devised to ensure minimal fuel consumption. As a case study, an offshore support vessel (OSV) is simulated under an online optimization control in MATLAB/Simulink. The simulation evaluates the on-line fuel saving of the OSV over different modes of operation. The study results demonstrate that the dc system with optimized utilization of energy storage provides substantial fuel saving compared to the conventional ac system.

Chapter 4 is dedicated to the stability studies of a multi-converter dc network. It sets forth a centralized control of the power converters to improve global stability of the system. Taking into account measurement errors and parameters uncertainties, a robust nonlinear stabilization technique is proposed that increases the stability margins. The analysis and simulations are supported by experimental results to illustrate the validity of the proposed stabilization technique.

Conclusions are drawn in chapter 5, along with the possibilities for future investigations and research.

Four appendices provide analytical and numerical support for the methodologies and results presented in the thesis. References to the appendices are made throughout the text.

A version of chapter 2 has been published as:

B. Zahedi and L. E. Norum, “Modeling and Simulation of All-Electric Ships with Low Voltage DC Hybrid Power Systems”, *IEEE Transactions on Power Electronics,* vol. 28, pp. 4525-4537, 2013.

A version of chapter 3 has been published as:

B. Zahedi, L. E. Norum, K. B. Ludvigsen, "Optimized Efficiency of All-Electric Ships by DC Hybrid Power Systems," *Journal of Power Sources*, vol. 255, pp. 341-354, 2014.

A version of chapter 4 has been submitted:

B. Zahedi, B. Nahid-mobarakeh, S. Pierrefederici, and L. E. Norum, “Robust Active Global Stabilization of DC Microgrids with Tightly Controlled Loads”, submitted to *IEEE Transactions on Industrial Electronics*, 2014.

2

Modeling and Simulation of the Power and Propulsion System

Modeling and simulation are essential tools to facilitate design, analysis, and optimization of shipboard dc hybrid power systems. This chapter reviews modeling of all-electric ship components including mechanical and electrical elements. Power electronic converters are modeled using nonlinear averaging methods to suit system-level studies. A unified model for bidirectional converters is proposed to avoid transitions between two separate models. A simulation platform including the derived models is developed for system-level analysis of all-electric ships with dc distribution systems. Simulation results of power sharing among two diesel generators, a fuel cell module, and an energy storage system are presented for three modes of operation.

DC power electronic-based power systems are of interest for future low-emission and fuel-efficient marine vessels. Modeling and simulation are essential tools in design, analysis, power management, and control of these systems. As the standard power system simulation packages need excessive computation time to simulate power-electronic based systems [10], an appropriate modeling for all modules appears to be necessary. In terms of computation time, the limiting elements in the modeling of these systems are power electronic converters, as they require extremely small time steps [11].

This chapter deals with modeling and simulation of shipboard integrated dc power

and propulsion systems. Different electrical and mechanical elements are modeled such as the synchronous generator-rectifier system, inverter, dc/dc converters, diesel engines, propellers, and ship hydrodynamics. Power electronic converters are modeled using nonlinear averaging techniques to provide an effective solution with the accuracy and speed of simulation for large signal analysis. A simulation platform is developed in MATLAB/Simulink for system-level studies of integrated dc power and propulsion systems. As a case study, an all-electric ship with dc distribution is simulated in different modes of operation. The simulation results of a power sharing control among two diesel generators, a fuel cell unit, and an energy storage system show that the simulation program can be applied in system studies associated with design, evaluation, power management, etc.

2.1 System Overview and Characteristics

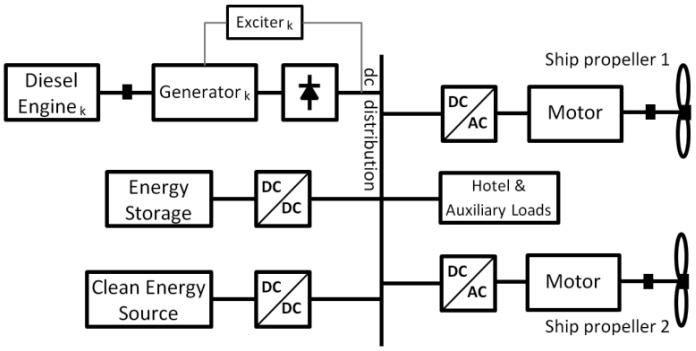

Fig. 2-1. Single-line diagram overview of the studied shipboard dc hybrid power system

Along with the benefits power electronics provides in hybrid power systems, they add to system complexity due to switching behavior of the semiconductors and the nonlinear properties of the power converters. System-level analysis of the shipboard power electronic-based power systems requires appropriate modeling that suits specific characteristics of the system. These characteristics are briefly explained as follows:

- There are mechanical and electrical components in such a system with extremely different dynamics. The time constants of these dynamics range from a very small time constant of a power electronic switch, which is on the order of nanoseconds to a large time constant of ship hydrodynamics, which is tens of seconds. Thus,

detailed switching models of power electronic converters lead to excessive simulation run-time. Reduced-order converter models using averaging techniques make the simulation orders of magnitude faster. Therefore, dynamic averaging is a time-efficient solution when studying the exact switching behavior is not necessary.

- Small signal or linearized averaging is imprecise for system-level studies that include large variations in system states. Large signal models are to be developed, which can be implemented by nonlinear averaging methods [12].

- The interactions among connected elements should be applied in order for the system model to be causal. This means that each element should receive the reaction of the element on that it acts. Therefore, the interfaces among connected models must be bidirectional.

- It is also preferred that the developed models are able to interface with elements in standard simulation tools, in order to take advantage of the existing valid models.

A single-line diagram of a shipboard dc power distribution system is depicted in Fig. 2-1. This given combination includes typical components and modules of the hybrid system. Fuel cells and solar energy are the proposed clean energy sources for future fuel-efficient vessels. Solar power source can be combined with wind power source by using fixed sails that are equipped with solar panels. This architecture can bring in opportunities for zero-emission operation [13]. Different types of energy storage can be used onboard an all-electric ship, such as electrochemical batteries and super capacitors.

Detail dynamic models of the sources and energy storages are essential in order to implement their dynamic behaviors and constraints for time-domain analysis. Diesel engines are an example of main energy sources, which have slow dynamics resulted from ignition delay and mechanical time constant. This will be addressed in section 2.3. Fuel cell is proposed as an auxiliary energy source for ship applications. Its terminal voltage drops sharply at high currents due to fuel starvation, which may lead to irreversible damages to the cell. This phenomenon is avoided by limiting its current dynamics, which causes fuel cell to be a slow dynamic source. Batteries or super capacitors that have faster dynamics are used in combination with fuel cells to manage fast transient loads [14]. However, these energy storage devices have also limitations on their capacity and dynamic behavior. The aforementioned restrictions can be taken into account in simulation through their detailed dynamic models.

2.2 Modeling of Power Electronic Converters

In a shipboard dc distribution system, the majority of the power supplied to the dc grid passes through three-phase rectifiers after originating from synchronous generators. These rectifiers could be uncontrolled three-phase diode rectifiers if the generators are of wound rotor type. In this case, the voltage regulation is performed by the generator excitation system. A thyristor-based rectifier can also be employed [15]. However, since its control functionality is mainly used under fault conditions, it can be considered as an uncontrolled rectifier in normal operation. In case of using a Permanent Magnet Synchronous Generator (PMSG), the rectifier would be of controlled type with three-phase bridge inverter topology. The controlled rectifier is able to perform either voltage regulation or current control depending on the system requirements.

DC/DC converters are prominent for energy management of shipboard hybrid electric systems. They could also be used to shift dc voltage level along the dc distribution system [16]. It is a common practice to use bidirectional converters to incorporate energy storage in electric power systems. Although most ships do not currently have energy storage except in the fuel, future all-electric ships would need electric energy storage, such as batteries. These energy storage devices can be controlled by bidirectional converters. A boost-type bidirectional converter is used to connect low-voltage energy storage to the high voltage dc bus [17]. This enables to use lower number of battery cells in series, which provides better reliability. The boost topology could be also a suitable option for employing auxiliary dc energy sources such as fuel cells.

A high share of the generated power onboard an electrically propelled ship is consumed by the variable speed drives of the propulsion system[18]. The motor drive basically uses a three-phase bridge inverter to supply and control the motor.

Modeling of the mentioned power electronic converters is discussed in the following.

2.2.1 DC/DC converters

Topological circuits of an isolated full-bridge boost converter and an isolated full-bridge bidirectional converter are shown in Fig. 2-2.a and b, respectively.

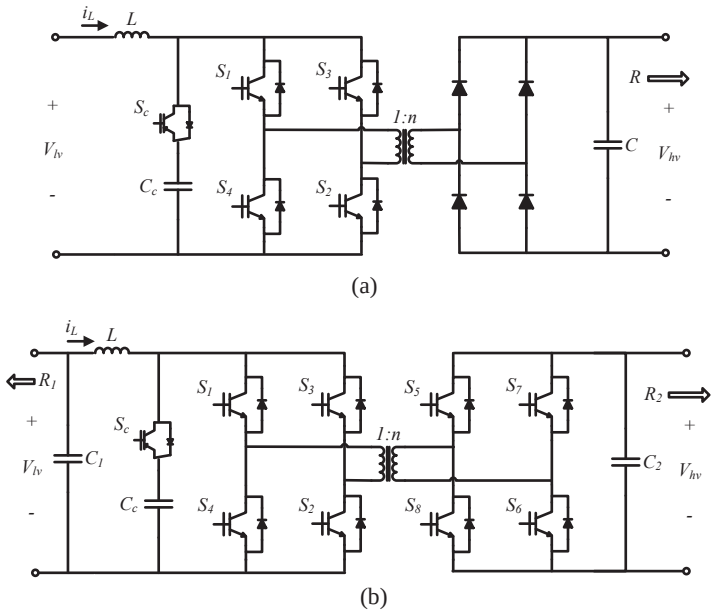

Fig. 2-2. Topological circuit of the converters under study, a) boost b) bidirectional

High frequency transformer may be required in those applications where the voltage ratio between LV and HV is beyond a certain limit. Otherwise, devices should tolerate both high voltage and high current simultaneously, which is not economical. Another role of the high-frequency transformer is to provide isolation for safety requirements. It also brings in an additional degree of freedom compared to the basic topology by introducing the transformer turns ratio. Nevertheless, the high frequency transformer entails more cost and power losses. The advantage of the full-bridge topology is to provide lower voltage and current stresses, resulting in significantly lower power losses compared to half-bridge and push-pull topologies. It, however, needs high number of switches [17].

To simulate these power converters a number of software packages are available. Nonetheless, due to using detailed switching models, they are too slow for analysis of rather large power electronic-based systems. Therefore, when exact switching behavior is not required in the study, dynamic averaging methods may be used to make the simulation faster [19]. As large variations may occur in the system, small signal models could be imprecise for system simulation. Hence, large signal modeling which includes

nonlinear relations is required. Fig. 2-3 and Fig. 2-4 illustrate the errors of the linear small signal models in comparison with detailed switching model and nonlinear models. The studied methods include AVM (small signal Average Value Model), Linear SSAVM (Linearized State Space Average Value Model), Nonlinear SSAVM, and GSSAM (Generalized State Space Average Model) [12, 20-22]. The models are simulated in MATLAB/Simulink, and compared with detailed model implemented in PLECS. The above-mentioned modeling procedures are summarized in the Appendix [see A]. The design parameters of the studied converters are given in Table 2.1.

TABLE 2.1
DESIGN PARAMETERS OF THE CONVERTERS UNDER STUDY

$V_{hv} = 620\ V$	$R = R_2 = 19.22\ \Omega$
$V_{lv} = 100\ V$	$C_1 = 500\ \mu F$
$D = 0.516$	$C = C_2 = 267\ \mu F$
$f_{sw} = 2\ kHz$	$L = 516\ \mu H$
$R_1 = 0.5\ \Omega$	$n = 3$

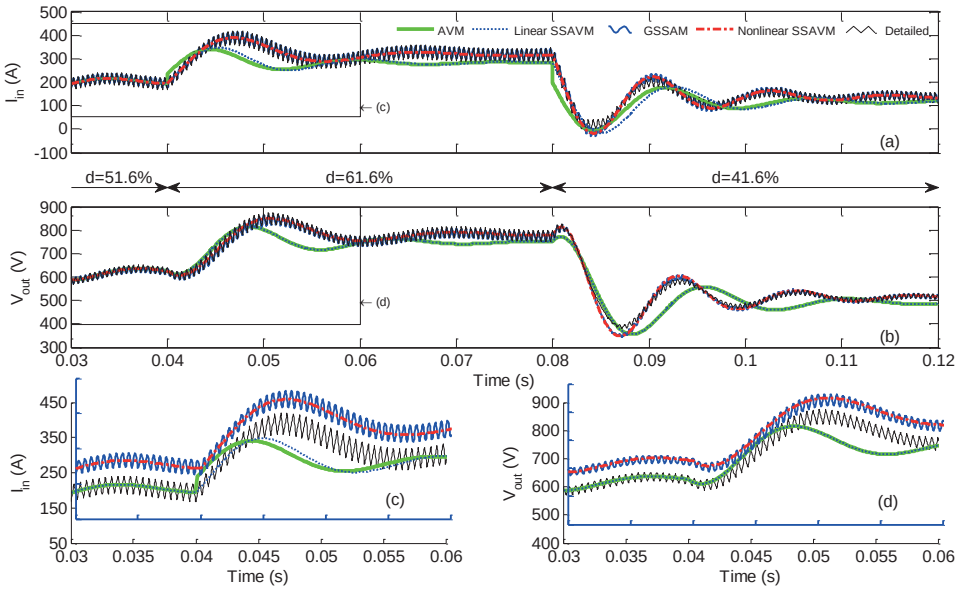

Fig. 2-3. Comparison of Open-loop duty cycle step response for boost converter/mode

Fig. 2-3 illustrates the simulation results for average models of the boost converter based on the open loop response to duty cycle step changes. These results are also the case for boost mode of the bidirectional converter. To see the details more clearly, parts of the curves are enlarged in Fig. 2-3.c and d, and the curves of nonlinear methods are slightly shifted to separate frames. It can be seen that the linearized models create errors both in transient and steady state conditions. The errors increase as the duty cycle further deviates from its design value. The generalized averaging approach exhibits the most accurate behavior by taking harmonics into account [20, 21]. However, the drawback of GSSAM is its slow simulation. Nonlinear SSAM is accurate and at the same time provides high simulation speed.

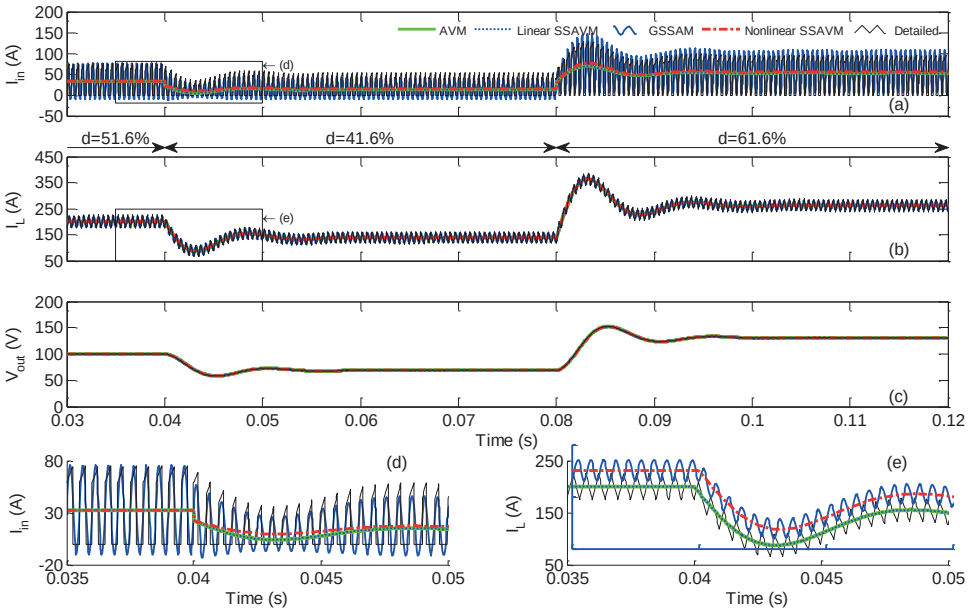

Fig. 2-4. Comparison of Open-loop duty cycle step response for buck converter/mode.

The other operational mode of the bidirectional converter is buck mode. Fig. 2-4 shows the open loop time response of the different buck average models to duty cycle step changes. The buck converter shows more linearity compared to boost converter. Therefore, the differences between linear and nonlinear models are limited in case of the buck converter. The input current, however, is still nonlinear in terms of duty cycle, and certain error can be observed for linear models in Fig. 2-4.d. Another difference is about

the pulsation modeling. As the input current in the buck converter has a highly pulsating waveform, the difference is particularly significant in current estimation. The generalized averaging by modeling the first order harmonic is following the pulsations of the input current wave form; whereas the normal averaging methods are following only the dc value of the wave form in each switching period. However, an input filter is normally used in practice which reduces the importance of this pulsation modeling.

The foregoing comparisons indicate that nonlinear SSAVM is the preferable approach for both buck and boost modes of operation in terms of both the accuracy and simulation speed. Two models for buck and boost modes can be combined to form a unified model for the bidirectional converter [23]. This prevents from the associated problems with transitions between two models during simulation. Such a model, however, can only represent the converter in voltage source mode of operation, as the input and output voltages are included in the state vector. In order to model the converter in current source mode, a different approach should be devised.

2.2.1.1 Representation for current source mode

The above-mentioned approaches are used when voltage is assumed to be the output of the model. However, in those applications where current should be the output, and the voltage is applied as an input, state space approaches cannot provide proper modeling. Averaged switch modeling is considered in the following as a solution [20].

Simplifying the switch network of the bidirectional converter of Fig. 2-2.b, we obtain Fig. 2-5.a and b for buck and boost modes, respectively. The duty cycle of the new topologies is the actual duty cycle divided by the transformer turns ratio. Averaged circuits for each mode are obtained as Fig. 2-6 using the averaged switch modeling [19], however in a nonlinear form. The operation of the boost mode at duty cycle of “d’” (=1–d) corresponds to the operation of buck mode at duty cycle of “d”, with only the opposite current direction. Therefore, each equivalent circuits of Fig. 2-6 can represent a unified model for the bidirectional converter. The boost converter of Fig. 2-2.a can be modeled by equivalent circuit depicted in Fig. 2-6.b.

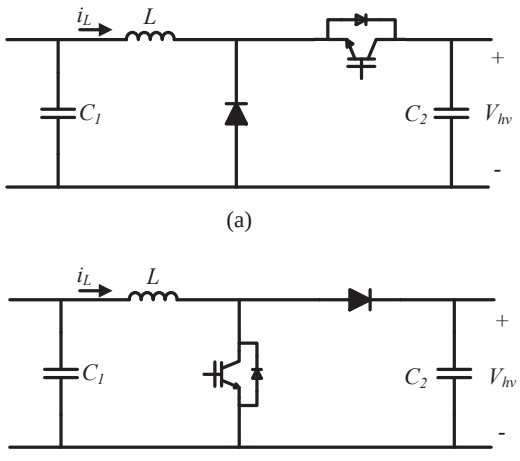

Fig. 2-5. Simplified topology of the bidirectional converter, a) buck mode b) boost mode ($d_{new}=d_{actual}/n$)

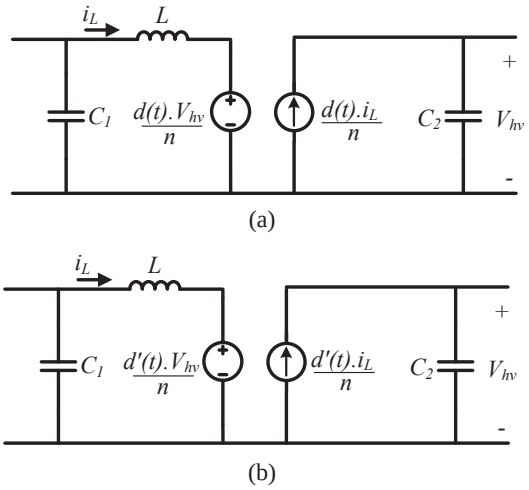

Fig. 2-6. Averaged circuit model of the bidirectional converter, a) buck mode b) boost mode (model.a can be used as a unified model since $d'_{discharge}\equiv d_{charge}$)

Fig. 2-7 and Fig. 2-8 illustrate the simulation results of the unified model. Fig. 2-7 shows open-loop response to duty cycle step changes over a charge/discharge cycle. The low voltage side and high voltage side of the converter are supplied at their rated voltage levels. A time constant for inductor charging/discharging is taken into account.

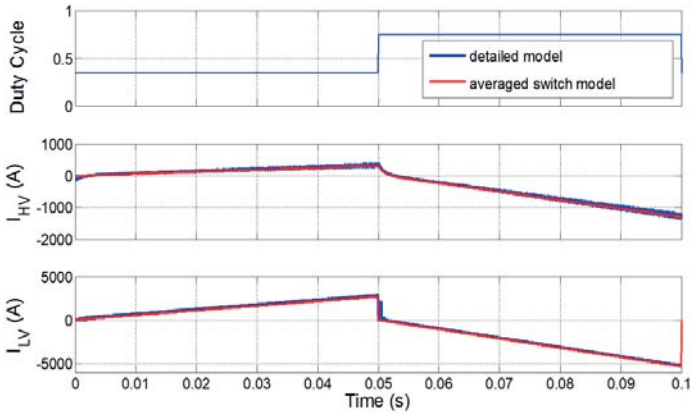

Fig. 2-7. Open loop response of the unified bidirectional model to duty cycle. step change over a charge/discharge cycle.

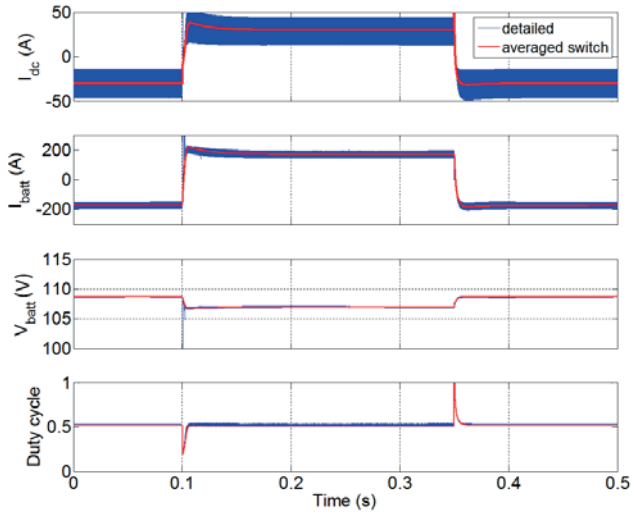

Fig. 2-8. Closed loop current control response to dc current step commands, charging/discharging the battery. (The converter controls the dc current on ±30A.)

The unified model is used in simulation of an energy storage system. The energy storage device is a NiMH battery pack rated at 100V and 200Ah, which is connected to a dc bus through the bidirectional converter under study. The dc bus voltage level is considered fixed at 620V, and the ESS power is controlled through its HV-side dc current. Fig. 2-8 shows a charge/discharge cycle of the battery when dc current is controlled on ±30A. The inversion-based control methodology [24] is used to control the converter average model as well as the detailed switching model. The simulation

results validate the proposed unified model against the detailed model. It should be noted that this model is also nonlinear to suit large signal analysis.

2.2.2 The Synchronous generator-rectifier system

Average modeling of synchronous machine-converter systems has been a challenge for decades, as several articles explored this issue from late 1960s [25, 26] to recent years [27, 28]. In initial attempts, the rectifier was modeled by algebraic expressions to relate the ac variables to rectifier dc variables assuming the generator as a voltage behind a constant reactance [25, 26]. In [29], the steady state characteristics of the synchronous machine-rectifier system are represented by reduced-order models. Despite the accuracy of this approach in steady state, due to neglecting the stator dynamics, it is inaccurate for fast transients. This work was extended in [30], where a dynamic average value model with good compliance to both detailed simulation and experimental results is presented. The analysis, however, is limited to a single switching pattern (conduction and commutation intervals). In [31], the parameters of the average model are obtained from detailed simulation of the synchronous machine-rectifier system. Nevertheless, these parameters are not dependent on operating conditions, creating errors when predicting the source impedance. An extension of this work is presented in [28], wherein the average model parameters are obtained by running the detailed simulation at multiple operating points. These parameters are no longer constant values, but a set of nonlinear algebraic functions that are dependent on the operating conditions. This provides an accurate dynamic model in different rectifier modes over a wide range of frequencies.

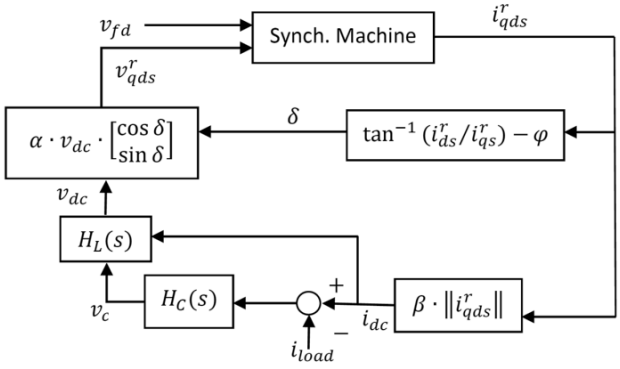

Fig. 2-9. Block diagram AVM model of the synchronous generator-rectifier system; constant model parameters.

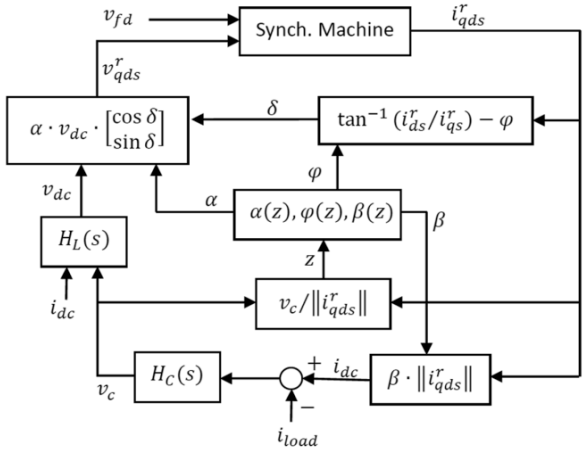

Fig. 2-10. Block diagram AVM model of the synchronous generator-rectifier system; variable model parameters.

Fig. 2-9 and Fig. 2-10 summarize the models of the last two mentioned references in block diagrams. The dynamic averaging of the rectifier circuit is done by establishing a relationship between the dc-link variables on one side and the ac variables transferred to a suitable reference frame on the other side. As can be seen in Fig. 2-9, this relationship is established in [31] by assuming three parameters α, β, and φ to be constant, where α is the voltage ratio between dc side and ac side, β is the current ratio, and φ is the phase shift between the fundamental harmonics of generator voltage and current. Different denotations are used for α and β in [31] i.e. k_v, k_i (k_v is the inverse of α, and k_i equals β).

As can be seen in Fig. 2-10, the model parameters in [28] are considered to be functions of the generator loading conditions, which is quantified by "z". These functions are calculated by running the detailed simulations at different loading conditions for a machine-rectifier system. Fig. 2-11 shows these algebraic functions for a synchronous generator given in the Appendix [see Table B. I].

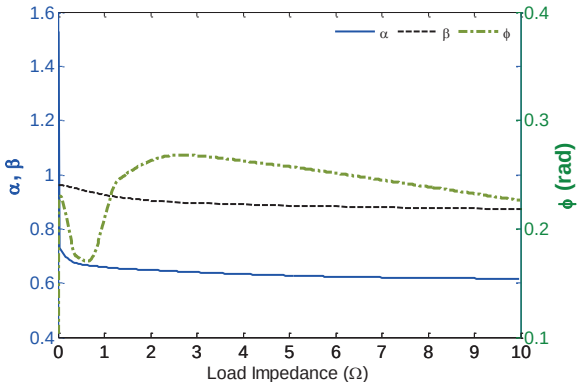

Fig. 2-11. Algebraic functions α, β, and φ of the generator loading conditions, obtained from detailed simulations.

Fig. 2-12 and Fig. 2-13 compare simulation results of the average models with constant and variable parameters with the detailed model. AVM with constant parameters shows satisfactory results under light load conditions (≥2.5 Ω). However, as load increases (load=1Ω in Fig. 2-12) certain errors appear in its voltage and current approximations. It is seen in Fig. 2-13 that its accuracy decreases even further under heavy loads (≤0.5 Ω). However, the accuracy can be improved by AVM with variable parameters. An excellent match, regarding frequency domain behavior, is also reported in [28] by comparison of the parametric AVM with the detailed model and experimental results.

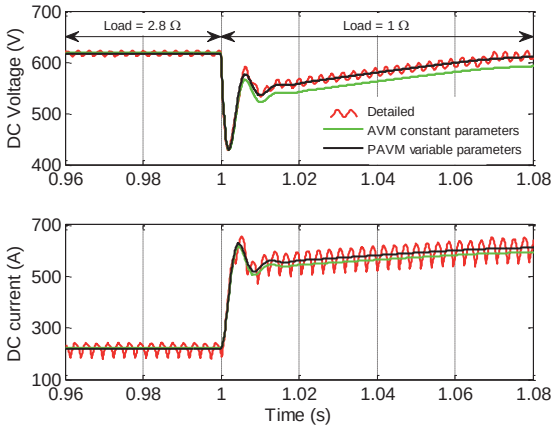

Fig. 2-12. SM-Rectifier response to a load step change at lower loads.

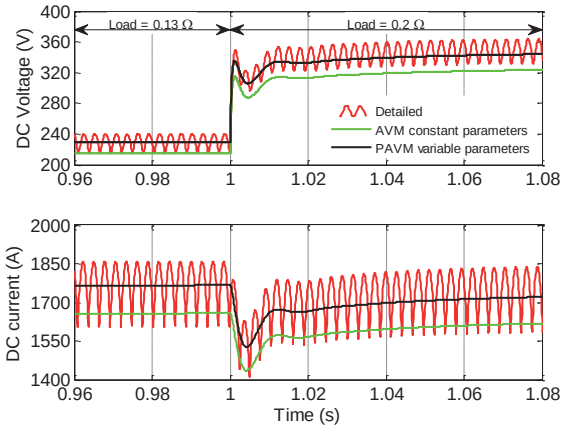

Fig. 2-13.SM-Rectifier response to a load step change at higher loads.

2.2.3 Voltage source inverter

The topology of a three-phase Voltage Source Inverter (VSI) is shown in Fig. 2-14. The average value model for a PWM voltage source inverter is considered here. The PWM VSI can be modeled with an equivalent stationary circuit by d-q transformation [32].

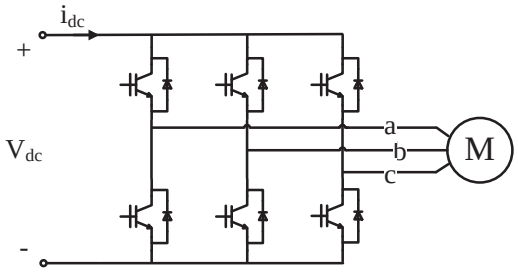

Fig. 2-14. Topology of a three phase voltage source inverter.

In order to develop an average model for VSI, it is assumed that all switches operate at continuous conduction mode (CCM) with a PWM switching pattern provided that the switching harmonics are not dominant. Considering these assumptions, averaging can be applied by approximating the sinusoidal PWM with a continuous sinusoidal waveform, which can be expressed by

$$\begin{bmatrix} v_a \\ v_b \\ v_c \end{bmatrix} = \begin{bmatrix} d_a \\ d_b \\ d_c \end{bmatrix} . v_{dc} \tag{2.1}$$

where switching functions "$d_{a,b,c}$" can be defined using the modulation index "m" by

$$\begin{bmatrix} d_a \\ d_b \\ d_c \end{bmatrix} = \begin{bmatrix} \sin(\theta(t) + \varphi_2) \\ \sin(\theta(t) + \varphi_2 - 2\pi/3) \\ \sin(\theta(t) + \varphi_2 + 2\pi/3) \end{bmatrix} \cdot m \tag{2.2}$$

φ_2 is the arbitrary initial phase angle of SPWM.

DC current can now be expressed by

$$i_{dc} = d_a i_a + d_b i_b + d_c i_c \tag{2.3}$$

Defining a switching vector **S** for the inverter, the transformation of variables from ac side to the inverter dc side can be simply expressed by

$$\begin{cases} \mathbf{v_{abc}} = \mathbf{S} \cdot v_{dc} \\ i_{dc} = \mathbf{S^T} \cdot \mathbf{i_{abc}} \end{cases} \tag{2.4}$$

where the switching vector **S** is

$$\mathbf{S} = m \cdot \begin{bmatrix} \sin\left(\theta(t) + \varphi_2\right) \\ \sin\left(\theta(t) + \varphi_2 - 2\pi/3\right) \\ \sin\left(\theta(t) + \varphi_2 + 2\pi/3\right) \end{bmatrix} \tag{2.5}$$

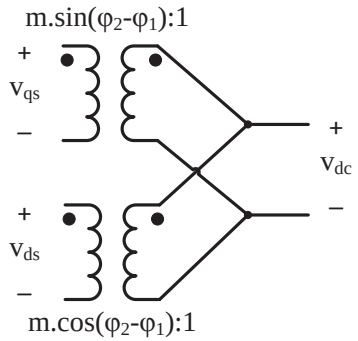

Fig. 2-15. D-Q average model of a three phase PWM Voltage Source Inverter.

In order for the inverter model to interface with electric machine d-q models, the above phasor representation is transformed to d-q domain:

$$\mathbf{X_{qdo}} = \mathbf{K} \cdot \mathbf{X_{abc}} \tag{2.6}$$

where **K** is the d-q transformation matrix with a transformation angle of φ_1 which is defined by

$$\mathbf{K} = \frac{2}{3}\begin{bmatrix} \cos\left(\theta(t)+\varphi_1\right) & \cos\left(\theta(t)+\varphi_1-2\pi/3\right) & \cos\left(\theta(t)+\varphi_1+2\pi/3\right) \\ \sin\left(\theta(t)+\varphi_1\right) & \sin\left(\theta(t)+\varphi_1-2\pi/3\right) & \sin\left(\theta(t)+\varphi_1+2\pi/3\right) \\ 1/2 & 1/2 & 1/2 \end{bmatrix} \tag{2.7}$$

Substituting variables of (2.4) into (2.6), we will have

$$\begin{cases} v_{qdo} = \mathbf{K} \cdot \mathbf{S} \cdot v_{dc} \\ i_{dc} = \mathbf{S^T} \cdot \mathbf{i_{abc}} = \mathbf{S^T} \cdot \mathbf{K^{-1}} \cdot \mathbf{i_{qdo}} \end{cases} \tag{2.8}$$

Simplifying the equations, we will obtain

$$\begin{cases} \begin{bmatrix} v_q \\ v_d \end{bmatrix} = \begin{bmatrix} \sin\left(\varphi_2-\varphi_1\right) \\ \cos\left(\varphi_2-\varphi_1\right) \end{bmatrix} \cdot m \cdot v_{dc} \\ i_{dc} = m\left(i_q \sin\left(\varphi_2-\varphi_1\right) + i_d \cos\left(\varphi_2-\varphi_1\right)\right) \end{cases} \tag{2.9}$$

Therefore, the inverter can be represented by time-invariant transformers shown in Fig. 2-15.

The equivalent circuit can be simplified by assuming φ_2 equal to φ_1. In this case, one of the transformers will be eliminated, and the model will be as simple as (2.10).

$$\text{if } \varphi_2 \triangleq \varphi_1 \Rightarrow \begin{cases} v_d = m \cdot v_{dc} \\ i_{dc} = m \cdot i_d \end{cases} \tag{2.10}$$

2.3 Modeling of Mechanical Subsystems

In this section, dynamic models of mechanical elements in an integrated ship power and propulsion system are presented.

2.3.1 Propellers

Modeling of the propeller can be established by relationships among thrust, torque, and speed. For a fixed pitch propeller, these relationships can be expressed by (2.11) and (2.12) [33].

$$T_p = \rho D_p^4 K_T n_m |n_m| \tag{2.11}$$

$$Q_p = \rho D_p^5 K_Q n_m |n_m| \tag{2.12}$$

where T_p is propeller thrust [N], n_m is propeller shaft speed [rpm], and Q_p is propeller torque [Nm]. The parameters ρ, D_p, K_T, and K_Q are water density, propeller diameter, thrust coefficient, and torque coefficient, respectively.

K_T and K_Q are functions of the propeller structure, and advance ratio J which is defined in (2.13) [34].

$$J = \frac{V_A}{n_m D_p} \tag{2.13}$$

V_A is the advance velocity of the propeller. It is normally less than the ship speed V_S due to wake. Their relationship is expressed by (2.14).

$$V_A = V_S(1-w) \tag{2.14}$$

where w is Taylor's wake fraction [35]. In order to calculate the ship speed resulted from the propeller thrust, ship hydrodynamic model is also required.

2.3.2 Ship hydrodynamics

The vessel hydrodynamic model could be complicated when dynamic positioning is

purposed [36]. However, for power system analysis in integrated power and propulsion systems, a one-dimensional motion model suffices. Therefore, the ship can be treated as an inertial mass with a resistive drag, on which the propeller thrust "T_p" applies. The resistive drag is proportional to the square of ship speed "V_S".

In order to take advantage of the established models with identified parameters, Marine System Simulator toolbox [37] is employed for the propeller and ship models.

2.3.3 Diesel engines

Diesel engine dynamics can be modeled in different levels of complexity, depending on the application. In this study, it is approximated by a time delay τ and a time constant τ_c [34] as represented in (2.15).

$$T_m(s) = e^{-\tau s} \frac{K_y}{1+\tau_c s} Y(s) \tag{2.15}$$

where T_m is the generated torque, K_y is the torque constant, and Y is the fuel index (governor setting). The time delay is half the period between consecutive cylinder firings, which can be calculated by (2.16) [38].

$$\tau \approx \frac{1}{2n_m N} \tag{2.16}$$

where n_m is the engine rotational speed in [rps], and N is the number of cylinders. The time constant is calculated by (2.17).

$$\tau_c \approx \frac{0.9}{2\pi n_m} \tag{2.17}$$

In order to model the interaction between the diesel engine and the synchronous generator, a speed control loop is established by a PI controller, which acts as a governor [39].

2.4 System Simulation

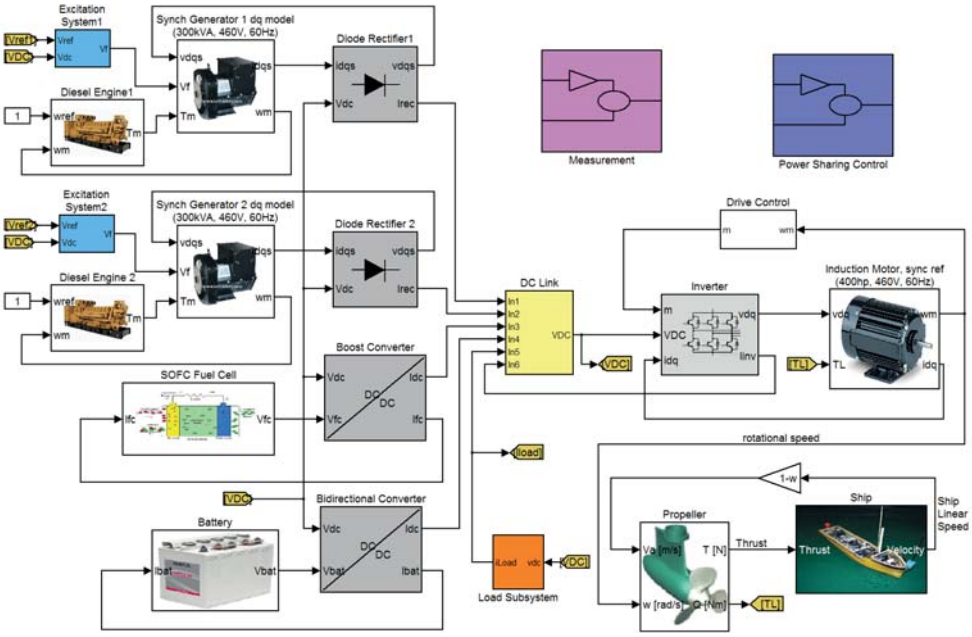

Fig. 2-16. Overview of the ship dc hybrid power system implemented in MATLAB/Simulink.

Appropriate models according to the system characteristics in section 2.1 are already derived for different elements. The derived models of power electronic converters are validated against detailed simulations. In this section, simulation results of a hybrid electric power and propulsion system are presented. Among various possible combinations, a dc hybrid power system is chosen that includes two diesel generators rated at 300 kW, a fuel cell system as an auxiliary source, and an energy storage system based on Li-Ion battery. Specifications of the fuel cell and the energy storage can be found in the Appendix [see B.1]. Integration of super capacitors is also proposed in ship applications where load transients repeatedly occur, e.g. dynamic positioning mode in offshore support vessels [18, 40]. As the major operational mode of the studied ship is cruise mode in that load transients are not so frequent, super capacitors are not used in this case study.

The overview of the system implemented in MATLAB/Simulink is depicted in the block diagram of Fig. 2-16. Interfaces among elements are bidirectional to ensure causal

interactions among connected elements. The product of two exchanged variables among connected elements yields power. This facilitates the interface among different types of electrical, mechanical, and electromechanical elements. The generators and converters have the same parameters as those studied previously in section 2.2. The unified model of Fig. 2-6 and parametric AVM of Fig. 2-10 are used in the simulations. The propulsion motor is a three-phase $460V_{l\text{-}l}$ induction motor rated at 400hp. Parameters for different parts of the system are given in the Appendix [see B].

To present the simulation results, a sailing profile including high speed (10 kt), moderate speed (5 kt), and low speed (1.5 kt) is studied in this section. Due to slow dynamics of the ship motion, each speed range is simulated for at least 60 seconds so that the ship can reach its steady state speed. The simulated ship is a large version of Cybership II [41] weighing 300 tons with a length of 50 m, which has similar hydrodynamic behavior. Fig. 2-17 shows the ship speed and the propeller rotational speed over the simulation time. In the first 60 seconds, the ship is accelerating from zero to full speed, which examines the power system response to high stress. The propeller accelerates much faster than the ship, as dynamics of the propulsion system is much faster than ship motion.

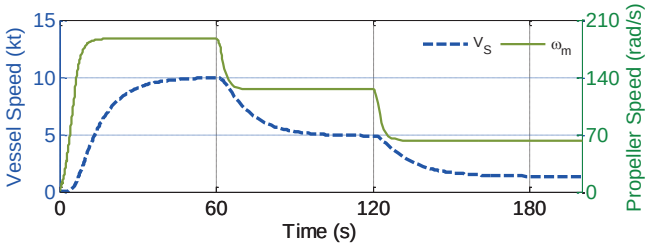

Fig. 2-17. Ship and propeller speeds.

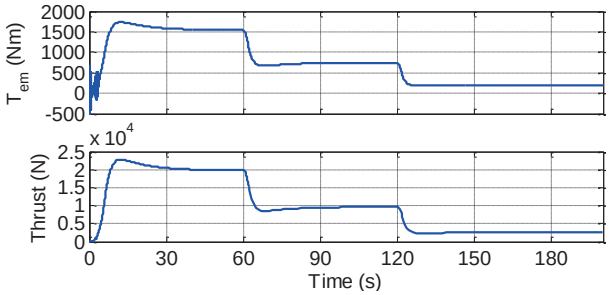

Fig. 2-18. Electromagnetic torque and thrust.

Fig. 2-18 shows electromagnetic torque of the propulsion motor, and applied thrust of the propeller. The peak torque and thrust occur as the motor reaches its peak speed. Motor soft starting is used by limiting the motor starting current to improve the stability of such a weak isolated power system, while having negligible effect on the ship acceleration. Assuming the ship propellers operate identically, only one propeller is simulated. The power demand and output thrust of the simulated propeller is doubled so as to represent both propulsion units.

Fig. 2-19 shows dc currents of different units that are connected to the dc grid. As shown, the diesel generators are starting under light load conditions before the sailing begins. This load is ship auxiliary and hotel load rated at 125 kW, which is modeled by a constant impedance load. The battery is being charged at start-up, and ensures stable operation of the diesel engines by adjusting the charge rate.

At high speeds, the propulsion system demands the highest amount of power. Therefore, both of the diesel generators, the fuel cell, and the energy storage supply power to the grid during the first minute of simulation. The propulsion power significantly reduces with reduction of propeller rotational speed and ship speed. Reduction of the ship speed by 50% leads to 70% reduction of the propulsion power, while the propeller speed has only decreased by 30%. At this speed range, one of the generators (G2) shuts down and the power is mainly supplied by the remaining generator (G1) and the fuel cell.

Depending on the load level, the battery can be charged or discharged at moderate rates. The battery also takes care of fast transient changes of load to compensate for the slow response of the diesel engines and the fuel cell. The rate of fuel cell current reference is limited to 20 A/s in order to prevent from fuel starvation [14]. The fuel cell power is controlled on its rated value to have optimal efficiency.

At slow speed operation, the generator G1 also shuts down, and the power is mainly supplied by the fuel cell. This provides ultra-low emission mode of operation, which is important when ship is approaching/leaving harbors at low speeds.

The operation in low emission mode is recommended to protect harbors and their nearby cities from NOx, SOx, and PM emitted by ships [42]. Emission of these air pollutants is reported to be zero in some fuel-cell powered ships, such as Viking Lady [43] and MethaPU [44].

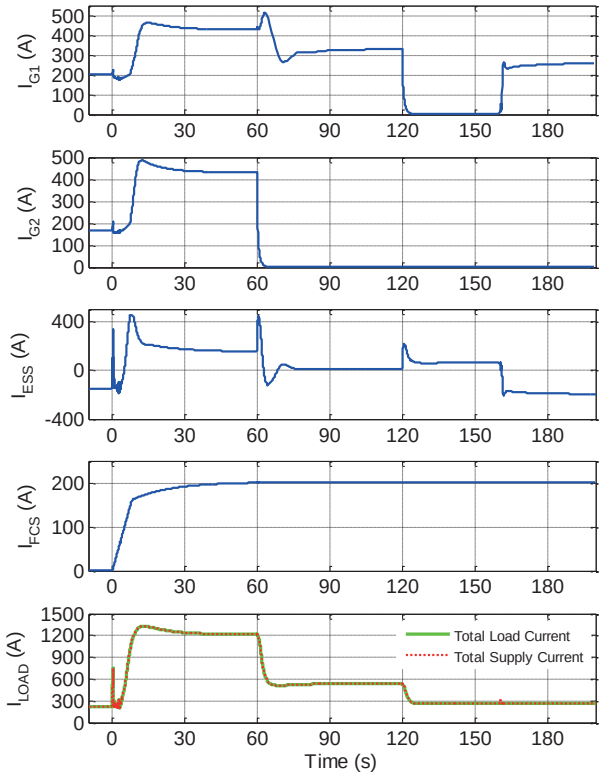

Fig. 2-19. DC currents of the sources, energy storage system (ESS), and load.

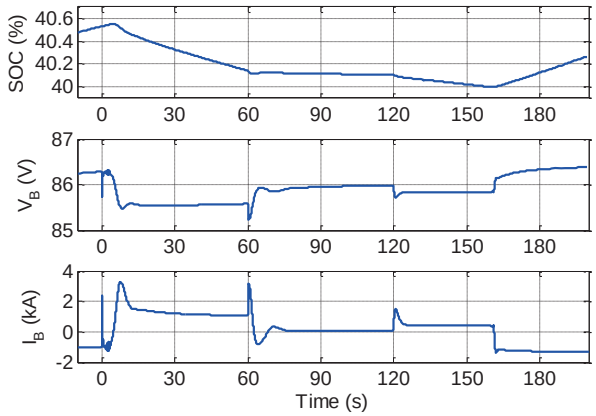

Fig. 2-20. Battery state of charge, voltage, and current.

The battery state of charge (SOC) is maintained within certain limits. This is done by

starting an idle diesel generator when SOC reaches the lower boundary, and by shutting down an active diesel generator when SOC exceeding the upper limit. Fig. 2-20 shows SOC, voltage, and current of the battery. As the battery SOC reaches the lower boundary, which is chosen 40% here, the diesel generator G1 starts in order to charge the battery and increase the state of charge. Restarting the diesel engine in such a short time would not be practiced in operation. Nevertheless, it is simulated here to cover a variety of events in a short time frame.

Fig. 2-21 shows the mechanical powers of the diesel engines in different modes of operation. Diesel engines operate efficiently over the range of 60% to 100% of their rated power [2]. Therefore, the steady state operating points of the diesel engines are maintained within this range. Fig. 2-22 shows the rotational speeds of the diesel engines under fixed speed control. Slight deviations can be seen at rapid load changes of the generators.

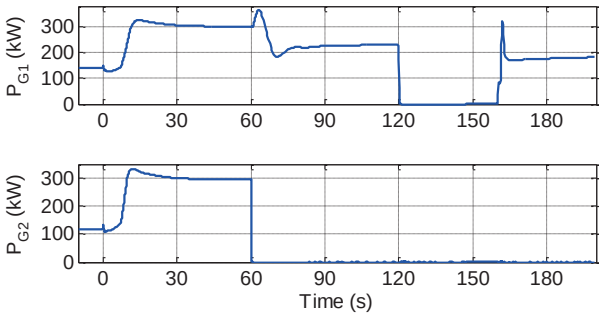

Fig. 2-21. Mechanical powers of the diesel engines.

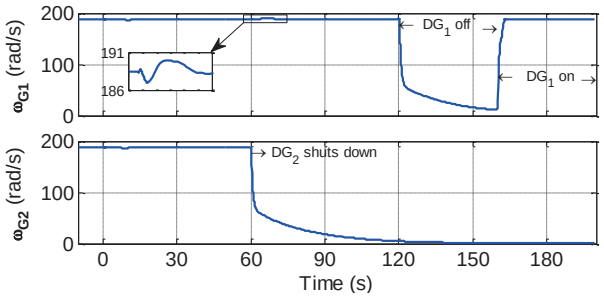

Fig. 2-22. Rotational speeds of the diesel generators.

The system dc voltage is regulated through voltage droop control method [45, 46]. The voltage droop characteristics of the two generator sets are depicted in Fig. 2-23.

Even though the generator sets are assumed identical, they most likely exhibit different droop characteristics in practice. Therefore, different droop settings are considered for the generator sets.

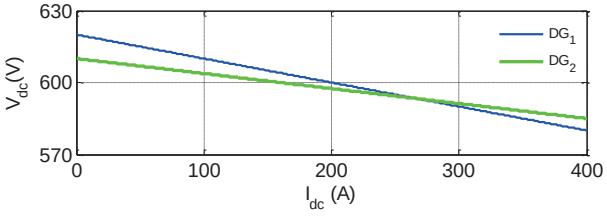

Fig. 2-23. Voltage droop characteristics of the generator sets.

A block diagram of the exciters is depicted in Fig. 2-24. A compensator is introduced as a secondary-level controller. This controller adjusts the voltage reference in order to control the generator load sharing. Fig. 2-25 shows excitation voltages and dc bus voltage. As seen in this figure, the dc bus voltage is not exactly controlled on a fixed value, which is a characteristic of droop control method. The compensation voltages for the two generator sets are depicted in Fig. 2-26. Under heavy loads, the compensator increases the voltage reference to deliver more power to the grid. As the load decreases, the compensation voltages reduce, leading to less power delivery from the generators.

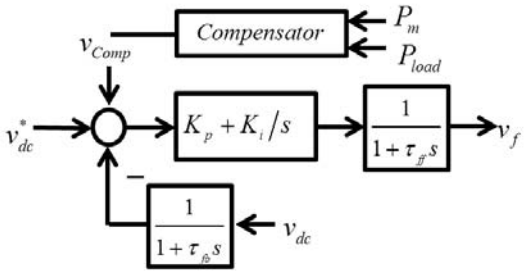

Fig. 2-24. Block diagram of the voltage regulator-exciter.

The foregoing simulation results demonstrate the capability of the presented simulation program in time-domain studies of integrated dc power and propulsion systems. These time-domain studies could be used for dynamic analysis, voltage regulation, power management, and control system design of shipboard dc power systems.

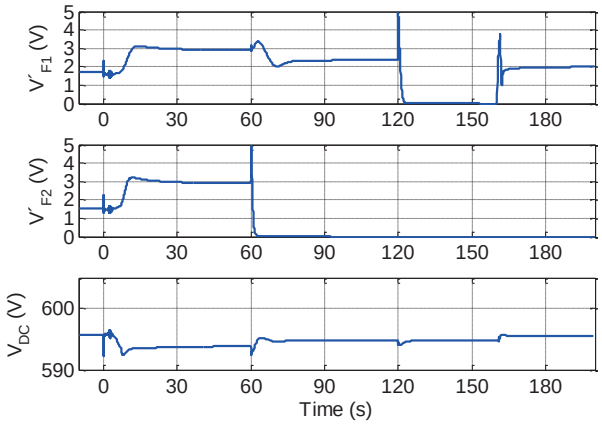

Fig. 2-25. Excitation voltages and dc bus voltage.

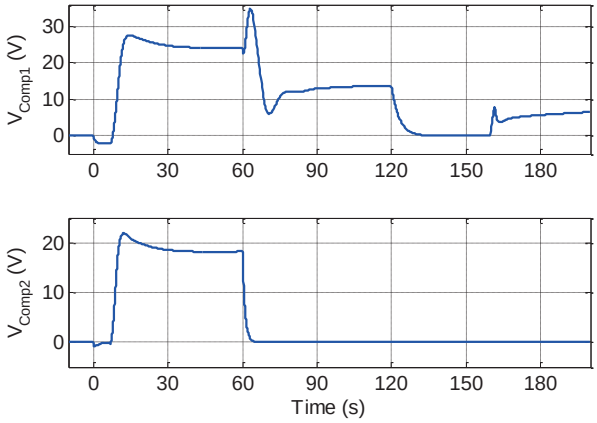

Fig. 2-26. Compensation voltages of the exciters.

2.5 Summary

This chapter presented modeling of an all-electric ship with low voltage dc power system. Averaging methods were used to model the power electronic converters by neglecting high frequency switching behavior in order to reduce the computation burden. A simulation platform was developed using the derived models of different components for system-level studies. The simulation results for a sailing profile of an

all-electric ship demonstrated the effectiveness of the simulation platform in studying dynamic behaviors of different mechanical and electrical variables. Providing significant savings in terms of time and computational intensity, the presented simulation tool could be useful for long-term and repetitive simulations that are required for research on all-electric ship dc power systems.

3
Optimized Fuel Consumption

In this chapter, detailed efficiency analysis of a shipboard dc power system is carried out. An optimization algorithm is proposed to minimize fuel consumption under various loading conditions. The studied system includes diesel engines, synchronous generator-rectifier units, a full-bridge bidirectional converter, and an energy storage device. In order to evaluate potential fuel saving provided by such a system, an online optimization strategy for fuel consumption is implemented. An Offshore Support Vessel (OSV) is simulated over different operating modes using the online control strategy. The resulted consumed fuel is compared to that of a conventional ac power system as well as of a dc power system without energy storage.

Increasing concerns on environmental issues and fuel economy have forced the maritime transport sector to pursue low emission and fuel efficient solutions. Power electronics plays a major role in optimization of the conventional drivetrains. In marine vessels, power electronic converters made a breakthrough with regard to fuel saving, when they enabled electrification of propulsion systems through Variable Speed Drives (VSDs) in 1970's [2]. The advantages gained from electric propulsion systems have ever since promoted the concept of all-electric ship, which provides a common electrical platform to supply the propulsion power and ship-service loads [47-49]. Although the overwhelming majority of present all-electric ships use ac distribution systems, the penetration of power electronic converters into power systems is giving rise to a tendency towards dc distribution systems [5-7]. The incentive for this transition lies, on the one hand, in an increasing interest in integration of energy sources and storage devices with dc outputs [6, 8], and on the other hand, in the challenges

associated with the conventional ship ac power systems. These challenges include the need for synchronization of the generation units, reactive power flow, inrush currents of transformers, harmonic currents, and three-phase unbalances. A dc power system lets the prime movers operate at their optimal speeds, leading to significant fuel saving. Shipboard dc power systems offer further advantages, such as space and weight savings, and flexible arrangement of equipment [9].

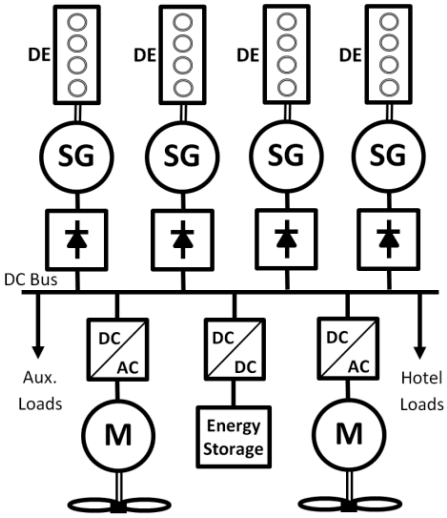

Fig. 3-1. Single-line diagram overview of the studied shipboard dc hybrid power system.

Despite the long history of hybridization and fuel saving practices in land vehicles [50-55], marine hybrid-electric vessels are almost at the beginning of their journey, particularly with regard to integration of energy storage [7, 56-60]. Presently, dc hybrid power systems are being considered for certain categories of ships that experience frequent load variations and/or long time of operation under non-rated conditions. Offshore Support Vessels (OSVs) form a major category of interest [9, 60]. The first OSVs with dc power systems were delivered in 2012, including “Jaguar” with a power system from Alewijnse [61]. ABB and Siemens launched OSVs with dc power systems in 2013. “Edda Ferd” introduced by Siemens is the first OSV with a dc hybrid power system which benefits from variable-speed diesel engines and batteries, and assures a significant fuel saving compared to the conventional diesel-electric systems.

Although extensive research has been carried out on efficiency optimization of hybrid electric vehicles [62-65], this issue for all-electric ships has largely remained unaddressed. This chapter is aimed at efficiency analysis and optimization of shipboard power systems and evaluation of their fuel saving when utilizing the dc distribution and

incorporating an energy storage device (see Fig. 3-1). Section 3.1 discusses the fuel consumption of the prime mover and its modeling. It also analyzes and models the efficiency of the electrical sources, converters, and the energy storage. In order to evaluate potential fuel saving by this system, in section 3.2, an optimization algorithm is proposed for ship applications where multiple generator sets should be optimized in terms of their average powers and power ripples. The optimization algorithm extends the work reported in [66] (that is limited to HEVs with a single generator) to all-electric ships running on multiple generator sets. The optimization algorithm minimizes the fuel consumption by optimal power sharing among the energy storage and prime movers. In section 3.3, an online optimization strategy based on the proposed algorithm is applied to an offshore support vessel with seven different operational modes. MATLAB/Simulink is used to simulate the system. The control performance deficiencies resulted from the approximations of the online control is taken into account to estimate the optimized fuel saving onboard an actual vessel. The simulation results of the online optimization control are presented and compared with those of theoretical optimization algorithm. The study results show substantial fuel saving for the optimally controlled dc hybrid power system in comparison with a conventional ac system as well as with a dc system without energy storage.

3.1 Efficiency Analysis and Modeling

Fig. 2 depicts the architecture of the studied dc power system in more detail. The power system consists of four generation units, an energy storage system based on Li-Ion batteries, propulsion loads, ship service loads, and auxiliary loads. In each generation unit, a prime mover is coupled to a wound-rotor synchronous generator. The ac power of the generator is converted to dc power through a three-phase diode rectifier. The rotational speed of the prime mover is adjusted by a local controller to minimize fuel consumption. This is not possible in conventional ship ac power systems wherein the speed reference is constant to maintain synchronization among generators. In order to manage power sharing among generators while regulating the dc voltage level, the exciters of different generation units can be coordinated by voltage droop with secondary level control. The energy storage system consists of a Li-Ion battery bank and a bidirectional dc-dc converter that enables controlled charging and discharging of the battery.

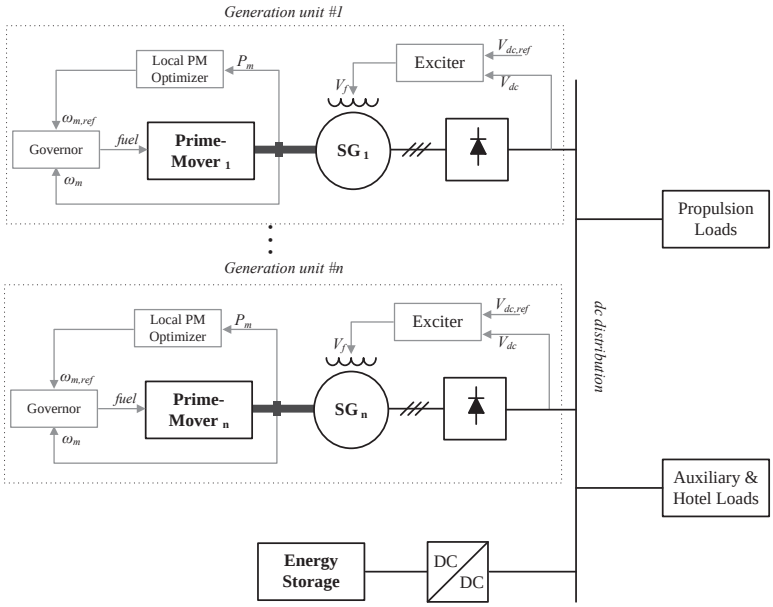

Fig. 3-2. The architecture of the power sources.

In this section, the generation units are analyzed and modeled in terms of fuel consumption of the prime movers, and efficiency of the generator-rectifier systems. In addition, the efficiencies of the battery bank and the dc-dc converter are analyzed and modeled. As the electrical load profile of the studied system is available, the efficiency models of the system loads are not required.

3.1.1 The prime mover

The main source of power onboard an all-electric ship typically comprises a synchronous generator, driven by an internal combustion engine (ICE) that is often fueled by diesel or heavy fuel oil [47]. Specific fuel consumption (SFC) curves of an internal combustion engine (ICE) can be obtained from the engine efficiency maps. Fig. 3-3 shows SFC curves of an ICE qualitatively [8]. The efficiency and emissions of ICEs are continuously being improved; however, the optimum fuel utilization factor of marine ICEs is still around 40%, and the remaining stored energy in the fuel is dissipated through heat or the exhaust.

Fig. 3-3 shows that the fuel utilization of an ICE can be improved by adjusting the engine speed based on the engine load. This implies a disadvantage of the conventional

shipboard ac power systems, wherein all generator sets must be synchronized at a fixed frequency, preventing from the optimized speed control. A dc power system, however, enables the engines to rotate independently, which consequently provide the possibility of optimal speed adjustment. In ac power systems, independent rotation of the engines could be also provided by use of back-to-back converters for each generator. Nevertheless, this entails more cost and complexity in comparison with a dc system. In addition, considerable ship electrical power is converted to dc to be used by the ship propulsion drives, which constitutes the major loads in many applications. Moreover, the use of back-to-back converters adds to the conversion stages between ac and dc, which reduces the drivetrain efficiency. Therefore, the dc system has become more appealing to the ship industry with regard to fuel saving.

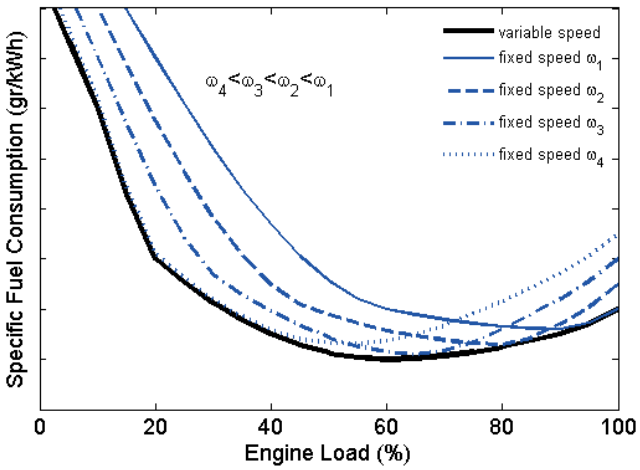

Fig. 3-3. Specific fuel consumption of an ICE.

The hourly fuel consumption curve for an ICE can be approximated by a quadratic function of the load as expressed in (3.1). This equation is valid for either variable-speed, or fixed-speed operation, using different sets of polynomial coefficients [66].

$$C_1 = C_0 + aP_m + bP_m^2. \tag{3.1}$$

Where C_0, a, and b are the coefficients of the second-order polynomial function, and P_m is the engine mechanical power. The support points for the specific fuel consumption of a 300 kW diesel engine are given in the Appendix [see B.2] under both variable and fixed-speed operations. The specific fuel consumption is the hourly consumption per

unit of power, which is obtained by (3.2).

$$SFC = C_0 / P_m + a + bP_m. \tag{3.2}$$

The above relations of fuel consumption are also valid in dynamic conditions [66].

3.1.2 The synchronous generator-rectifier system

In a shipboard power generation system, the prime mover is coupled to an electric machine, typically a synchronous generator, to convert the mechanical energy into the electrical form. When dc distribution is considered, the three-phase ac power is to be converted to dc power through three-phase rectifiers. As bidirectional power flow is not required in such an application, a three-phase diode rectifier is a preferable option due to its structural simplicity, high energy efficiency, and low cost. It can readily be used with wound-rotor synchronous generators [5, 7].

Three-phase rectifiers are already used in the conventional electric propulsion systems to supply the dc links of propulsion electric drives. The transition from ac to dc can be viewed as the enhancement of these dc links to form a distributed dc bus. This leads to elimination of bulky ac switchboards, ac transformers, and their associated power losses [8]. In addition, it will be shown in the following that the efficiency of the generator is improved, when the prime mover is controlled at its optimal speed.

The main losses of the synchronous generator consist of copper losses, iron losses, and mechanical losses. The copper losses are resulted from the current passing through the stator and rotor windings, which are calculated by (3.3).

$$P_{Cu} = r_s I_s^2 + r'_{fd} I'^2_{fd} = r_s (i_{sd}^2 + i_{sq}^2) + r'_{fd} i'^2_{fd}. \tag{3.3}$$

where conventional notations are used. The iron losses are composed of eddy and hysteresis losses, which can be obtained by (3.4) [67].

$$P_{Fe} = c_{Fe} \omega_e^{\beta} \lambda_m^2 = c_{Fe} \omega_e^{\beta} (X_{md}^2 i_{md}^2 + X_{mq}^2 i_{mq}^2). \tag{3.4}$$

where $\beta = 1.5 - 1.6$. This equation is represented in the machine equivalent circuit by the core resistance R_c in parallel to the magnetizing reactors X_{md} and X_{mq}. The mechanical losses are due to friction and air drag losses, which are proportional to the square of rotational speed.

$$P_{l,m} = c_m \omega_m^2. \tag{3.5}$$

Power losses in diode rectifiers are mainly resulted from the conduction losses, and their switching losses are negligible. The conduction losses are given by

$$P_{rec} = 2V_{fw} I_{dc} + \frac{2}{3} R_{D,on} F_I^2 I_{dc}^2. \tag{3.6}$$

where V_{fw} is the diode threshold voltage, and F_I is the current waveform factor, which can readily be calculated for the typical diode current waveforms by $F_I = I_{D,rms} / I_{D,avg}$. Assuming that each diode has a half-sine current waveform, we calculate $\pi/2$ for the current waveform factor.

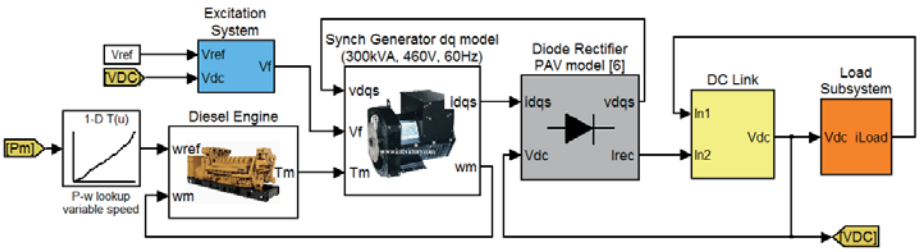

Fig. 3-4. Overview of the variable-speed control of a diesel-generator unit.

In order to evaluate the power losses in the generator-rectifier system and to obtain its efficiency curve, the simulation platform introduced in [7] is employed. The losses are investigated over a wide range of load for two conditions:

1) Engine speed is fixed at its rated value.

2) Engine speed is optimally adjusted to consume minimum fuel.

Fig. 3-4 shows the overview of the variable-speed control for one diesel engine. The optimal speed against the engine load can be deduced from the engine manufacturer's datasheet. For constant-speed operation, the reference speed is fixed at its rated value. The parameters of the diesel-generator sets are given in the Appendix [see B].

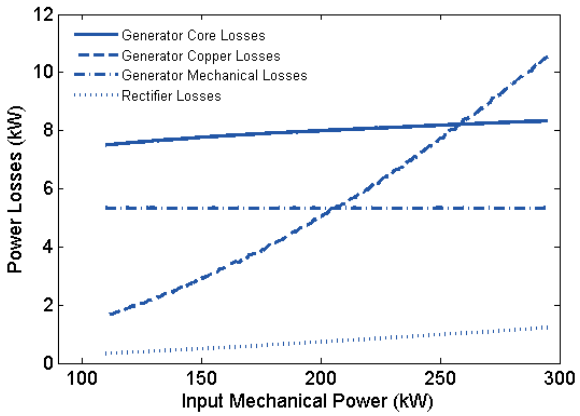

Fig. 3-5. Power losses of the generator-rectifier under fixed-speed operation

Fig. 3-5 depicts power loss components of the generator-rectifier system under fixed speed operation, while Fig. 3-6 shows the same components when the speed is varied to attain minimum SFC. Comparing the two figures, it is observed that the generator core and mechanical losses reduce in variable-speed operation, while the copper losses slightly increase. Nevertheless, the total loss reduction outweighs the increased copper losses, which results in higher efficiencies in variable-speed operation. Fig. 3-7 depicts the efficiency in the two operation modes, wherein the difference of the two efficiency curves increases as the load decreases.

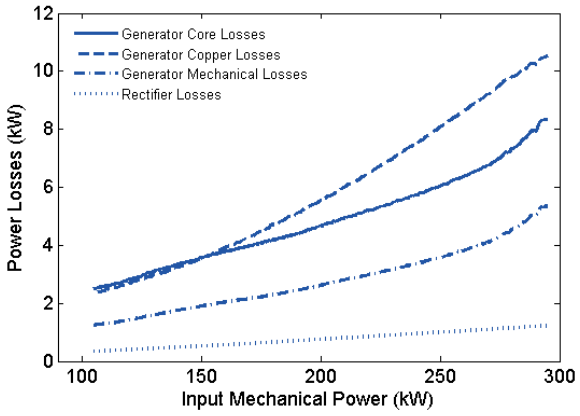

Fig. 3-6. Power losses of the generator-rectifier under adjusted-speed operation

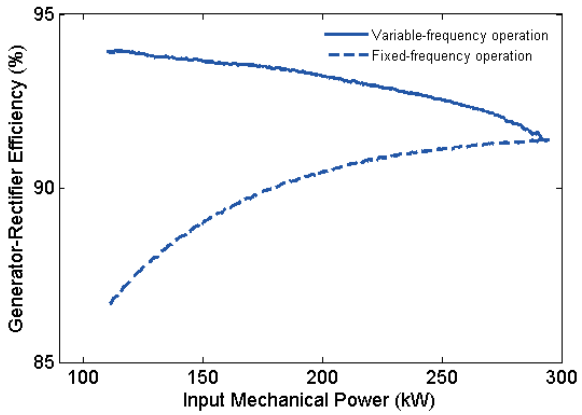

Fig. 3-7. Efficiency curves of the generator-rectifier under fixed and variable-speed operation.

The specific fuel consumption is calculated in terms of electrical load by using the efficiency curves of Fig. 3-7 and the SFC relation in (3.2). Fig. 3-8 depicts the curves of these new SFC relations for fixed and variable-speed operation, which are fitted to quadratic functions with coefficients given in the Appendix [see B.2]. These quadratic functions will be used in the development of the optimization algorithm.

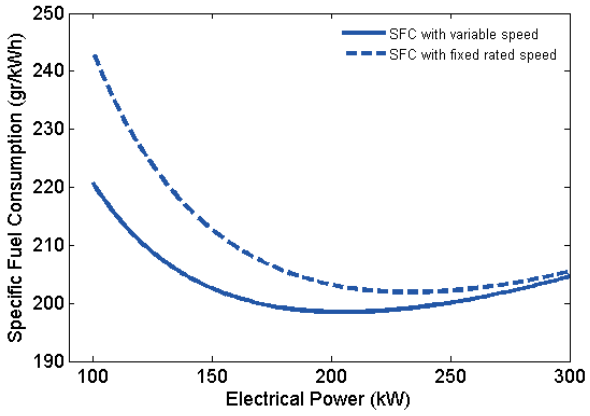

Fig. 3-8. SFC curves of the diesel-generator set in terms of electrical power under fixed and variable-speed operation.

3.1.3 The bidirectional dc-dc converter

In a dc hybrid power system, an energy storage device is prominent to improve the transient performance of the system, and to enable optimal load leveling of the sources.

A bidirectional converter is normally used to incorporate the energy storage in the power system. Various topologies of bidirectional dc-dc power converters are discussed and compared in [68] and [69]. The topological circuit of Fig. 2-2.b is considered for the bidirectional converter [70, 71]. The high frequency transformer is used to provide high voltage transfer ratio to link a low voltage battery to the dc bus. The power losses of the converter of Fig. 2-2.b for its two modes of operation are discussed in the following. The parameters of the converter are given in the Appendix [see B.1].

The converter losses are comprised of the conduction and the switching losses of the transistors, the conduction losses of the diodes, and the resistive losses of the inductor, the transformer, and the capacitors. The transformer core losses are neglected, as the switching frequency is relatively low. In the following, the converter losses in buck mode are formulated. The losses are preferably derived in terms of HV-side power so as to provide an efficiency curve against exchanged power with the dc bus. More details on the derivation can be found in [72]-Ch. 3.

The transistors conduction losses are obtained by (3.7), assuming that the inductor current is ripple-free.

$$P_{Sw,on} = R_{S,on} I_{S,rms}^2 = R_{S,on} \left(\frac{P_{hv} \sqrt{D}}{V_{hv}} \right)^2 . \tag{3.7}$$

Assuming that the transistor output capacitance is linear, we can calculate the switching losses by

$$P_{Sw,sw} = 4 \left(\frac{f_{sw}}{2} \right) C_O V_{SM}^2 = \frac{1}{2} f_{sw} C_O V_{hv}^2 . \tag{3.8}$$

The following equations hold for the diode conduction losses over a switching period.

$$p_D = \begin{cases} V_{fw} i_L + 2R_{D,on} i_L^2, & (0 \le t \le DT) \\ V_{fw} i_L + (2R_{D,on} \| 2R_{D,on}) i_L^2, & (DT \le t \le T) \end{cases} \tag{3.9}$$

Taking an average over the switching period, it yields

$$P_D = V_{fw} I_L + R_{D,on} I_L^2 D + 2R_{D,on} I_L^2 (1-D) = V_{fw} \left(\frac{nP_{hv}}{DV_{hv}} \right) + (2-D) R_{D,on} \left(\frac{nP_{hv}}{DV_{hv}} \right)^2 \tag{3.10}$$

The resistive losses of the passive elements are obtained by

$$P_L = r_L I_{L,rms}^2 = r_L \left(\frac{nP_{hv}}{DV_{hv}} \right)^2 . \tag{3.11}$$

$$P_{C1} = r_{C1} I_{C1,rms}^2 = r_{C1} \left(\frac{(1-D)P_{hv}}{DV_{hv}} \right)^2 . \tag{3.12}$$

$$P_{C2} = r_{C2} I_{C2,rms}^2 = r_{C2} \left(\frac{(1-D)V_{lv}}{\sqrt{12} f_{sw} L} \right)^2 . \tag{3.13}$$

$$P_T = r_T I_{T,rms}^2 = r_T \left(\frac{nP_{hv}}{V_{hv}\sqrt{D}} \right)^2 . \tag{3.14}$$

The power loss components in buck mode are depicted in Fig. 3-9, using the above formulas. Analysis of the boost mode is carried out in a similar way to the above formulation, and results in the loss components depicted in Fig. 3-10. The formulas for boost mode are summarized in the Appendix [see C].

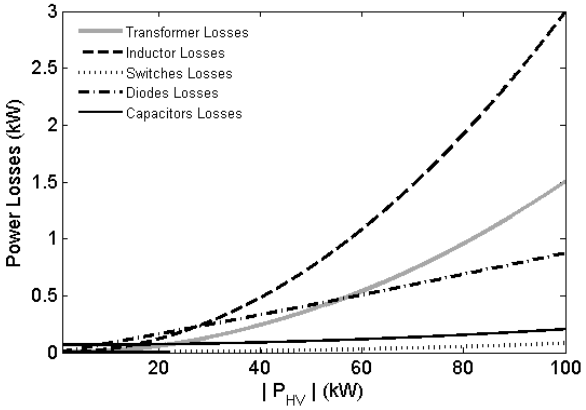

Fig. 3-9. The power loss components of the bidirectional converter in buck mode.

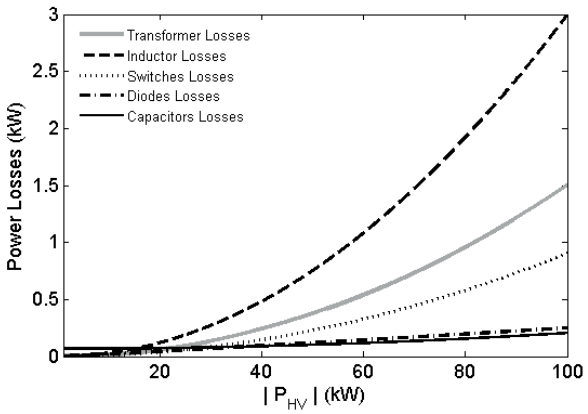

Fig. 3-10. The power loss components of the bidirectional converter in boost mode.

Fig. 3-11 shows the converter efficiency curves for the two modes, which are slightly different. An averaged efficiency curve between the two modes is considered to model the converter efficiency. This is because the converter is equally operated in both modes in order to sustain the battery charge level. The converter losses, thereafter, can be modeled by an equivalent resistance, as expressed by (3.15). This equation also includes a small constant term, resulted from constant switching losses, and capacitor losses. As seen in Fig. 3-12, the loss model of (3.15) complies with the detailed converter losses.

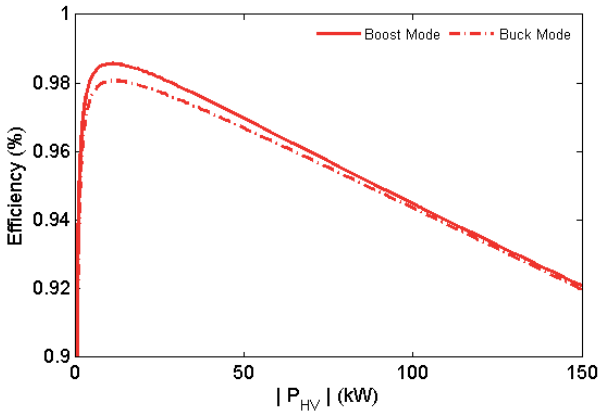

Fig. 3-11. Efficiency curves of the bidirectional converter in buck and boost modes.

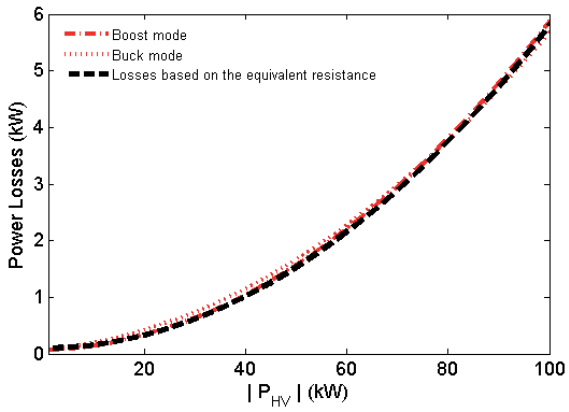

Fig. 3-12. The converter losses based on the equivalent resistance.

$$P_{l,bid} = \frac{R_{bid}}{V_{bus}^2} P_{hv}^2 + P_{l0}. \tag{3.15}$$

R_{bid} is the equivalent resistance of the bidirectional converter. In order to provide a total loss model of the energy storage system, battery losses can be integrated in the converter loss model as discussed in the following.

3.1.4 The battery model

To develop an optimization control strategy, a reference model of the battery is essential. Electrochemical battery models [73-75] can often provide high accuracy by capturing all key behaviors of the electrochemical cells. These models are based on partial differential equations with large number of unknown parameters. Therefore, they could lead to unnecessary complex models for the purpose of power management control.

Equivalent circuit battery models have been widely used for the purpose of power management studies. They are lumped models with relatively small number of parameters. A number of these equivalent circuit models are studied in [76] for Li-Ion batteries. As the battery SOC in the current research is maintained within a narrow range of high SOC values, the simple model presented in [76] is chosen. This simple model is a SOC-dependent voltage source in series with an equivalent resistance.

The above-mentioned battery model is used only for the analytical derivation of the

optimization strategy. However, for the system simulation, the battery model of the Simulink library is used. The details of the Simulink battery model can be found in [77]. The internal resistance of a Li-Ion battery bank rated at 80 V and 1000 Ah is 0.8 mΩ which is calculated through the user interface of the Simulink model. Such a small value of resistance is resulted from a high number of parallel branches of battery cells to provide the required capacity.

The power loss model of the battery, based on its equivalent resistance R_b [66], is readily integrated in (3.15) by

$$P_{l,ess} = \frac{R_{ess}}{V_{bus}^2} P_{hv}^2 + P_{l0}. \tag{3.16}$$

where R_{ess} is the equivalent resistance of the energy storage system that is expressed by

$$R_{ess} = R_{bid} + \frac{n^2}{(1-D)^2} R_b. \tag{3.17}$$

The above simplified model of the energy storage system is useful in the development of the optimization algorithm that will be discussed in the next section.

3.2 Optimization algorithm

The presence of more sources of power causes more complexity in power management, calling for an effective strategy to coordinate the sources properly and to make an appropriate choice among different possible alternatives. Various control strategies can be devised in a hybrid power system so as to achieve desired performance goals, optimized energy efficiency, reduced emission, or improved reliability and safety. This section deals with optimization of energy efficiency, which is discussed in the following.

Fig. 3-13 compares fuel consumption of a shipboard dc power system with that of a conventional shipboard ac power system. The solid curves depict specific fuel consumption for the dc power system of Fig. 3-1, wherein “k” active diesel engines are controlled at their optimal speeds. This set of active generation units of the dc power system will be called “dc source” hereafter in this chapter. The dotted curves depict

specific fuel consumption for a conventional ac power system, wherein the same set of diesel-generators of Fig. 3-1 is used, and "k" active diesel engines operate at fixed speed. Besides the comparison, Fig. 3-13 also implies how the replacement of a high-power generation unit with a set of low-power generation units results in substantial fuel saving, especially under light-load conditions. In addition, it yields a quantitative measure to determine the optimal number of active generator sets based on the system load.

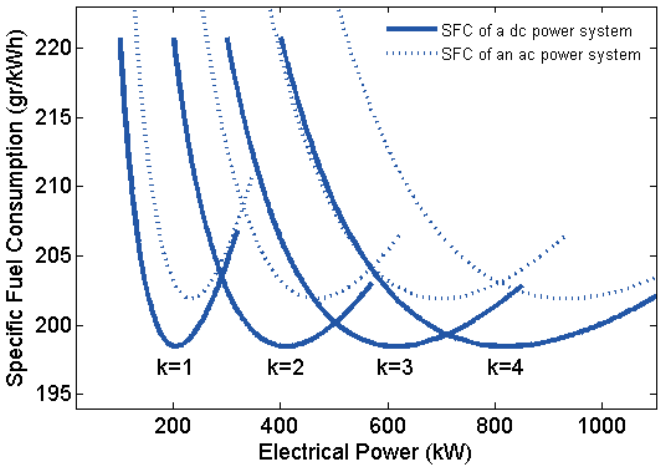

Fig. 3-13. SFC curves for "k" active diesel engines in a dc power system compared to those in the conventional ac power system.

In practice, potential large transients of the ship electrical load may require the system to continuously keep a redundant active generator set. This is already a technical requirement for several ship types including OSVs, which increases their fuel consumption considerably. In case an energy storage device is integrated in the system, it can supply the transient power until an engine start-up is really necessary. This would provide the required redundancy with no additional fuel consumption [60].

The energy storage also enables the engines to operate at their optimal conditions. It is apparent in Fig. 3-13 that the optimal fuel consumption is achieved when the engines are operated at their minimum SFC point. However, due to power losses of the energy storage, the optimal operation is not necessarily achieved by keeping the engine operating point at the minimum SFC. A compromise is to be considered between the minimum engine SFC and the maximum efficiency of the energy storage system. Besides, existing ripple of the generator load causes ripples on the engine SFC that

results in additional fuel consumption. Therefore, the power ripple of the generation units should also be optimized. This will be discussed in detail later in this section.

According to the above discussion, the optimization strategy has two main tasks: first, to calculate the optimal value for the average power of the dc source, and second, to find the optimal value for the power ripple of the dc source. This section extends the work of [66] to suit the multi-generator shipboard power system of Fig. 3-1.

The power of the dc source is expressed in terms of an average value and a ripple proportional to the load ripple.

$$P_s(t) = P_{sa} + \alpha(P_L(t) - P_{La}) \qquad (0 \le \alpha < 1). \tag{3.18}$$

where P_{sa} and P_{La} are the averaged values of the dc source power and the load respectively, and α determines the fraction of the load ripple supplied by the dc source. The remaining load ripple is to be supplied by the battery, which is also loaded by an averaged power of $P_{La} - P_{sa}$. The purpose of the following analysis is to find optimal values for P_{sa} and α.

3.2.1 Charge-discharge mode

In order to maintain the state of charge (SOC) of the battery within a certain limit, it is necessary that a diesel generator starts when SOC reaches the lower boundary, and shuts down as soon as SOC exceeds the upper limit. Therefore, two operating modes can be considered for the dc source, which are addressed here by charge mode and discharge mode. We rewrite (3.18) for the two modes of discharge and charge respectively.

$$P_{s,k}(t) = P_{sa,k} + \alpha_k(P_L(t) - P_{La}) \qquad (0 \le \alpha_k < 1). \tag{3.19}$$

$$P_{s,k+1}(t) = P_{sa,k+1} + \alpha_{k+1}(P_L(t) - P_{La}) \qquad (0 \le \alpha_{k+1} < 1). \tag{3.20}$$

where k is the number of active engines in discharge mode. Fig. 3-14 shows an overview of the optimization problem. In this figure, the system is supplying a load with an average of P_{La} and ripple amplitude of $\hat{P}_L$. Charging and discharging the energy storage periodically, we can move the operating point toward lower SFCs. During the charge mode, "$k+1$" active engines supply the load while charging the battery with $P_{ch,a}$. This moves the operating point from point A to point B, reducing the SFC value. During the discharge mode, "k" engines are active and the battery is discharged with $P_{dis,a}$ in

order to assist the generators to supply the load. The operating point, in this mode, moves to point B´. In order to find the optimal operating points B and B´, the optimal average value of the dc source power can be calculated for both charge and discharge modes i.e. $P_{sa,k}$ and $P_{sa,k+1}$.

In addition, the power ripple of the dc source may also cause additional fuel consumption. It is seen in Fig. 3-14 that although the average of $P_{s,k}(t)$ is equal to $P_{sa,k}$, the average of $SFC(P_{s,k}(t))$ is greater than $SFC(P_{sa,k})$, which is a consequence of the nonlinearity of SFC curves. This means that the power ripple may cause additional fuel consumption, as the fuel consumption is proportional to the average of SFC over time. Thus, the power ripple of the dc source should be optimized as well as its average power.

Based on the foregoing discussion, the set of variables that must be optimized consists of $P_{sa,k}$, $P_{sa,k+1}$, α_k, and α_{k+1}. The solution of the optimization will be a trade-off between the minimum consumption of the dc source, and the maximum efficiency of the energy storage system. The number "k", which is the number of active engines in discharge mode, is an integer between 0 and 3 for the system under study. It is determined in such a way that P_{La} lies between the minimum SFC points of the two neighboring SFC curves.

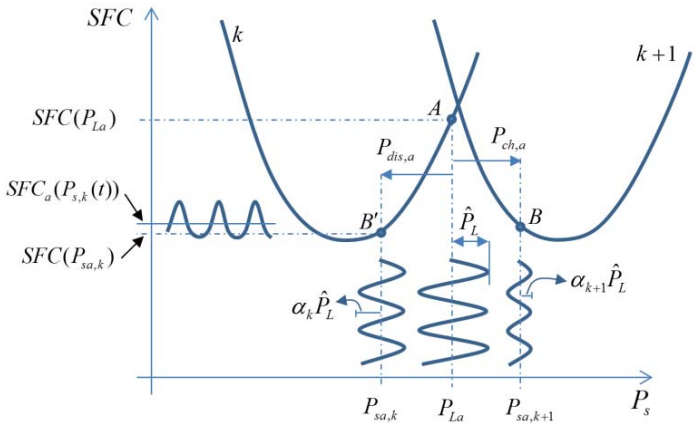

Fig. 3-14. Qualitative representation of the optimization problem.

Assuming that each charge/discharge cycle lasts for T_c, including a charge time T_{ch} and a discharge time T_{dis}, we obtain the total fuel consumption by taking integral of

(3.1) over time "t".

$$C(t) = N_{su}\{C_{0,k+1}T_{ch} + a_{k+1}\int_{T_{ch}} P_{s,k+1}(t)dt + b_{k+1}\int_{T_{ch}} P_{s,k+1}^2(t)dt + C_{0,k}T_{dis} + a_k\int_{T_{dis}} P_{s,k}(t)dt + b_k\int_{T_{dis}} P_{s,k}^2(t)dt + C_{su}\}. \quad (3.21)$$

where N_{su} is the number of engine start-ups over the time "t". An equivalent value for fuel consumption at each engine start-up is also considered which is represented by C_{su}.

The equivalent power ripple is defined by means of an integrative function "R_{eq}" that is expressed by

$$R_{eq} = \sqrt{\frac{1}{t}\int_t (P_L(t) - P_{La})^2 dt}. \quad (3.22)$$

Taking the steps provided in the Appendix [see D.1], we can derive (3.23) from the integral terms of (3.21), which yields the fuel consumption as

$$C(t) = N_{su}\{C_{0,k+1}T_{ch} + C_{0,k}T_{dis} + aP_{La}(T_{ch}+T_{dis}) + aT_{ch}\frac{R_{ess}}{V_{bus}^2}[(P_{sa,k+1}-P_{La})^2 + R_{eq}^2(1-\alpha_{k+1})^2] + aT_{dis}\frac{R_{ess}}{V_{bus}^2}[(P_{sa,k}-P_{La})^2 + R_{eq}^2(1-\alpha_k)^2] + b_{k+1}T_{ch}(P_{sa,k+1}^2 + \alpha_{k+1}^2R_{eq}^2) + b_kT_{dis}(P_{sa,k}^2 + \alpha_k^2R_{eq}^2) + C_{su}\}. \quad (3.23)$$

Considering the energy balance of the energy storage over a charge/discharge cycle, we can obtain the different time periods of T_c, T_{ch}, and T_{dis} in terms of the other variables (Appendix [see D.2], which gives

$$C(t) = t\{C_{0,k+1}D_s + C_{0,k}D_s' + aP_{La} + aD_s\frac{R_{ess}}{V_{bus}^2}[(P_{sa,k+1}-P_{La})^2 + R_{eq}^2(1-\alpha_{k+1})^2] + aD_s'\frac{R_{ess}}{V_{bus}^2}[(P_{sa,k}-P_{La})^2 + R_{eq}^2(1-\alpha_k)^2] + b_{k+1}D_s(P_{sa,k+1}^2 + \alpha_{k+1}^2R_{eq}^2) + b_kD_s'(P_{sa,k}^2 + \alpha_k^2R_{eq}^2) + \frac{C_{su}}{T_c}\}. \quad (3.24)$$

where $D_s = 1 - D_s' = T_{ch}/T_c$ is calculated by

$$D_s = \frac{P_{La} - P_{sa,k} + \frac{R_{ess}}{V_{bus}^2}[(P_{sa,k} - P_{La})^2 + R_{eq}^2(1-\alpha_k)^2]}{P_{sa,k+1} - P_{sa,k} - \frac{R_{ess}}{V_{bus}^2}[(P_{sa,k+1} - P_{sa,k})(P_{sa,k+1} + P_{sa,k} - 2P_{La}) + R_{eq}^2(\alpha_{k+1} - \alpha_k)(\alpha_{k+1} + \alpha_k - 2)]} \tag{3.25}$$

The fuel consumption represented by (3.24) has a minimum that satisfies

$$\frac{\partial C}{\partial \alpha_k} = 0, \quad \frac{\partial C}{\partial \alpha_{k+1}} = 0, \quad \frac{\partial C}{\partial P_{sa,k}} = 0, \quad \frac{\partial C}{\partial P_{sa,k+1}} = 0. \tag{3.26}$$

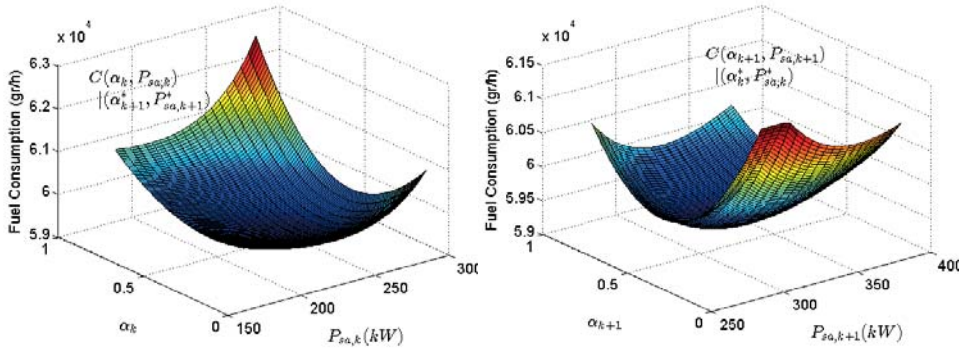

(a) (b)

Fig. 3-15. Hourly fuel consumption of the dc source under a certain load, a) in terms of loading conditions in discharge mode, b) in terms of loading conditions in charge mode.

Fig. 3-15 depicts the hourly fuel consumption of the dc power system under a certain load in terms of the dc source loading conditions. As the hourly fuel consumption has a five dimensional surface, it is represented in terms of only one pair of (α, P_{sa}) at each time, assuming the other pair to be fixed at(α^*, P^*_{sa}). Therefore, two separate graphs are used to depict the fuel consumption against the two pairs. The optimal values of $P_{sa,k}$, $P_{sa,k+1}$, α_k, and α_{k+1} can numerically be obtained by searching for the minimum fuel consumption in the analytical relation (3.24).

3.2.2 Continuous mode

The obtained optimal loading conditions must also satisfy the limits on the engine duty cycle "D_s". The resulted duty cycle must be a value between 0 and 1; otherwise the dc source operates at a continuous mode. In case the resulted duty cycle is less than or

close to zero, the dc source operates with "*k*" active diesel engines continuously, and if the duty cycle is greater than or close to one, the dc source continuously operates with "*k+1*" active engines.

In such conditions, the optimal values can be analytically attained by

$$P_{sa,j} = P_{La} + \frac{V_{bus}^2}{2R_{ess}} - \frac{1}{2}\sqrt{\frac{V_{bus}^4}{R_{ess}^2} - 4R_{eq}^2(1-\alpha_j)^2}. \tag{3.27}$$

$$\alpha_j = 1 - \frac{b_j V_{bus}^2 / R_{ess}}{\sqrt{4b_j^2 R_{eq}^2 + (a_j + 2b_j P_{La} + b_j V_{bus}^2 / R_{ess})^2}}. \tag{3.28}$$

where $j = \begin{cases} k, & D_s \le 0 \\ k+1, & D_s \ge 1 \end{cases}$

In the following section, the algorithm will be used in an online optimization strategy for an offshore support vessel at its different modes of operation.

3.3 Online optimization strategy

The optimization algorithm presented in the previous section should be tailored to suit online computations and control. In the theoretical approach, analytical definitions for some variables are, as such, dependent on the future data of the system, for example the equivalent power ripple R_{eq} and the average power P_{La}. As future data is not available in online computations, these variables need to be estimated. In addition, the online processing requires reduced computational intensity to perform the tasks in real time. This can be provided by reducing the step sizes in online processing when searching for optimal values of $P_{sa,k}$, $P_{sa,k+1}$, α_k, and α_{k+1}. These estimations and simplifications may deteriorate the effectiveness of the method. In order to evaluate the performance of the method under online operation, this section presents the simulation results of the online control in comparison with those of the offline theoretical algorithm.

An online control, based on the theoretical algorithm is used in simulation of an offshore support vessel over a number of operational modes. The parameters of the system are reported in the Appendix [see B]. The power demands at each of the operating modes are specified in Table 3.1, where the number of active engines, average

power, load fluctuation, and duration for each mode are given. These data are deduced from the experiences of ABB and DNV reported in [8, 60].

TABLE 3.1
PARAMETERS OF THE SHIP OPERATING MODES

Operating mode	# of active CEs	P_{La} (%)	P_{Lp} (%)	Duration (hr)
Low Dynamic Positioning (LDP)	2	33	20	7.5
High Dynamic Positioning (HDP)	3	53	20	4
Anchor Handling (AH)	3	50	2	1.5
Harbor (H)	1	17	1	1.5
Bollard Pull (BP)	4	66	2	0.5
Transit Towing (TT)	4	72	1	3
Transit Supply (TS)	2	33.5	1	6

For each mode of operation, the algorithm outputs the optimal loading conditions of the dc source, i.e. $P_{sa,k}$, $P_{sa,k+1}$, α_k, and α_{k+1}, and also the control mode (charge-discharge or continuous). The algorithm suggests the continuous mode when the operating point of the dc source is close to the minimum SFC; otherwise it suggests the charge-discharge mode as the optimal mode. While the offline algorithm uses a step-size of 0.01 in search for optimal α_k and α_{k+1}, requiring 100 steps, the online algorithm uses a step-size of 0.05, which needs 20 steps. This provides significant reduction in computational intensity in search for optimal α_k and α_{k+1}. The number of steps in search for $P_{sa,k}$ and $P_{sa,k+1}$ is considered 20 in both online and offline processing. Another difference between the offline algorithm and the online control is related to estimation of the load average P_{La}, and the equivalent power ripple R_{eq}. As the future data for these variables are not available, their online estimate can be obtained through filtering their instantaneous values by

$$P_{La}(s) = \frac{1}{1+sT} P_L(s). \tag{3.29}$$

$$R_{eq}^2(s) = \frac{1}{1+sT} (P_L(s) - P_{La}(s))^2. \tag{3.30}$$

where the filter time constant "T" should properly be chosen. A too short time constant may cause unnecessary engine start-stops, when a change occurs in the load profile. A too long time constant may cause that the dc source operates under non-optimal conditions for an unnecessary long period of time after a step change occurs in the system load. The choice of the time constant is critical considering that the load variations might have extremely low frequencies in ship applications, e.g. in low

dynamic positioning mode. In order to adapt to various situations, two different time constants have been considered in the simulations. When a change happens in the load profile, e.g. changes in ship operating mode, the system selects the short time constant throughout the transition time to follow the load average quickly. In the normal operation at each mode, the control system uses the larger time constant that results in more efficient control. The mode transition is detected by observing a monotonic change in the load average for some seconds. Repeated simulations have shown that suitable values for the short and long time constants are 300s and 1000s respectively. Fig. 3-16 shows the simulation results of the optimized shipboard dc power system at three modes of harbor, high dynamic positioning, and transit supply. It is observed that in harbor and transit supply modes, one of the diesel engines periodically turns on and off. This is the control mode that we earlier called "charge-discharge mode". The battery state of charge (SOC) is bounded between 60 and 80 percent. The energy storage system periodically charges and discharges with optimum average values, and also supplies an optimum fraction of the power ripple. In high dynamic positioning mode, in which the load average is close to the rated conditions, the system operates at "continuous mode", and the energy storage system only supplies an optimum fraction of the power ripple. At the bottom of Fig. 3-16, there is a flag indicating whether the control mode is "charge-discharge" or "continuous".

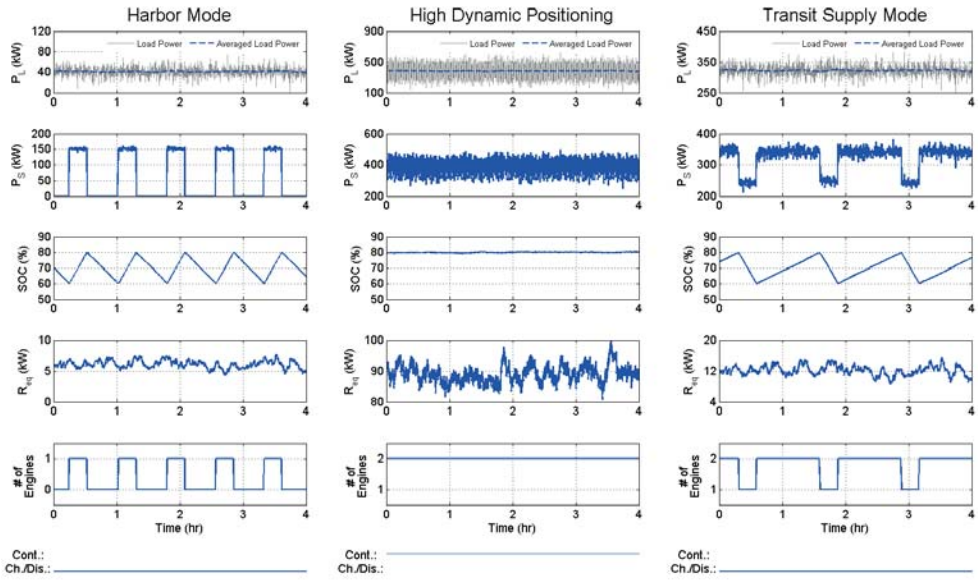

Fig. 3-16. Simulation results for three operating modes of the shipboard hybrid power system with online optimization.

Simulation results over an operating cycle consisting seven different modes are presented in Fig. 3-17. The operating modes over the cycle are indicated on top of the figure. The upper plot shows the instantaneous and average load power. The dual time-constant characteristic of the filter is particularly clear in low dynamic positioning (LDP). At the beginning of the LDP mode, shortly after the mode transition, the average power follows the instantaneous value, as the smaller time constant is chosen. Thereafter, when the transition is completely over, the larger time constant is selected in order to filter the extremely low frequency variations. This procedure is carried out at all mode transitions.

During harbor, transit towing, and transit supply, the control system operates at charge-discharge mode, as periodical changes in the number of active engines and the battery SOC are observed. During the rest of ship operating modes, the control system operates at continuous mode, and the battery mainly contributes in supplying the power ripple.

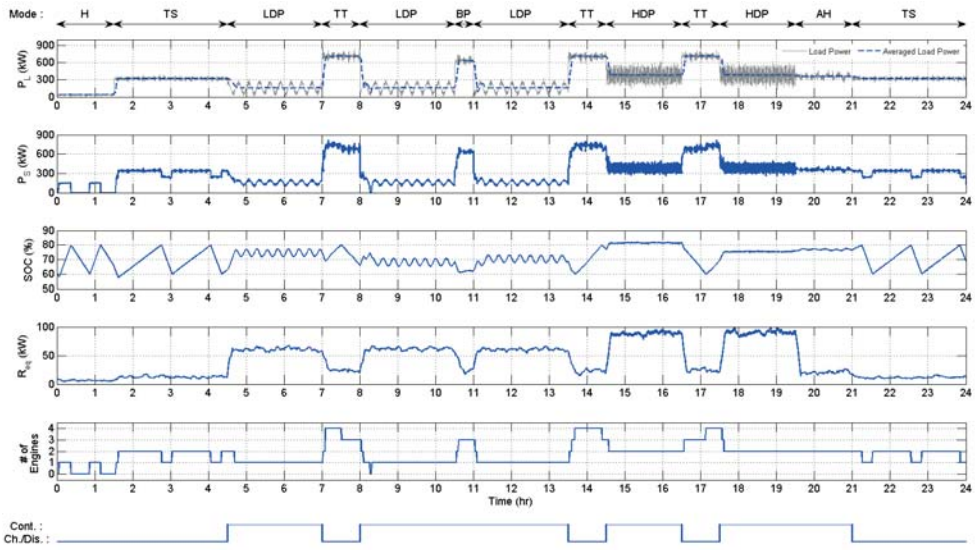

Fig. 3-17. Simulation results of the optimized shipboard hybrid power system over an operation cycle with 7 modes.

Table 3.2 presents the optimized fuel consumption in comparison with non-optimized dc and ac systems. It also compares fuel consumption results for the online optimization method with the offline at different ship operating modes.

TABLE 3.2
FUEL CONSUMPTION BASED ON THE ALGORITHM AND THE SIMULATION COMPARED TO NON-OPTIMIZED SYSTEMS

		DC system with ESS (Optimized)							DC w/o ESS	AC
Operating mode	**Control mode**	**# of active engines**	**$P_{sa,k+1}$ (%)**	**$P_{sa,k}$ (%)**	**α_{k+1}**	**α_k**	**C_{opt} (gr/h) (algorithm)**	**C_{opt} (gr/h) (simulation)**	**C_{DC} (gr/h)**	**C_{AC} (gr/h)**
LDP	Cont.	1	66.0	N/A	0.39	N/A	3.19E+04	3.32E+04	3.79E+04	4.32E+04
HDP	Cont.	2	N/A	79.0	N/A	0.49	7.59E+04	7.69E+04	7.95E+04	8.51E+04
AH	Cont.	2	N/A	75.0	N/A	0.49	7.17E+04	7.22E+04	7.58E+04	8.17E+04
H	Ch./dis.	1/0	62.8	N/A	0.36	N/A	9.83E+03	1.16E+04	1.35E+04	1.69E+04
BP	Cont.	3	N/A	75.3	N/A	0.78	1.26E+05	1.27E+05	1.28E+05	1.33E+05
TT	Ch./dis.	4/3	77.2	94.6	0.77	0.72	1.38E+05	1.38E+05	1.38E+05	1.43E+05
TS	Ch./dis.	2/1	71.2	100	0.61	0.44	6.47E+04	6.50E+04	7.64E+04	8.68E+04

The fuel consumption of the simulation is slightly higher compared to the algorithm, which is caused by estimations of (3.29) and (3.30) as well as the step-size reductions in search for the optimal loading conditions. The fuel saving achieved by the optimization method is shown in percentage in Fig. 3-18. The optimization method provides more fuel saving in those modes whose power demand is away from the rated conditions. These modes include harbor, transit supply, and low dynamic positioning modes. Due to approximations made in the online optimization, the resulted fuel saving of the simulation is less than that of the algorithm by approximately 1% in average. The difference between the performances of the simulation and the algorithm peaks at harbor mode. This is mainly resulted from the steep SFC characteristic over the low-power range which the harbor mode belongs to. This makes the harbor mode more sensitive to the errors resulted from the approximations made in the online processing. However, due to the low-power characteristic of the harbor mode, it has a minor effect on the overall performance of the online control.

The presented results in Fig. 3-18 show an average fuel saving of 15.3% for online control simulation when the conventional shipboard ac power system is replaced by a dc hybrid power system. This percentage is calculated based on weighted averaging of consumed fuel of the seven different operating modes. The system simulation over the 24-hr cycle results in even a slightly higher fuel saving of 15.8%.

Fig. 3-18 also shows that integration of an energy storage system into the dc power system can provide a fuel saving of 7.3%. The achieved fuel saving is resulted partly from optimization of the number of active engines and partly from optimization of loading conditions of the diesel-generators. The study results demonstrate a significant

potential in fuel saving of offshore support vessels through transition from ac to dc power systems and integration of energy storage devices. The fuel saving potential is not limited to the studied type of ships, but can be also considered for a wide range of marine vessels that have frequent load variations or long-time operation under non-rated conditions.

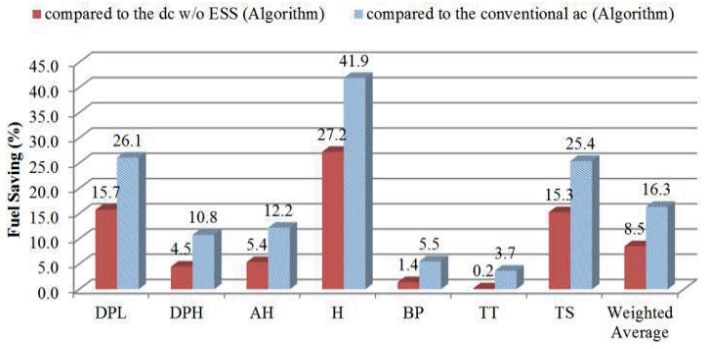

(a)

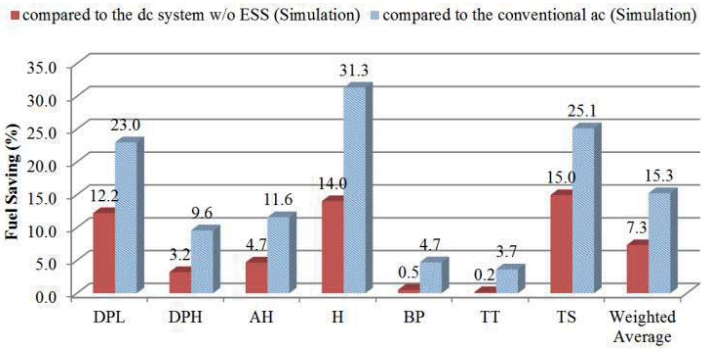

(b)

Fig. 3-18. Resulted fuel saving from the optimization strategy, a) algorithm results, b) online simulation results

3.4 Summary

In this chapter, detailed efficiency analysis of a shipboard dc hybrid power system was carried out in order to evaluate its potential fuel saving. It was shown that maximum fuel saving conditions for such a system required the generator sets to operate

at optimal loading conditions in terms of average power and power ripple. A numerical optimization algorithm was proposed to find optimal loading conditions, using the presented analysis. In addition, the optimization algorithm determined whether the generator sets operated at continuous mode or periodical charge/discharge mode. In order to evaluate the actual fuel saving provided by the method when processing online, the algorithm was used in simulation of an Offshore Support Vessel (OSV) over seven operating modes. Although the online optimization had slightly less efficiency than the algorithm by around 1%, it provided an average fuel saving of over 15 % compared to the conventional ac systems. The study also showed that the shipboard dc system with energy storage could provide a fuel saving of more than 7% compared to the dc system without energy storage. The study results demonstrate significant fuel-saving potentials in maritime sector, particularly in the category of marine vessels that experience frequent load variations or long-time operation under non-rated conditions.

4
Global Stability Control

This chapter proposes a robust large-signal stabilization technique for dc networks considering potential measurement and parameter uncertainties. The proposed technique expands the global stability margins, while keeping the benefits of the reduced-size capacitors. To validate the method, simulation and experimental results are presented for a power electronic based dc network that consists of a voltage source inverter driving a permanent magnet synchronous motor, a bidirectional boost converter incorporating a super-capacitor, and a buck converter supplying a resistive load.

Stability is an essential issue for dc power systems with power electronic-based components due to the potential for negative impedance instabilities. These instabilities are resulted from the tendency of power electronic converters to behave as constant power loads. The stability analysis of dc distribution systems can be traced back to 1970's, when Middlebrook introduced his filter design criterion for dc/dc converters [78, 79]. Using linear system theory, he proposed an input impedance criterion for the converter to prevent from unstable oscillations. This criterion leads to conservative designs, which often result in unnecessary large capacitances and expensive solutions. More recent researches have sought less conservative criteria e.g. GMPM [80], ESAC [81], and RESC [82] which provide more efficient designs [80-86]. Applying linear system theory, these criteria assure small signal stability, as they use linearized model of the system. Large signal stability analysis has also been addressed for power electronic-based dc power systems [87-92]. [87] and [92] have developed global stability analysis

tools to evaluate the system response to large signal disturbances.

The recent advancements in the stability analysis of dc power systems enable efficient and cost-effective design of the system parameters. These efficient design approaches, as opposed to the conservative ones, allow reduced sizes for passive elements to provide savings in cost, weight, and space. However, the reduction of the dc-link capacitance can have negative impacts on the system stability margins. In order to ensure high stability margins, while reducing the dc-link capacitor size, different stabilization methods have been proposed [93-100]. These methods implement a feedback term in the load control loop to eliminate the oscillatory behavior and improve the stability margins. Small signal stability analysis and control have been extensively reported in the literature [100-109]. Different methods of dc-link voltage stabilization are proposed in [100, 107, 109], which enable reduction of dc-link electrolytic capacitors. [102-105, 108, 110] have researched the small signal stability of dc microgrids, and have proposed linear controllers to ensure local stability. Islanded microgrids, such as aircraft and shipboard power systems, are subject to large signal disturbances when changing their operating modes. A single operating point (or equilibrium) cannot normally be considered for such systems. Therefore, a global stability study of these systems is usually desirable. Large signal stabilization techniques can provide them an improved global stability. In [111-114], the large signal stability has been considered, and global stabilization approaches have been proposed. [115] proposes a design criteria for a class of power converters based on nonlinear stability analysis. [116] proposes to apply amplitude death methods to the stabilization problem of dc grids. These papers study the case of two cascaded dc systems, and applicability of these methods to multi-converter dc systems still needs to be explored. The work of [117] proposes a global stabilization technique for a multi-load dc network by use of the Lyapunov theory.

A common point in the above-mentioned stabilization methods is introduction of an extra feedback term in the control system to stabilize the power system. This stabilizing feedback is a function of system variables and parameters. Therefore, errors of measurements and parameters uncertainties may affect the stabilization performance. This paper proposes a large signal stabilization technique for multi-converter dc networks that is robust to the potential measurement errors and parameters uncertainties.

This chapter is structured as follows. In section 4.1, the system overview and modeling are presented. Section 4.2 provides a formulization of the stability problem with consideration of measurement errors and parameter uncertainties. To analyze the stability of the resulted nonlinear model, and to design a robust stabilization control, Takagi-Sugeno multi-modeling approach [118, 119] is used together with robust pole

placement. A feedback vector of stabilizing powers is derived that is superposed on power references of different loads of a dc network to improve global stability of the system. In sections 4.3 and 4.4, the proposed method is validated through simulation and experimental results, respectively.

4.1 System overview

To study the stability of dc power systems, a dc grid test-bed is implemented which consists of a dc voltage source that supplies three different power electronic-based loads. The first load is a voltage source inverter driving a permanent magnet synchronous motor (PMSM). The second load is a buck converter supplying a resistive load. The third one is a supercapacitor that is connected to the main dc bus through a bidirectional boost converter. Different types of power electronic converters have been used to examine the proposed method for different load types. Fig. 4-1 shows an overview of the dc power system.

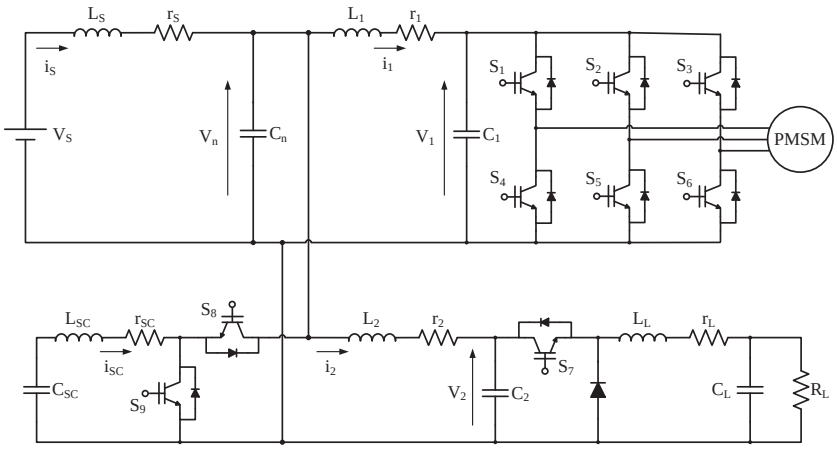

Fig. 4-1. Schematic overview of the studied dc network.

In an onboard dc network, particularly in marine and aeronautic applications, the power source is usually located far away from the points of loads. The long cables

between the source and the loads lead to inductive effects that should be considered in the stability studies. Such inductive effects form the inductance L_S. The inductors L_1 and L_2 are basically the inductors of the input filters of the converters, but the mentioned inductive effects can also contribute to their values. The resistivity of the inductors is also considered as represented in Fig. 4-1. The capacitor C_n is connected across the main dc bus, and the capacitors C_1 and C_2 are parts of the LC filters of the converters.

4.1.1 Control system

The presence of various controllable units in the dc network provides more flexibility in the control system, while it causes more complexity as well. Different control strategies can be devised in the dc network of Fig. 4-1 so as to achieve desired performance goals, optimized energy efficiency, increased reliability, and improved stability. The hierarchical control architecture is common in different applications with a variety of objectives [3, 7, 120-122]. The upper control level is basically dedicated to overall system supervision. [7, 121] use hierarchical control to regulate the dc voltage while performing power management. In [123], a supervisory control system uses fuzzy logic for energy management purposes. In this chapter, a hierarchical control system is used for the purpose of stability improvement. Fig. 4-2 shows the block diagram overview of a hierarchical control system. On the primary control level, each unit is controlled by its own local controller. The well-known vector control method is used to control the PMSM drive through commanding the gate signals S_1 to S_6. The inner control loops of the dc-dc converters use Proportional-Integrator controllers that output appropriate duty cycles to control their powers. The gate signals S_7, S_8, and S_9 are generated through pulse-width modulation of the duty cycles d and d_{sc}. The active stabilization takes place on the secondary control level, which provides references for the local controllers. The outer control loop is designed through Takagi-Sugeno (TS) multi-modeling approach [119] combined with robust pole placement. The design procedure will be discussed in detail in section 4.2.

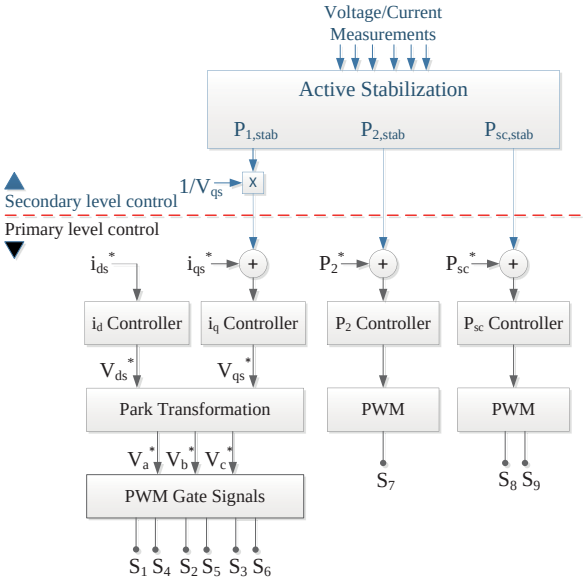

Fig. 4-2. Block diagram of the control system.

4.1.2 System modeling

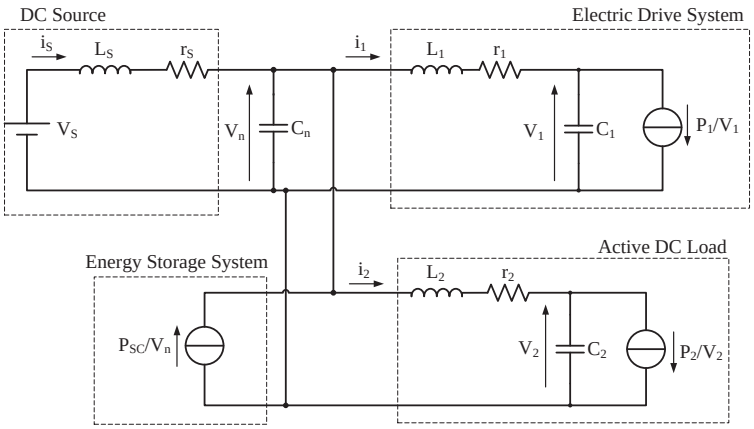

Fig. 4-3. Equivalent Circuit of the dc network under study.

The local controllers of the dc network tightly regulate their output objectives. The feature of tight regulation of the power electronic converters creates a destabilizing effect in dc microgrids. This phenomenon is called negative impedance instability in the literature [124-126]. The tight regulation characteristic of the converters makes the converters behave as instantaneous constant power loads (CPLs). To analyze the

stability of the dc network to instantaneous constant power characteristic of active loads, each converter and its associated local controller is modeled as a constant power load as shown in Fig. 4-3.

The dc system of Fig. 4-3 can be represented by the set of differential equations of (4.1), which has three nonlinearities in the capacitor voltage differential equations. These nonlinear terms are resulted from the three tightly regulated power electronic converters. P_{sc} is the power supplied by the supercapcitor through its associated boost converter. P_1 is the power consumed by the PMSM motor through its voltage source inverter, and P_2 is the consumed power by the resistive load through its buck converter.

$$\begin{cases} L_s \dfrac{di_s}{dt}(t) = -r_s i_s(t) - V_n(t) + V_s(t) \\ L_1 \dfrac{di_1}{dt}(t) = -r_1 i_1(t) - V_1(t) + V_n(t) \\ L_2 \dfrac{di_2}{dt}(t) = -r_2 i_2(t) - V_2(t) + V_n(t) \\ C_n \dfrac{dV_n}{dt}(t) = i_s(t) - i_1(t) - i_2(t) + \dfrac{P_{sc}}{V_n(t)} \\ C_1 \dfrac{dV_1}{dt}(t) = i_1(t) - \dfrac{P_1}{V_1(t)} \\ C_2 \dfrac{dV_2}{dt}(t) = i_2(t) - \dfrac{P_2}{V_2(t)} \end{cases} \tag{4.1}$$

Each variable of (4.1) can be assumed as the sum of its steady-state value and a variation around it, and can be expressed in the form of $r(t) = r_0 + \tilde{r}(t)$. After moving the operating point to the origin, the state-space model of the system is represented by (4.2).

$$\dot{\mathbf{x}}(t) = \mathbf{A}\mathbf{x}(t) + \mathbf{B}\mathbf{u}(t) \tag{4.2}$$

where state matrices, state variables, and state vector are given in (4.3)-(4.6).

$$\mathbf{x} = [x_1 \quad x_2 \quad x_3 \quad x_4 \quad x_5 \quad x_6]^t \tag{4.3},$$

$$\begin{cases} x_1(t) = i_s(t) - i_{s0} \\ x_2(t) = i_1(t) - i_{10} \\ x_3(t) = i_2(t) - i_{20} \\ x_4(t) = V_n(t) - V_{n0} \\ x_5(t) = V_1(t) - V_{10} \\ x_6(t) = V_2(t) - V_{20} \end{cases} \tag{4.4}$$

$$\mathbf{A}=\begin{bmatrix} \frac{-r_s}{L_s} & 0 & 0 & \frac{-1}{L_s} & 0 & 0 \\ 0 & \frac{-r_1}{L_1} & 0 & \frac{1}{L_1} & \frac{-1}{L_1} & 0 \\ 0 & 0 & \frac{-r_2}{L_2} & \frac{1}{L_2} & 0 & \frac{-1}{L_2} \\ \frac{1}{C_n} & \frac{-1}{C_n} & \frac{-1}{C_n} & 0 & 0 & 0 \\ 0 & \frac{1}{C_1} & 0 & 0 & 0 & 0 \\ 0 & 0 & \frac{1}{C_2} & 0 & 0 & 0 \end{bmatrix} \quad (4.5), \qquad \mathbf{B}=\begin{bmatrix} 0 & 0 & 0 \\ 0 & 0 & 0 \\ 0 & 0 & 0 \\ \frac{-1}{C_n} & 0 & 0 \\ 0 & \frac{1}{C_1} & 0 \\ 0 & 0 & \frac{1}{C_2} \end{bmatrix} \quad (4.6)$$

The input vector **u** is expressed by (4.7) that includes three nonlinear functions.

$$\mathbf{u}(t)=\begin{bmatrix} u_1(t) \\ u_2(t) \\ u_3(t) \end{bmatrix}=\begin{bmatrix} \frac{P_{sc}}{V_{n0}}\cdot\frac{1}{V_{n0}+x_4}x_4 \\ \frac{P_1}{V_{10}}\cdot\frac{1}{V_{10}+x_5}x_5 \\ \frac{P_2}{V_{20}}\cdot\frac{1}{V_{20}+x_6}x_6 \end{bmatrix} \quad (4.7)$$

The system parameters are given in Table 4.1. Large inductance values have been chosen to provide unstable conditions at low-power levels that suit the small-scale laboratory test-bed. Fig. 4-4 shows the measured system variables when stabilization loop is opened. It illustrates that the dc network without stabilization is susceptible to unstable oscillations. In the next section, we will deal with designing of a robust global stabilizer that improves the stability margins of the system.

TABLE 4.1
PARAMETERS OF THE DC NETWORK

Converters Parameters:		***PMSM Parameters:***
V_S = 200 V	L_1 = 40 mH	*Pole pairs* = 4
r_S = 0.4 Ω	L_2 = 19.6 mH	*Stator resistance* = 0.5 Ω
L_S = 17.3 mH	C_1 = 500 μF	*Stator inductance* = 3.1 mH
C_n = 1050 μF	C_2 = 1050 μF	*Torque constant* = 0.572 Nm/A
r_1 = 0.8 Ω	C_{sc} = 165 F	*Friction constant* = 14 gm^2/s
r_2 = 0.42 Ω	L_{sc} = 1 mH	*Inertia constant* = 3.7 gm^2

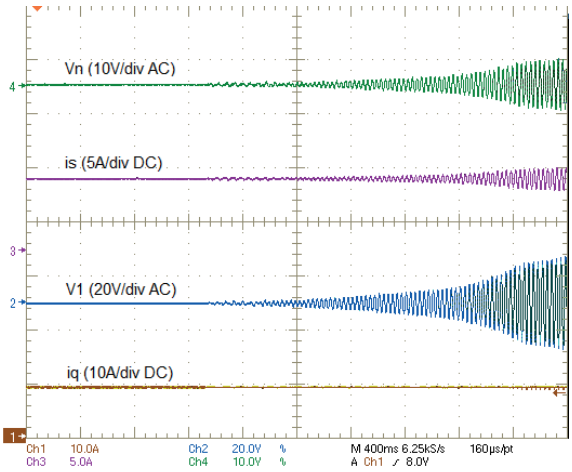

Fig. 4-4. Measured variables of the dc network without stabilization control ($i_q = 9A$, $P_2 = 300\ W$, $P_{SC} = 0\ W$).

4.2 Stability study

4.2.1 Active stabilization

The system of Fig. 4-3, in its original state, becomes unstable if the power demands of the loads exceed certain limits. The stability margins, however, can be improved through active stabilization methods. Active stabilization eliminates the need for firmware modifications that lead to inefficient and costly solutions. Different stabilization methods have been proposed [93-98] to improve stability margins, while maintaining reduced capacitor sizes. They introduce a stabilizing feedback in the load control loop to moderate the oscillatory behavior and improve the stability. The preceding researches have often studied small signal stabilization that concern local stability only. Large signal stabilization has also been reported in the literature including [111-114], which propose global stabilization approaches. These papers deal with the stability problem in case of two cascaded dc systems. In [117], a global stabilization technique is proposed for a multi-load dc network. The stabilizing feedback in the latter paper is dependent on the system variables. Measurement uncertainties which may affect the stabilization performance, has not been addressed in the above paper. In this section, a robust global stabilization technique is discussed that takes into account the

measurement errors as well as uncertainties in the parameters.

4.2.2 Measurement uncertainties

Assuming each load can absorb a stabilizing power that is small compared to the nominal power values, the state equations referred to the origin are obtained by (4.8).

$$\begin{cases} L_s \dfrac{dx_1}{dt}(t) = -r_s x_1(t) - x_4(t) \\ L_1 \dfrac{dx_2}{dt}(t) = -r_1 x_2(t) - x_5(t) + x_4(t) \\ L_2 \dfrac{dx_3}{dt}(t) = -r_2 x_3(t) - x_6(t) + x_4(t) \\ C_n \dfrac{dx_4}{dt}(t) = x_1(t) - x_2(t) - x_3(t) + \dfrac{P_{sc} x_4(t)}{(x_4(t) + V_{n0}) V_{n0}} - \dfrac{P_{sc,stab}}{x_4(t) + V_{n0}} \\ C_1 \dfrac{dx_5}{dt}(t) = x_2(t) + \dfrac{P_1 x_5(t)}{(x_5(t) + V_{10}) V_{10}} - \dfrac{P_{1,stab}}{x_5(t) + V_{10}} \\ C_2 \dfrac{dx_6}{dt}(t) = x_3(t) + \dfrac{P_2 x_6(t)}{(x_6(t) + V_{20}) V_{20}} - \dfrac{P_{2,stab}}{x_6(t) + V_{20}} \end{cases} \tag{4.8}$$

where $P_{sc,stab}$, $P_{1,stab}$, and $P_{2,stab}$ are the mentioned stabilizing powers that are absorbed by the active loads. The control vector u(t) in this case is expressed by (4.9).

$$\mathbf{u}(t) = \begin{bmatrix} u_1(t) \\ u_2(t) \\ u_3(t) \end{bmatrix} = \begin{bmatrix} \dfrac{P_{sc} x_4(t) - P_{sc,stab}(t) V_{n0}}{V_{n0} V_n(t)} \\ \dfrac{P_1 x_5(t) - P_{1,stab}(t) V_{10}}{V_{10} V_1(t)} \\ \dfrac{P_2 x_6(t) - P_{2,stab}(t) V_{20}}{V_{20} V_2(t)} \end{bmatrix} \tag{4.9}$$

In case ideally precise measurements are available, it can be shown that the system is stable provided that the control vector **u***(t)* can be expressed in the form of (4.10).

$$\mathbf{u}(t) = -B^t \cdot P \cdot X(t) \tag{4.10}$$

where P is the solution of Lyapunov equation (4.11), in which P and Q are positive definite matrices [92].

$$PA + A^t P = -Q \tag{4.11}$$

In practice, the above-mentioned feedback loop is implemented by adding the set of stabilizing powers to the power references of the active loads. The stabilizing powers are given in

$$\begin{aligned} P_{sc,stab} &= (i_{10} + i_{20} - i_{s0})x_4(t) - u_1(t)V_n(t) \\ P_{1,stab} &= i_{10}x_5(t) - u_2(t)V_1(t) \\ P_{2,stab} &= i_{20}x_6(t) - u_3(t)V_2(t) \end{aligned} \tag{4.12}$$

These stabilizing powers are generated in the feedback control loop of the stabilization block. However, as they are completely dependent on the system variables, errors in their measurements may have negative effect on the stabilization performance. To investigate this issue, the measurement errors are modeled by non-unity sensor gains and sensor offsets. Therefore, each measured variable is expressed in terms of its actual value by

$$\hat{g}_i = l_i g_i + l_{i0} \quad i = 1,2,...6 \tag{4.13}$$

where g_i is a voltage or a current variable, l_i is a non-unity gain resulted from the sensor gain error, l_{i0} is the sensor offset, and "^" indicates the measured value. Thus, the measured variables can be written in the matrix form of

$$\hat{\mathbf{g}} = \mathbf{L}\mathbf{g} + \mathbf{L_0} \tag{4.14}$$

In equation (4.14), $\mathbf{g}$ is a vector of current and voltage variables expressed by $\mathbf{g} = [i_s \quad i_1 \quad i_2 \quad V_n \quad V_1 \quad V_2]^T$, and the matrices $\mathbf{L}$ and $\mathbf{L_0}$ are defined as follows.

$$\begin{aligned} \mathbf{L} &= diag(l_1, l_2, ...l_6) \\ \mathbf{L_0} &= diag(l_{10}, l_{20}, ...l_{60}) \end{aligned} \tag{4.15}$$

Deriving (4.12) in terms of the measured variables and replacing it in (4.9), we will obtain

$$\begin{cases} u_1 = l_4\hat{u}_1 + \dfrac{1}{V_n}(l_{40}\hat{u}_1 - \sigma_1 x_4) \\ u_2 = l_5\hat{u}_2 + \dfrac{1}{V_1}(l_{50}\hat{u}_2 - \sigma_2 x_5) \\ u_3 = l_6\hat{u}_3 + \dfrac{1}{V_2}(l_{60}\hat{u}_3 - \sigma_3 x_6) \end{cases} \tag{4.16}$$

where the coefficients σ_1, σ_2, and σ_3 are calculated as follows.

$$\begin{aligned}
\sigma_1 &= (l_1 l_4 - 1) i_{s0} - (l_2 l_4 - 1) i_{10} \\
&-(l_3 l_4 - 1) i_{20} - l_{10} l_4 + l_{20} l_4 + l_{30} l_4. \\
\sigma_2 &= (l_2 l_5 - 1) i_{10} + l_{20} l_5. \\
\sigma_3 &= (l_3 l_6 - 1) i_{20} + l_{30} l_6.
\end{aligned} \tag{4.17}$$

We rewrite (4.16) in a matrix form by

$$\mathbf{u} = \mathbf{\Gamma}\hat{\mathbf{u}} + \mathbf{F}(\mathbf{x}, \hat{\mathbf{u}}) \tag{4.18}$$

where $\mathbf{\Gamma} = diag(l_4, l_5, l_6)$, and

$\mathbf{F}(\mathbf{x}, \hat{\mathbf{u}}) = \left[(l_{40}\hat{u}_1 - \sigma_1 x_4)/V_n \quad (l_{50}\hat{u}_2 - \sigma_2 x_5)/V_1 \quad (l_{60}\hat{u}_3 - \sigma_3 x_6)/V_2 \right]^T$.

Replacing (4.18) in the original state space equation, we will have

$$\dot{\mathbf{x}} = \mathbf{A}\mathbf{x} + \mathbf{B}\mathbf{\Gamma}\hat{\mathbf{u}} + \mathbf{B}\mathbf{F}(\mathbf{x}, \hat{\mathbf{u}}) \tag{4.19}$$

The ultimate objective of the control design is to come up with an appropriate state feedback matrix **K** which results in an effective control vector by $\hat{\mathbf{u}} = -\mathbf{K}\hat{\mathbf{x}} = -\mathbf{K}\mathbf{L}\mathbf{x}$. Therefore, we can simplify (4.19) by

$$\dot{\mathbf{x}} = \hat{\mathbf{A}}_{\mathbf{C}}\mathbf{x} + \tilde{\mathbf{f}}(\mathbf{x}) \tag{4.20}$$

where $\hat{\mathbf{A}}_{\mathbf{C}} = \mathbf{A} - \mathbf{B}\mathbf{\Gamma}\mathbf{K}\mathbf{L}$, and $\tilde{\mathbf{f}}(\mathbf{x}) = \mathbf{B} \cdot \mathbf{F}(\mathbf{x}, -\mathbf{K}\mathbf{L}\mathbf{x})$. The latter is expressed in more detail by (4.21), wherein $\gamma_{mn} = l_{(m+3)0} k_{mn} - \sigma_m$.

$$\tilde{\mathbf{f}}(x) = \begin{bmatrix} 0 \\ 0 \\ 0 \\ \dfrac{-1}{C_n V_n} \displaystyle\sum_{i=1}^{6} \gamma_{1i} x_i \\ \dfrac{1}{C_1 V_1} \displaystyle\sum_{i=1}^{6} \gamma_{2i} x_i \\ \dfrac{1}{C_2 V_2} \displaystyle\sum_{i=1}^{6} \gamma_{3i} x_i \end{bmatrix} = \begin{bmatrix} 0 \\ 0 \\ 0 \\ \dfrac{-f_1(x_4)}{C_n} \displaystyle\sum_{i=1}^{6} \gamma_{1i} x_i \\ \dfrac{f_2(x_5)}{C_1} \displaystyle\sum_{i=1}^{6} \gamma_{2i} x_i \\ \dfrac{f_3(x_6)}{C_2} \displaystyle\sum_{i=1}^{6} \gamma_{3i} x_i \end{bmatrix} \tag{4.21}$$

The resulted state space model (4.20) has three nonlinear functions (f_1, f_2, and f_3). It is seen that each of these nonlinearities is a one-to-one nonlinear function. To deal with the system stability issue, Takagi-Sugeno (TS) multi-modeling approach is used, which is particularly effective for one-to-one nonlinear functions [118, 119]. TS multi-models

are used to estimate the domain of attraction. Using fuzzy "*if-then*" rules, this approach derives a set of linear local models whose convex combination can represent the nonlinear system. The method is explained briefly in the following.

4.2.3 Takagi-Sugeno multi-modeling

Assuming "*q*" nonlinearities $f_1(x)$ to $f_q(x)$ in the system, premise variables z_j $(j=1, 2,...q)$ are decision variables which depend on the state vector. Fuzzy membership functions, noted by F_j^i $(i=1, 2,...r)$, set up "*r*" fuzzy rules in the form of

Rule R^i: *If* $\{ z_1(t)$ is $F_1^i, \dots$, and $z_q(t)$ is $F_q^i \}$, *Then* $\{ \dot{\mathbf{x}}(t) = \mathbf{A_i}\mathbf{x}(t) + \mathbf{B_i}\mathbf{u}(t) \}$. (4.22)

where $\mathbf{A_i}$ and $\mathbf{B_i}$ are constant matrices that are deduced from the original system state matrices **A** and **B**. Each fuzzy rule R^i is attributed to a weight factor w_i which depends on the membership degree of the premise variables z_j to the fuzzy subsets F_j^i.

$$w_i(z(t)) = \prod_{j=1}^{q} F_j^i(z_j(t)), \qquad i = 1, 2, ...r \tag{4.23}$$

To comply with the property of convex combination, the weight factors should be normalized by

$$h_i(z(t)) = \frac{w_i(z(t))}{\sum_{i=1}^{r} w_i(z(t))} \tag{4.24}$$

Therefore, the fuzzy inferred model is expressed by

$$\dot{\mathbf{x}}(t) = \sum_{i=1}^{r} \{ h_i(z(t)) \cdot [\mathbf{A_i} \cdot \mathbf{x}(t) + \mathbf{B_i} \cdot \mathbf{u}(t)] \} \tag{4.25}$$

With sufficient number of the local linear models, the obtained TS model can be proved equivalent to the original nonlinear model. Each nonlinearity $f_j(x)$ may at least accept two values $f_j(x_{\max}^j)$ and $f_j(x_{\max}^j)$ corresponding to $x_{\max}^j$ and $x_{\min}^j$ respectively. Therefore, the TS model has at least $r = 2^q$ local linear models. Assuming the system inputs are constant, the system becomes a TS autonomous model which is asymptotically stable if the following LMIs hold

$$\begin{cases} \mathbf{M} = \mathbf{M}^{\mathbf{T}} > 0 \\ \mathbf{A}_{\mathbf{i}}^{\mathbf{T}} \cdot \mathbf{M} + \mathbf{M} \cdot \mathbf{A}_{\mathbf{i}} < 0, \quad i = 1, 2, ...r \end{cases} \tag{4.26}$$

A valid matrix $\mathbf{M}$ exists if each matrix $\mathbf{A_i}$ is Hurwitz as well as their summation $\mathbf{A} = \sum_{i=1}^{r} \mathbf{A_i}$. If LMIs of (4.26) are feasible, the system is asymptotically stable, and a valid Lyapunov function candidate can be obtained by

$$V(x) = \mathbf{x}^{\mathbf{T}} \cdot \mathbf{M} \cdot \mathbf{x} \tag{4.27}$$

It is noteworthy that the Lyapunov function candidate can be found with no knowledge of either F_j^i or w_i. To determine a valid function, the local state matrices $\mathbf{A_i}$ are required. These matrices can be calculated by fixing the q nonlinearities to their both end limits i.e. $f_j(x_{\max}^j)$ and $f_j(x_{\max}^j)$. Evaluating these limits, we can estimate the domain of attraction corresponding to the system operating point. The domain of attraction is the operating region in which the system is stable. A sample domain of attraction is shown in Fig. 4-5, which means the system can recover its stability provided that the variables deviations don't exceed the limits of the illustrated surface.

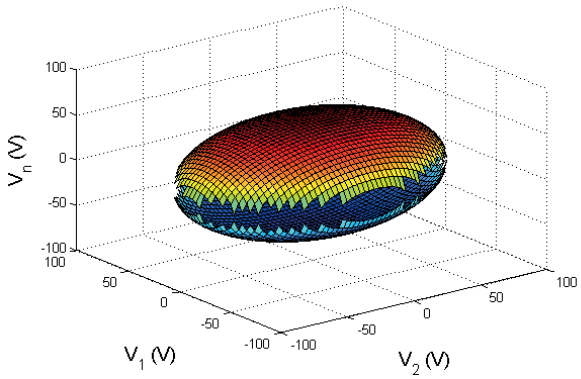

Fig. 4-5. A sample domain of attraction in terms of deviation from the operating point.

Before using Takagi-Sugeno method in stabilization design, the parameter uncertainties are also taken into account.

4.2.4 Parameters uncertainties

The system parameters may vary due to ambient conditions or degradation. As this can deteriorate the stability margins, the effect of parameter variations on the stability should be considered. This effect on stability could be studied by sensitivity analysis of system eigenvalues. The sensitivity of the eigenvalue λ_i to the element a_{kj} of the state matrix is equal to the product of the left eigenvector element ψ_{ik} and the right eigenvector element ϕ_{kj} [127].

$$\frac{\partial \lambda_i}{\partial a_{kj}} = \psi_{ik}\phi_{ji} \tag{4.28}$$

The overall sensitivity of the eigenvalues to the elements of the state matrix can be calculated by

$$S = \sum_i \sum_k \sum_j (\psi_{ik}\phi_{ji}) \tag{4.29}$$

where k and j specify the state matrix elements that are dependent on the system parameters. By minimizing the overall sensitivity, we can achieve a maximal robustness to parameter uncertainties.

According to the foregoing analyzes of measurement errors and parameters uncertainties, we develop a robust stabilization control design in this section. The control design can be developed by an appropriate placement of the system closed-loop poles. Fig. 4-6 shows an algorithm that finds a robust state feedback matrix K by considering a compromise between the largest domain of attraction and the least sensitivity. In the first step, a set of closed-loop poles is selected within a desirable region introduced in Fig. 4-7. This region is determined to provide proper control performance in terms of response time and damping factor. The initially selected closed-loop poles are optimized throughout consecutive iterations within the algorithm.

The optimization process is based on two measures each of which is evaluated on an algorithm branch. On the left algorithm branch, the domain of attraction is calculated by step-wise modification of x_{min} and x_{max}. At each step change of x_{min} and x_{max}, LMI problem of (4.26) is evaluated. The difference between x_{min} and x_{max} increases over iterations, meaning that the domain of attraction expands step-by-step. As soon as the solution becomes unfeasible in an iteration, the latest values of x_{min} and x_{max} yield an estimate of the domain of attraction. These values determine the acceptable variation ranges of V_n, V_1, and V_2 in order for the system to remain stable. On the right algorithm

branch, the sensitivity to the system parameters is evaluated. A compromise between the broadest domain of attraction and the least sensitivity is realized by division of the left branch output by the right branch output. The objective of the algorithm is to maximize this division.

In order to solve the above optimization problem, Genetic Algorithm is used. The outcome of the algorithm is the state feedback matrix K, which provides robust stabilization of the dc network under study. In the following sections, the performance of the proposed design will be evaluated through simulations and experiments.

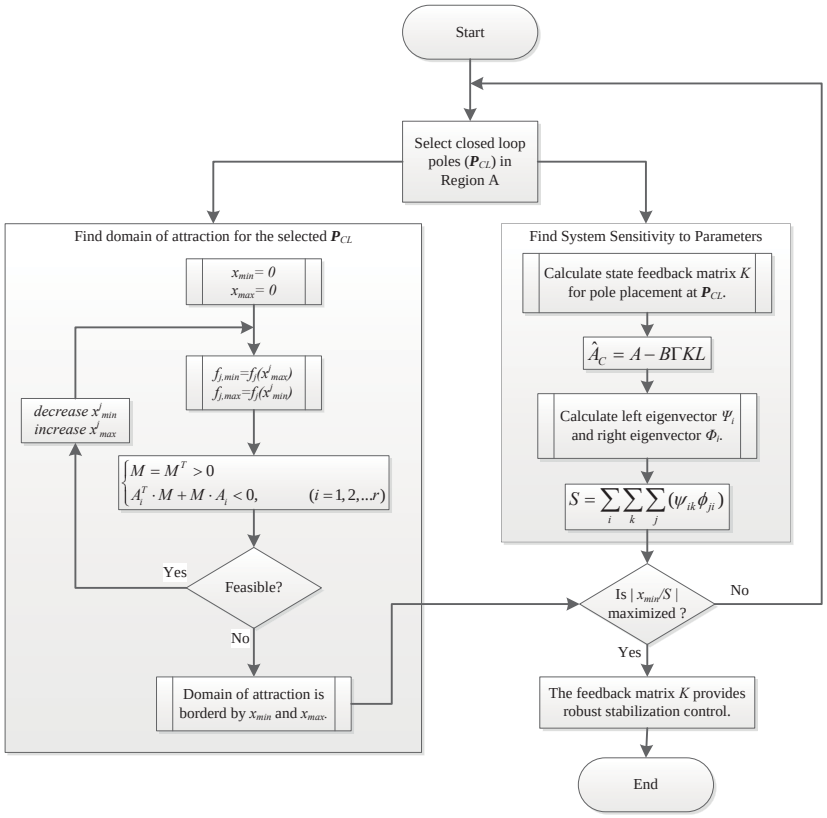

Fig. 4-6. Algorithm of robust control design.

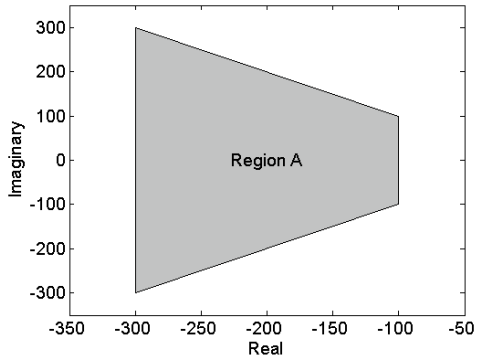

Fig. 4-7. Considered limits for the system closed-loop poles.

4.3 Simulation results

To evaluate the proposed robust stabilization method, the system of Fig. 4-3 is simulated in MATLAB/Simulink. The parameters of the simulated system are found in Table 4.1. The system has been tested in two conditions. The first condition is when all measurements are made precisely without any error. In the second condition, 50% error is considered in measurements of the sensors. Fig. 4-8, Fig. 4-10, and Fig. 4-12 compare the robust global stabilization (RGS) with active global stabilization method (AGS) [117] under the first condition. The solid curves show responses of the system voltages to a step change on the inverter power under robust control method, while no measurement error exists. The dashed curves show the voltage responses of the AGS control method. Although both methods stabilize the system under this condition, the performance of the robust method is preferable in terms of response time and damping.

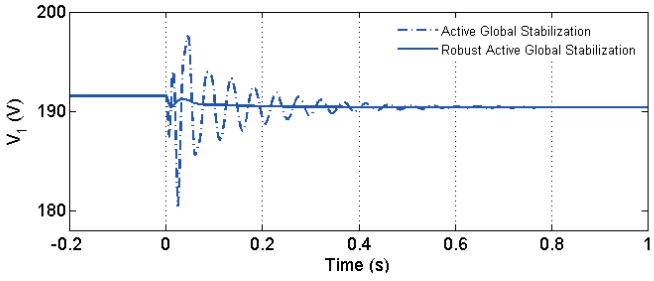

Fig. 4-8. Simulated response of V_n to a step change of P_1 from 1000W to 1500W (precise sensors)

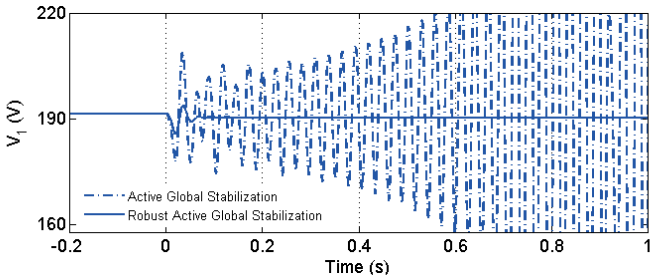

Fig. 4-9. Simulated response of V_n to step change of P_1 from 1000 to 1500W (erroneous sensors)

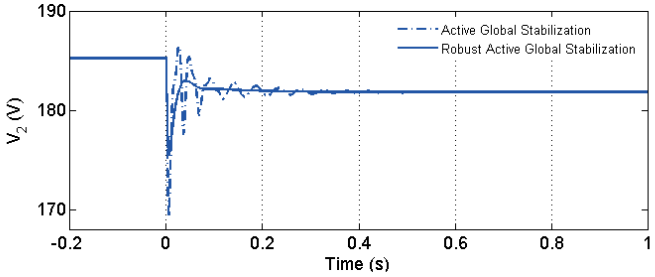

Fig. 4-10. Simulated response of V_1 to a step change of P_1 from 1000W to 1500W (precise sensors)

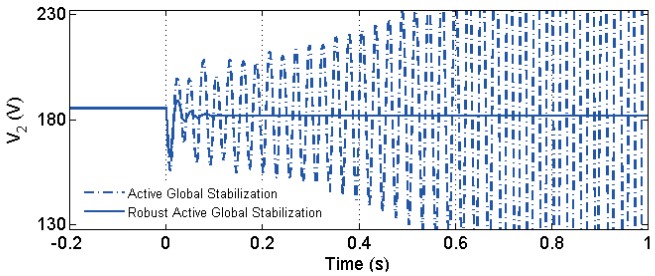

Fig. 4-11. Simulated response of V_1 to step change of P_1 from 1000 to 1500W (erroneous sensors)

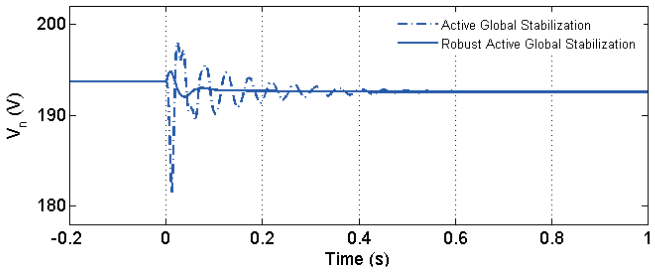

Fig. 4-12. Simulated response of V_2 to step change of P_1 from 1000W to 1500W (precise sensors)

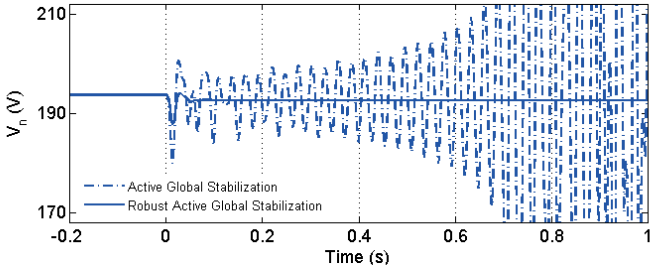

Fig. 4-13. Simulated response of V_2 to step change of P_1 from 1000 to 1500W (erroneous sensors)

Fig. 4-9, Fig. 4-11, and Fig. 4-13 make comparisons between the two methods when errors exist in measurements. The proposed robust method stabilizes the dc network under rather high measurement errors. However, AGS method is not able to maintain the stability under the erroneous measurement conditions. The proposed method will be further investigated in the next section through experimental results.

4.4 Experimental results

An experimental setup of an isolated dc network with configuration of Fig. 4-1 is developed to evaluate the theoretical analysis and simulations of the proposed methodology. To implement the stabilization control system, dSpace© platform is used. Taking the measured voltages and currents from the data acquisition module, the processing unit calculates a set of stabilizing powers. These stabilizing powers are superposed on the power references of the converters, based on which the gate signals of the IGBTs are generated. A picture of the testbed is shown in Fig. 4-14.

In this section, the proposed method is experimentally verified by testing the system under faulty and erroneous measurement conditions as well as under normal measurement conditions. Fig. 4-15 shows the performance of the method by experimental results under precise measurement condition. The quadratic component of the motor current is controlled at $i_q = 9A$ and the buck converter draws a power of $P_2 = 500W$. The dc network becomes unstable as soon as the stabilization control loop is opened. Reclosing the control loop, we observe that the control system restores the stability of the dc network.

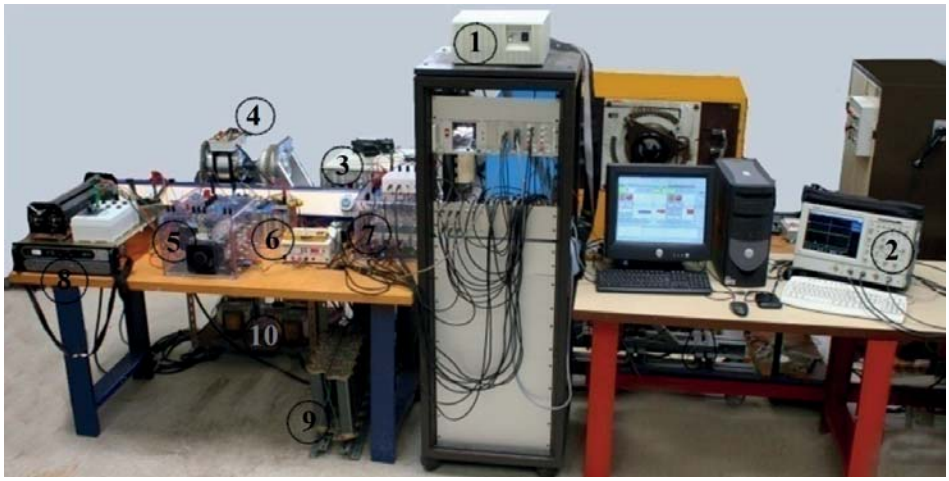

Fig. 4-14. A picture of the experimental setup at GREEN, university of Lorraine.

(1) dSpace unit	(2) 20-MHz Oscilloscope	(3) Inverter	(4) PMSM
(5) Boost converter	(6) Supercapacitor module	(7) Buck converter	(8) DC source
(9) Resistive load	(10) Inductors		

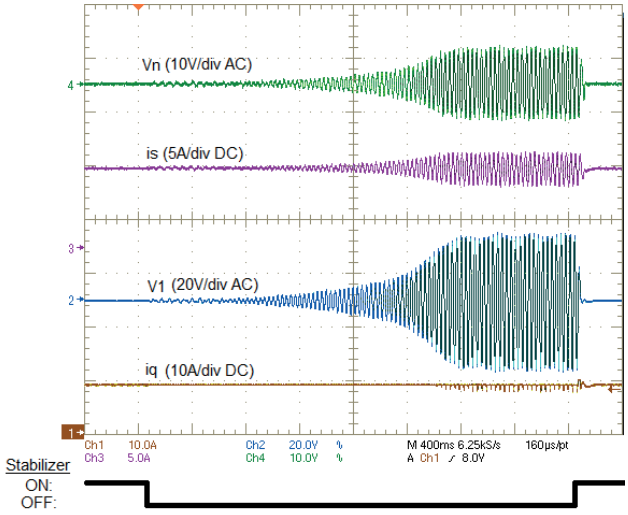

Fig. 4-15. System stability status under normal measurement condition, $i_q = 9A$ and $P_2 = 500W$ (Experimental)

The performance of the proposed stabilization method is compared to AGS [117] when no measurement error exists. The experimental results of the comparison are presented in Fig. 4-16. A step-up of i_q from $7A$ to $9A$ drives the dc network to instability when AGS control method is used. However, the proposed robust method maintains the stability under the same conditions. The load power of the buck converter for this test is

$P_2 = 500W$. This test demonstrates that RGS extends the system stability margins further compared to AGS, as a prime design measure in RGS is to expand the domain of attraction. Fig. 4-17, Fig. 4-18, and Fig. 4-19 show the generated stabilizing powers by RGS control system. These powers are injected to the dc network by superposing them on the reference powers of the converters. The power impulses are generated as soon as the torque step on the PMSM occurs at $t = 0s$.

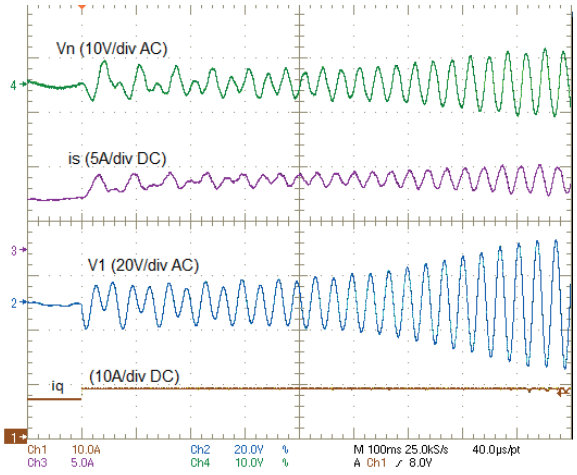

(a)

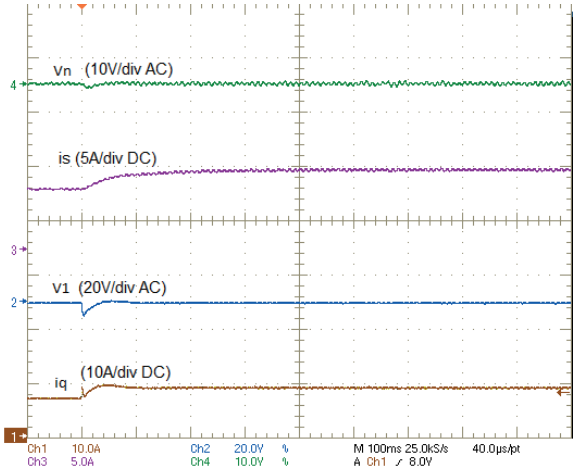

(b)

Fig. 4-16. Comparison of the two methods with precise measurements (Experimental)
a) AGS, b) RGS.

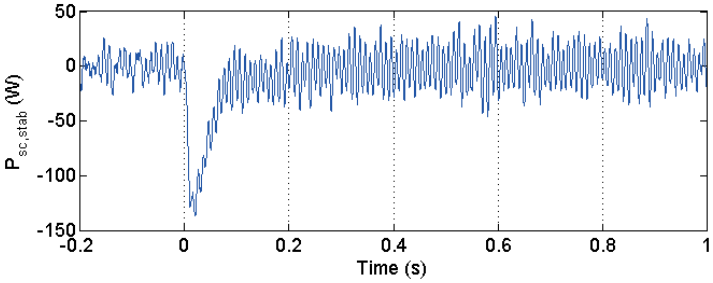

Fig. 4-17. Injected stabilizing power by the bidirectional converter in RGS method (Experimental).

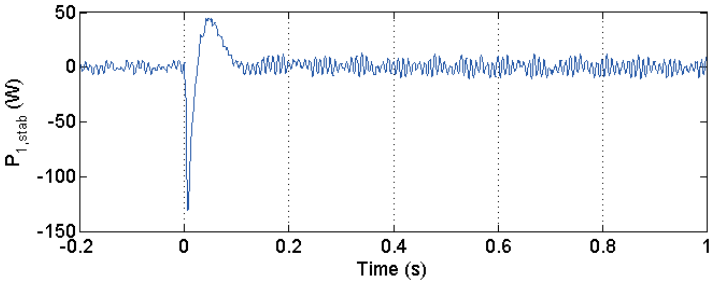

Fig. 4-18. Injected stabilizing power by the inverter in RGS method (Experimental).

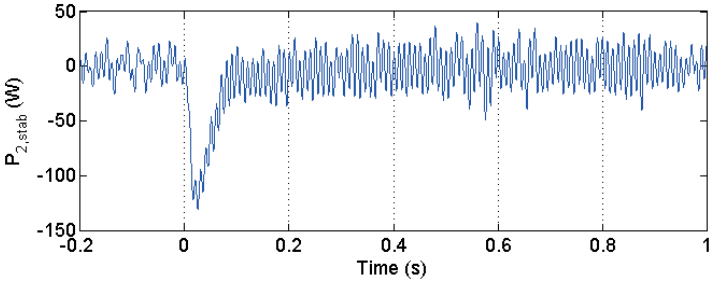

Fig. 4-19. Injected stabilizing power by the buck converter in RGS method (Experimental).

Fig. 4-20 compares the two methods when the measurements are made with 50% error. The loading conditions are chosen in such a way that both methods can stabilize the network, given precise measurements are available. Therefore, the power of the buck converter is adjusted on $P_2 = 300W$, and i_q is only stepped up from $7A$ to $8A$.

AGS method, as seen in Fig. 4-20, is not able to generate required stabilizing efforts under erroneous measurement conditions. However, RGS method maintains the network stability under the same conditions. This test validates the robustness of the proposed method to measurement uncertainties.

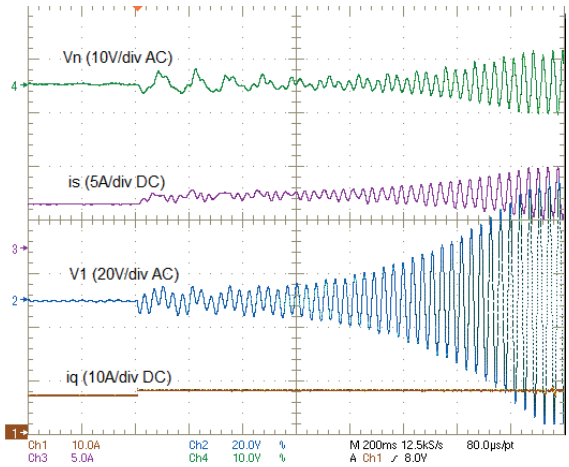

(a)

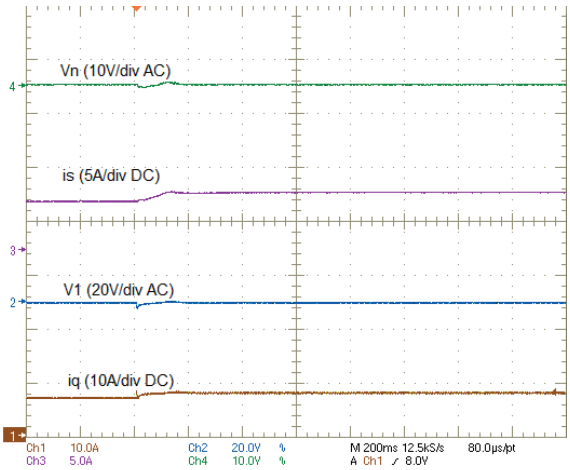

(b)

Fig. 4-20. Comparison of the two methods with erroneous measurements (Experimental) a) AGS, b) RGS.

Fig. 4-21, Fig. 4-22, and Fig. 4-23 show the injected stabilizing powers by RGS control system in the erroneous measurement mode. These powers disturb the normal operation of the converters to save the network stability. In case the network supplies a critical load whose power should not be disturbed, its associated stabilizing power reference could be set to zero. Consequently, the stabilizing efforts of other controllable loads would increase. This situation may also incidentally happen in case of failure e.g. when a sensor fails or a failure occurs at transmission of a stabilizing signal. In the following, the tolerance of the method to faults will be addressed.

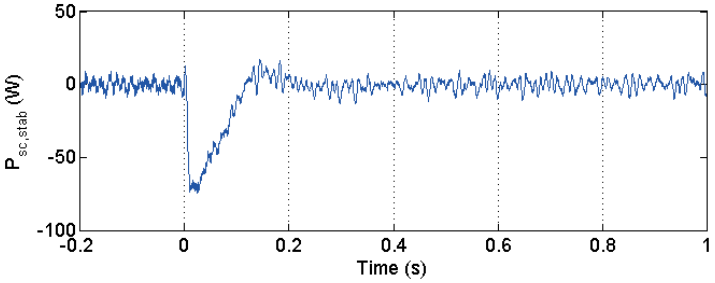

Fig. 4-21. Injected stabilizing power by the bidirectional converter in RGS method (Experimental)

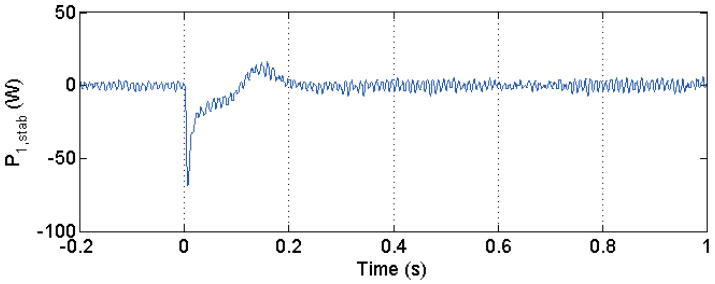

Fig. 4-22. Injected stabilizing power by the inverter in RGS method (Experimental)

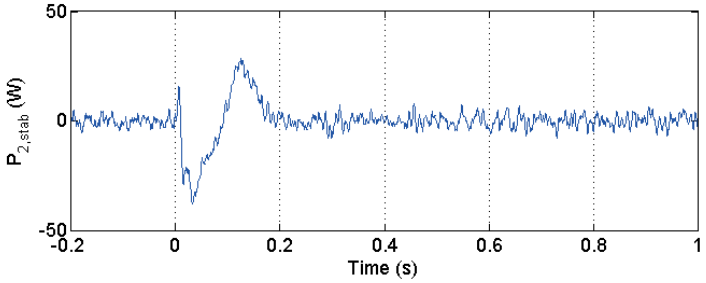

Fig. 4-23. Injected stabilizing power by the buck converter in RGS method (Experimental)

4.4.1 Fault tolerance evaluation

Reliability is a major concern in marine and aerospace power systems. Single point of failures should be investigated and avoided in these systems. Having a centralized architecture, the proposed control system creates a potential single point failure which is a drawback. Nevertheless, this single point failure can be avoided by adding a redundancy for the central processor. Other potential faults in the proposed control system include failure in measurement due to sensor failure or signal transmission

failure.

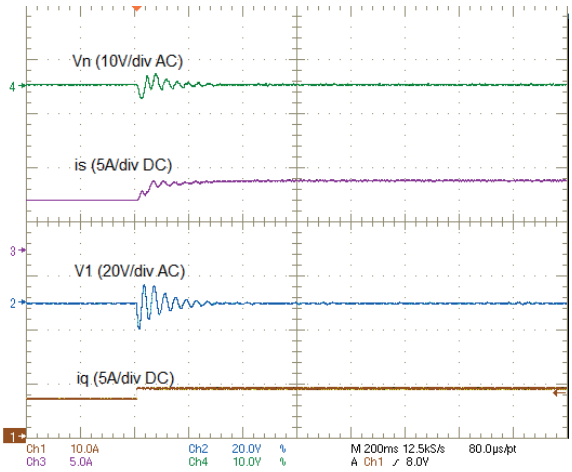

Fig. 4-24. Performance of the proposed stabilizer with failed sensor of V_1 when i_q steps from *7 to 9A* and P_2 = *300W* (Experimental)

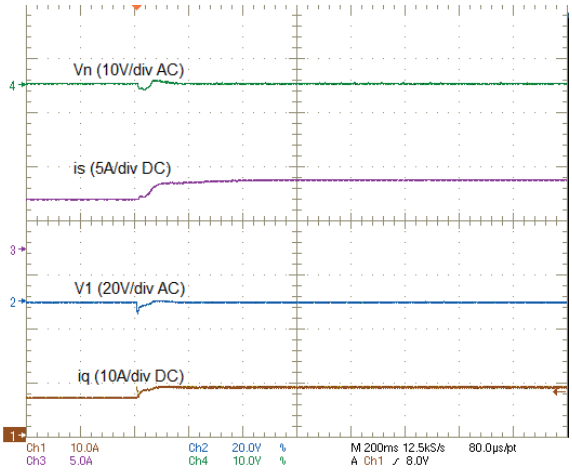

Fig. 4-25. Performance of the proposed stabilizer with failed sensor of V_n when i_q steps from *7 to 9A* and P_2 = *300W* (Experimental)

The control system is tested when a fault occurs on a sensor or two. Fig. 4-24 shows the test results when sensor V_1 fails. The buck converter power is P_2 = *300W*, and i_q steps from *7* to *9A*. Fig. 4-25 shows similar results under failure of sensor V_n. It is seen that the proposed method can maintain the network stability when a sensor fails. In Fig. 4-26 and Fig. 4-27 the control system stabilizes the dc network when two of the voltage sensors have failed. The stabilizing powers generated with failed sensors V_n and

V_1 are shown in Fig. 4-28. Under this condition, the stabilizing powers provided by the bidirectional converter and the inverter are zero. Therefore, the buck converter should take care of the system stability by itself. The healthy subsystem stabilizes the network as long as it is able to make the required stabilizing effort for the whole system.

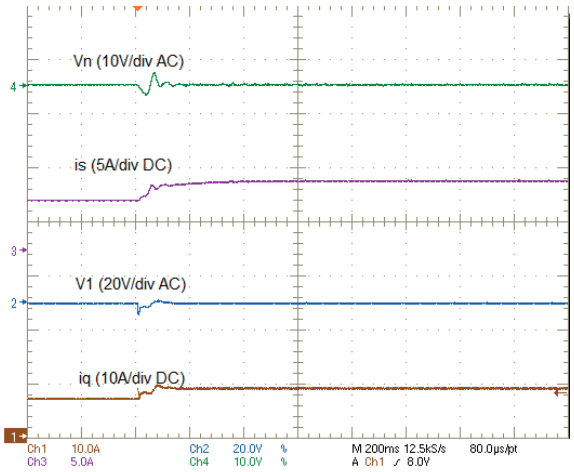

Fig. 4-26. Performance of the proposed stabilizer with failed sensors of V_n and V_2 at i_q step from *7 to 9A* and $P_2 = 300W$ (Experimental)

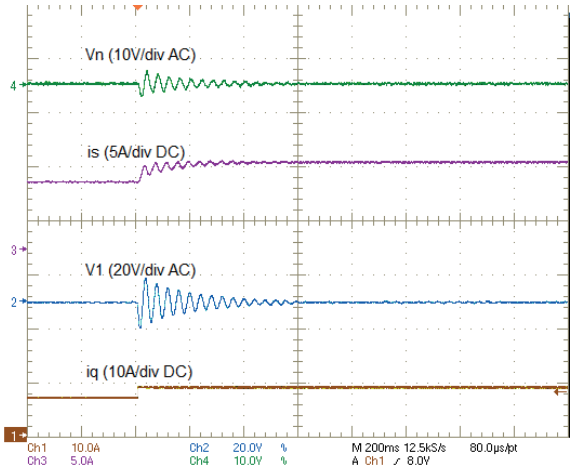

Fig. 4-27. Performance of the proposed stabilizer with failed sensors of V_n and V_1 at i_q step from *7 to 9A* and $P_2 = 300W$ (Experimental)

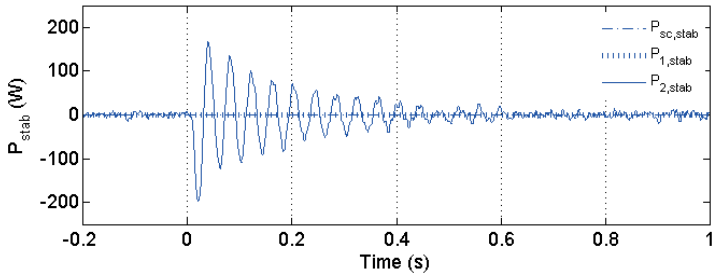

Fig. 4-28. Injected stabilizing powers by the converters with failed sensors of V_n and V_1 (Experimental)

4.5 Summary

A robust large-signal stabilization technique was presented to ensure global stability of a power electronic based dc network. Assuming each converter as a constant power load, we derived a nonlinear state space model for the overall system. Taking into account the measurement and parameter uncertainties in the nonlinear model, we devised a robust stabilization method by using Takagi-Sugeno multi-modeling and robust pole placement. The proposed method enhances the stability margin of isolated dc networks that supply controllable loads by applying stabilizing feedbacks to the loads. Such a stabilization method allows the benefit of having small dc-link and LC capacitors, which is particularly desirable in transportation systems. The performance of the proposed technique was validated through simulation and experimental results, and its advantages over the preceding methods were demonstrated. The robust characteristic of the control system provides effective stabilization performance under faulty and degraded conditions which include erroneous measurements, sensor failure, and parameters degradation.

5
Conclusion

Shipboard dc hybrid power systems are presently being considered for commercial marine vessels to provide low-emission and fuel-efficient operation along with providing space and weight savings. In spite of the benefits offered by the onboard dc network, the resulted interconnected system requires effective analysis tools to investigate the advantages and overcome the challenges.

Essential tools in design, analysis, optimization, and control of the dc hybrid power systems are modeling and simulation tools. Modeling of an all-electric ship with onboard dc network was presented in this thesis. In the system modeling, the limiting factor in terms of computation time was the switching behavior of the power electronic converters, which requires extremely small time steps. Averaging methods were used to model the power electronic converters by neglecting high frequency switching behavior to reduce the computation burden and time. Nonlinear models were derived in order to support system-level studies which require large signal analysis of the system. A simulation platform was developed using the derived models of different components. Providing significant savings in time and computational intensity, the presented simulation tool demonstrates effective performance in long-term and repetitive simulations.

A major motivation in the development of shipboard dc power systems is to provide opportunities for fuel saving. In order to evaluate its potential fuel saving, a shipboard dc hybrid power system was analyzed in terms of efficiency and fuel consumption. Adapting the developed models of the simulator by including the power loss

components of each element, the system efficiency analysis was performed. It was shown that maximum fuel saving conditions for such a system required the generator sets to operate at optimal loading conditions in terms of both average power and power ripple. To find these optimal loading conditions, a numerical optimization algorithm was proposed. The optimization algorithm also determined whether the generator sets operated at continuous mode or periodical charge/discharge mode. To estimate the optimized fuel saving in practice, an on-line optimization control was applied in simulation of an Offshore Support Vessel (OSV) over seven operating modes. The online optimization control provided an average fuel saving of over 15 % compared to the conventional ac systems. The shipboard dc system with optimized control of energy storage provided a fuel saving of more than 7% compared to the dc system without energy storage. The study results on fuel consumption demonstrated significant fuel-saving potentials in maritime sector, particularly in the category of marine vessels that experience frequent load variations or long-time operation under non-rated conditions.

The shipboard dc hybrid power systems can be considered as isolated multi-converter dc networks. The stability of these power electronic-based systems is an essential design and control issue due to destabilizing negative impedance introduced by power electronic converters. Large signal stability control of shipboard dc grids was investigated in this thesis. Assuming each converter as a constant power load, we developed a nonlinear state space model for the overall system. Taking into account the measurement and parameter uncertainties in the nonlinear model, we proposed a robust stabilization method by using Takagi-Sugeno multi-modeling and robust pole placement. The proposed method enhances the stability margin of isolated dc networks that supply controllable loads. This was carried out by applying stabilizing feedbacks to the loads. Such a stabilization method allows the benefit of having small dc-link and LC capacitors, which is particularly desirable in transportation systems. The performance of the proposed technique was validated against simulation and experimental results, and its advantages over the preceding methods were demonstrated. The robust characteristic of the control system provides effective stabilization performance under degraded conditions. These conditions include erroneous measurements, sensor failure, and parameters degradation.

5.1 Prospects for future work

Shipboard dc grids are at their early stages of research and development. Various aspects of these systems need to be studied. These studies can include a wide range of activities from the design optimizations to system analysis to different control methodologies for power management, system protection, fault tolerance, stability, etc. This thesis is one of the early works reported on shipboard dc grids targeting commercial applications, which mainly deals with their time-domain analysis, efficiency analysis, and stability control. These research tasks could be pursued further as follows.

Fuel saving potentials for an offshore support vessel was evaluated when energy storage was incorporated in the ship dc network. In a future work, this evaluation could be extended to other applications while a variety of power sources is investigated. Other vessel types to be studied include fishing vessels and tugboats. Gas turbines and fuel cells could be considered as alternative main and auxiliary power sources respectively.

This dissertation also introduced a centralized robust stabilizer for the dc networks with tightly controlled loads. The advantage of this method lies in the robust characteristic of the controller that provides improved stability margins at the presence of measurement errors and parameters uncertainties. The centralized architecture, however, requires transmission of all measured state variables throughout the network. This could lead to technical requirements on the remote sensors, data transmission lines, and data processors in terms of timing, redundancy, etc. In addition, the centralized structure creates a potential single point failure which necessitates a redundant central processor. These could be investigated in a prospective research to provide alternative solutions for the prescribed challenges through:

- Introduction of a state observer to estimate those variables that are difficult to transmit timely.
- Decentralized stabilization techniques.

6
Appendices

A

Average Modeling of the DC/DC Converters

An essential step to study, design and analyze modern power systems that include various power electronic modules is to model and simulate the system. Today, available standard power system simulators are based on detail switching models of the power electronic devices. Detail switching models need very small time steps during simulation which causes excessive simulation run time. Therefore, this kind of modeling is too slow especially when a large system is to be analyzed for longer times. A solution to this problem is to apply Average Value Modeling (AVM) when studying the exact switching behavior is not necessary. AVM approximates a variable by averaging over one switching period. It makes the simulation to run orders of magnitude faster. In order to carry out small signal analysis usually linearized Average Value Models are utilized. It represents the module by a block diagram composed of a few transfer functions. Since classical control theory is applicable to the transfer functions, this modeling approach facilitates the controller design. However, for system level analysis in which large signal variations are studied, linearized models are not appropriate. Nonlinear average models must be developed to use in system level analysis. This chapter presents different average models for dc-dc converters studied in the thesis.

A.1 Boost converter/mode:

Figure A-1 shows the schematic diagram of the isolated boost converter under study. The presented analysis can be used for the boost mode of the studied bidirectional converter as well. The circuit differential equations are expressed by

$$\begin{cases} L\dfrac{di_L(t)}{dt} = v_{in}(t) - \dfrac{1}{n}\big(1-u(t)\big)v_C(t), \\ C\dfrac{dv_C(t)}{dt} = \dfrac{1}{n}\big(1-u(t)\big)i_L(t) - \dfrac{v_C(t)}{R}, \end{cases} \tag{A.1}$$

where $u(t) = \begin{cases} 1, & 0 < t < dT \\ 0, & dT < t < T \end{cases}$

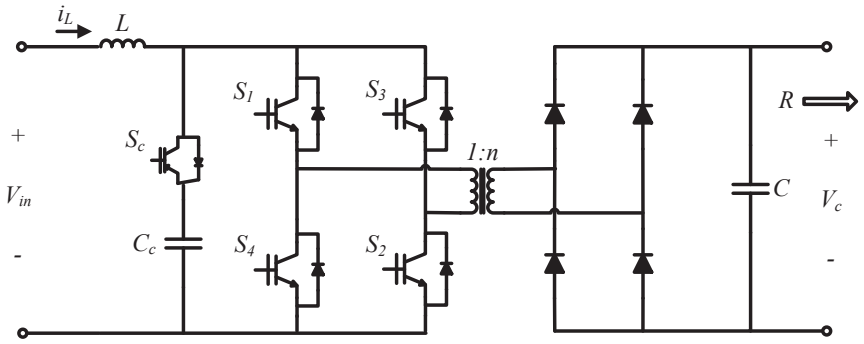

Figure A-1. The topological circuit of the boost converter under study

Figure A-2 shows the PWM gating signals in order to have the switching function, *u(t)*, as expressed in (A.1). *D* and T_S are duty cycle and switching period, respectively. During the overlapping period of both switch pairs which lasts for $D.T_S$, the energy is stored into the inductor core. In the second part of the switching period, the energy transfers to the high voltage side through the transformer. Due to the transformer leakage inductance, voltage transients might occur. The active clamp circuit can limit the voltage across the switches, and improve the energy efficiency of the converter.

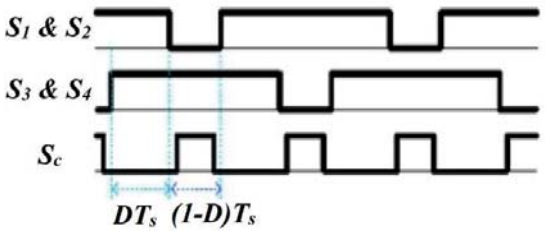

Figure A-2.Timing of the PWM gating signals for the full bridge boost converter [71]

A.1.1 Small signal average value model

The average model is useful to figure out the dynamic behavior of the converter in addition to its steady state characteristics. This model is obtained by averaging over the

switching period, which is defined by

$$\langle x(t)\rangle = \frac{1}{T}\int_{t-T}^{t} x(\tau)d\tau \tag{A.2}$$

Applying (A.2) to the circuit differential equations of (A.1), we will have

$$\begin{cases} L\dfrac{di_L(t)}{dt} = d(t)v_{in}(t) + d'(t)v_{in}(t) - \dfrac{1}{n}v_C(t) \\ C\dfrac{dv_C(t)}{dt} = d(t) - \dfrac{v_C(t)}{R} + d'(t)\dfrac{1}{n}i_L(t) - \dfrac{v_C(t)}{R} \end{cases} \tag{A.3}$$

Now the variables can be divided into steady state dc terms and small signal ac variation terms as expressed below.

$$\begin{cases} i_L(t) = I_L + \hat{i}_L; \\ v_{in}(t) = V_{in} + \hat{v}_{in};\ \ v_C(t) = V_C + \hat{v}_C; \\ d(t) = D + \hat{d};\ \ d'(t) = D' - \hat{d}; \end{cases} \tag{A.4}$$

where *D'* equals to *(1-D)* and the notation ^ indicates the small signal ac value. Replacing (A.4) into (A.3), we obtain

$$\begin{cases} L\dfrac{d\hat{i}_L}{dt} = (D+\hat{d})(V_{in}+\hat{v}_{in}) + (D'-\hat{d})(V_{in}+\hat{v}_{in} - \dfrac{1}{n}(V_C+\hat{v}_C)) \\ C\dfrac{d\hat{v}_C}{dt} = -(D+\hat{d})\dfrac{V_C+\hat{v}_C}{R} + (D'-\hat{d})(\dfrac{1}{n}(I_L+\hat{i}_L) - \dfrac{V_C+\hat{v}_C}{R}) \end{cases} \tag{A.5}$$

Separating the dc values from the small signal ac values, we will obtain

$$\begin{cases} L\dfrac{d\hat{i}_L}{dt} = \hat{v}_{in} - \dfrac{D'}{n}\hat{v}_C + \dfrac{V_C}{n}\hat{d} \\ C\dfrac{d\hat{v}_C}{dt} = \dfrac{D'}{n}\hat{i}_L - \dfrac{1}{R}\hat{v}_C + \dfrac{I_L}{n}\hat{d} \end{cases} \tag{A.6}$$

$$DV_{in} + D'V_{in} - \frac{D'}{n}V_C = 0; \qquad \boxed{V_C = \frac{n}{D'}V_{in}} \tag{A.7}$$

$$-D\frac{V_C}{R} + \frac{D'}{n}I_L - D'\frac{V_C}{R} = 0; \qquad \boxed{I_L = \frac{n}{D'R}V_C} \tag{A.8}$$

Figure A-3 shows the small signal ac equivalent circuit for the studied boost topology.

It is derived according to small signal equations of (A.6).

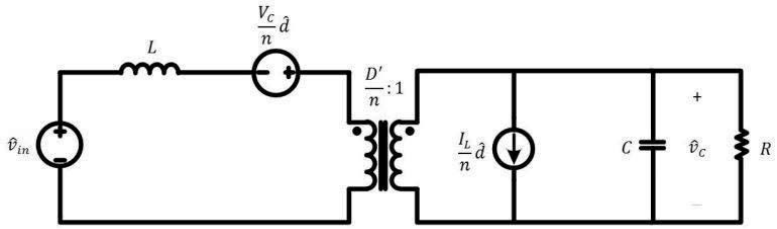

Figure A-3. Small signal ac equivalent circuit for the isolated boost converter

The converter can also be shown in block diagram which is suitable for classical control design. In this case, different transfer functions should be deduced from the small signal equivalent circuit. A comprehensive block diagram for the converter small signal model is shown in Figure A-4.

G_{vv}, G_{vd} and Z_{out} describe how variations or disturbances in the applied input voltage (v_{in}), control input duty cycle (d), and load current (i_{load}) affect the output voltage respectively. They can be calculated by (A.9)-(A.11). These transfer functions are important in design of the output voltage regulator.

$$G_{vv}(s) = \left.\frac{\hat{v}_{out}(s)}{\hat{v}_{in}(s)}\right|_{\substack{\hat{d}(s)=0 \\ i_{load}(s)=0}} \tag{A.9}$$

$$G_{vd}(s) = \left.\frac{\hat{v}_{out}(s)}{\hat{d}(s)}\right|_{\substack{\hat{v}_{in}(s)=0 \\ i_{load}(s)=0}} \tag{A.10}$$

$$Z_{out}(s) = \left.\frac{\hat{v}_{out}(s)}{\hat{i}_{load}(s)}\right|_{\substack{\hat{d}(s)=0 \\ \hat{v}_{in}(s)=0}} \tag{A.11}$$

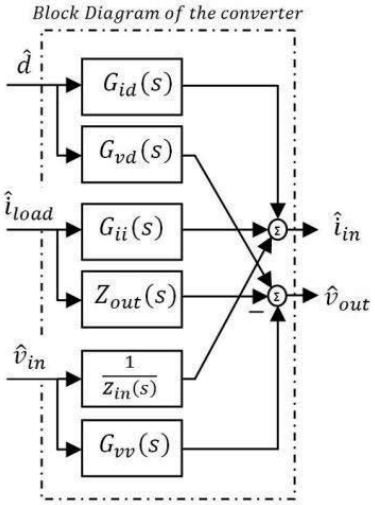

Figure A-4. Block diagram for the small signal model of the isolated boost converter based on transfer functions

Z_{in}, G_{id} and G_{ii} describe how variations or disturbances in the applied input voltage (v_{in}), control input duty cycle (d), and load current (i_{load}), respectively, affect the input current. They can be derived by (A.12)-(A.14).

$$Z_{in}(s) = \left.\frac{\hat{v}_{in}(s)}{\hat{i}_{in}(s)}\right|_{\substack{\hat{d}(s)=0 \\ \hat{i}_{load}(s)=0}} \tag{A.12}$$

$$G_{id}(s) = \left.\frac{\hat{i}_{in}(s)}{\hat{d}(s)}\right|_{\substack{\hat{v}_{in}(s)=0 \\ \hat{i}_{load}(s)=0}} \tag{A.13}$$

$$G_{ii}(s) = \left.\frac{\hat{i}_{in}(s)}{\hat{i}_{load}(s)}\right|_{\substack{\hat{d}(s)=0 \\ \hat{v}_{in}(s)=0}} \tag{A.14}$$

Calculating (A.9)-(A.14) by use of the equivalent circuit of Figure A-3, we obtain the different transfer functions shown in Figure A-4.

$$G_{vv}(s) = \frac{n}{D'} \frac{1}{1 + \frac{n^2 L}{D'^2 R} s + \frac{n^2 LC}{D'^2} s^2} \tag{A.15}$$

$$G_{vd}(s)=\frac{V_C}{D'}\frac{1-\frac{n^2L}{D'^2R}s}{1+\frac{n^2L}{D'^2R}s+\frac{n^2LC}{D'^2}s^2} \tag{A.16}$$

$$Z_{out}(s)=\frac{n^2L}{D'^2}\frac{s}{1+\frac{n^2L}{D'^2R}s+\frac{n^2LC}{D'^2}s^2} \tag{A.17}$$

$$Z_{in}(s)=\frac{D'^2R}{n^2}\frac{1+\frac{n^2L}{D'^2R}s+\frac{n^2LC}{D'^2}s^2}{RCs+1} \tag{A.18}$$

$$G_{id}(s)=\frac{nV_C}{D'^2R}\left(1+\frac{RCs+1}{1+\frac{n^2L}{D'^2R}s+\frac{n^2LC}{D'^2}s^2}\right) \tag{A.19}$$

$$G_{ii}(s)=\frac{n}{D'}\frac{1}{1+\frac{n^2L}{D'^2R}s+\frac{n^2LC}{D'^2}s^2} \tag{A.20}$$

A.1.2 Nonlinear state space average model

The small signal models are valid provided that the system variables don't exceed the linear range around the operating point. However, in system design and analysis, it is sometimes required to study the system reaction to large variations. Therefore, large signal nonlinear models are derived for such studies. The state space average model can be expressed in a nonlinear form to be appropriate for system level analysis. The state space equations can be derived by expanding (A.1) as expressed in (A.21).

$$\begin{cases}\begin{bmatrix}\frac{di_L(t)}{dt}\\ \frac{dv_C(t)}{dt}\end{bmatrix}=\begin{bmatrix}0 & -\frac{1}{nL}\\ \frac{1}{nC} & -\frac{1}{RC}\end{bmatrix}\begin{bmatrix}i_L(t)\\ v_C(t)\end{bmatrix}+\begin{bmatrix}\frac{1}{L}\\ 0\end{bmatrix}v_{in}(t) & for \quad 0<t<dT,\\ \begin{bmatrix}\frac{di_L(t)}{dt}\\ \frac{dv_C(t)}{dt}\end{bmatrix}=\begin{bmatrix}0 & 0\\ 0 & -\frac{1}{RC}\end{bmatrix}\begin{bmatrix}i_L(t)\\ v_C(t)\end{bmatrix}+\begin{bmatrix}\frac{1}{L}\\ 0\end{bmatrix}v_{in}(t) & for \quad dT<t<T,\end{cases} \tag{A.21}$$

We see that the circuit can be expressed by two sets of state space equations for two

states of switching. By averaging over the switching period these two sets of equations will be combined in a single set of state space equations as shown in (A.22).

$$\begin{bmatrix} \dfrac{di_L(t)}{dt} \\ \dfrac{dv_C(t)}{dt} \end{bmatrix} = (d(t)\mathbf{A_1} + (1-d(t))\mathbf{A_2}) \begin{bmatrix} i_L(t) \\ v_C(t) \end{bmatrix} + \mathbf{B}v_{in}(t) \tag{A.22}$$

where the matrices are as follows

$$\mathbf{A_1} \triangleq \begin{bmatrix} 0 & -\dfrac{1}{nL} \\ \dfrac{1}{nC} & -\dfrac{1}{RC} \end{bmatrix},\ \mathbf{A_2} \triangleq \begin{bmatrix} 0 & 0 \\ 0 & -\dfrac{1}{RC} \end{bmatrix},\ \mathbf{B} \triangleq \begin{bmatrix} \dfrac{1}{L} \\ 0 \end{bmatrix}$$

(A.22) represents the nonlinear state space average model of the studied boost topology. The linearized state space model can be obtained by replacing *d(t)* with the constant duty cycle *D* corresponding to the equilibrium point. In order to take into account the ripples for higher accuracy, we will derive the generalized state space average model in the following.

A.1.3 Generalized average modeling

Generalized averaging is based on the idea that each variable can be approximated by Fourier series which is represented by

$$x(t) = \sum_{k=-n}^{n} \langle x \rangle_k \, e^{jk\omega t} \tag{A.23}$$

where $\langle x \rangle_k$ is the Fourier coefficient for k^{th} order harmonic and is calculated by (A.24). In order to obtain the generalized average model, we need to calculate the coefficients of the Fourier series for the circuit state variables. To get better precision, one can take into consideration higher order harmonics i.e. higher "*n*". It is noteworthy that the average value modeling is a special form of the generalized averaging method in which only the zero harmonic (*n=0*) is considered.

$$\langle x \rangle_k (t) = \frac{1}{T} \int_{t-T}^{t} x(\tau) e^{-jk\omega\tau} d\tau \tag{A.24}$$

where $\omega = \frac{2\pi}{T}$

In this section, first harmonic approximation is performed which means setting n = 1.

The variables of power electronic converters are inductor currents and capacitor voltages. The Fourier coefficients for the circuit variables as defined in (A.25) and (A.26) are complex values.

$$\langle i_L \rangle_1 \triangleq x_1 + jx_2; \qquad i_{L0} \triangleq x_5; \qquad \langle i_L \rangle_{-1} = \langle i_L \rangle_1^*; \tag{A.25}$$

$$\langle v_C \rangle_1 \triangleq x_3 + jx_4; \qquad \langle v_C \rangle_0 \triangleq x_6; \qquad \langle v_C \rangle_{-1} = \langle v_C \rangle_1^*; \tag{A.26}$$

The circuit variables can be written in terms of the new state variables using the above definitions.

$$i_L(t) = x_5 + 2x_1 \cos(\omega t) - 2x_2 \sin(\omega t) \tag{A.27}$$

$$v_C(t) = x_6 + 2x_3 \cos(\omega t) - 2x_4 \sin(\omega t) \tag{A.28}$$

Taking the Fourier transform of (A.1) by use of helpful formulations of (A.29)-(A.30)

$$\left\langle \frac{d}{dt} x \right\rangle_k = \frac{d}{dt} \langle x \rangle_k + jk\omega \langle x \rangle_k \tag{A.29}$$

$$\langle x \cdot y \rangle_k = \sum_i \langle x \rangle_{k-i} \langle y \rangle_i \tag{A.30}$$

A new set of differential equations will be obtained as expressed by

$$\begin{cases} \dfrac{d}{dt}\langle i_L \rangle_1 + j\omega \langle i_L \rangle_1 = \dfrac{1}{L}\left(\langle v_{in} \rangle_1 - \dfrac{1}{n}\left[\left(1 - \langle u \rangle_1\right)\langle v_C \rangle_0 + \left(1 - \langle u \rangle_0\right)\langle v_C \rangle_1 \right] \right), \\ \dfrac{d}{dt}\langle v_C \rangle_1 + j\omega \langle v_C \rangle_1 = -\dfrac{1}{C}\left(\dfrac{\langle v_C \rangle_1}{R} - \dfrac{1}{n}\left[\left(1 - \langle u \rangle_1\right)\langle i_L \rangle_0 + \left(1 - \langle u \rangle_0\right)\langle i_L \rangle_1 \right] \right), \end{cases} \tag{A.31}$$

After replacing (A.23) and (A.24) into (A.31) and substituting the Fourier coefficients of *u(t)*,

$$\langle u \rangle_1 = \frac{j}{2\pi}\left(e^{-j2\pi d} - 1 \right); \quad \langle u \rangle_0 = d \tag{A.32}$$

we will have

$$\begin{cases} \dot{x}_1 + j\dot{x}_2 + j\omega x_1 - \omega x_2 = \dfrac{1}{L}\left(\langle v_{in} \rangle_1 - \dfrac{1}{n}\left[\left(1 - \dfrac{j(e^{-j2\pi d} - 1)}{2\pi} \right) x_6 + (1-d)(x_3 + j x_4) \right] \right), \\ \dot{x}_3 + j\dot{x}_4 + j\omega x_3 - \omega x_4 = -\dfrac{1}{C}\left(\dfrac{x_3 + j x_4}{R} - \dfrac{1}{n}\left[\left(1 - \dfrac{j(e^{-j2\pi d} - 1)}{2\pi} \right) x_5 + (1-d)(x_1 + j x_2) \right] \right), \end{cases} \tag{A.33}$$

$$\begin{cases} \dot{x}_1 = \omega x_2 + \dfrac{-(1-d)}{nL} x_3 + \dfrac{\sin 2\pi d}{2n\pi L} x_6 + \dfrac{1}{L} Re\{\langle v_{in} \rangle_1\} \\ \dot{x}_2 = -\omega x_1 + \dfrac{-(1-d)}{nL} x_4 + \dfrac{-(1-\cos 2\pi d)}{2n\pi L} x_6 + \dfrac{1}{L} Im\{\langle v_{in} \rangle_1\} \\ \dot{x}_3 = \omega x_4 + \dfrac{(1-d)}{nC} x_1 + \dfrac{-1}{RC} x_3 + \dfrac{-\sin 2\pi d}{2n\pi C} x_5 \\ \dot{x}_4 = -\omega x_3 + \dfrac{(1-d)}{nC} x_2 + \dfrac{-1}{RC} x_4 + \dfrac{(1-\cos 2\pi d)}{2n\pi C} x_5 \end{cases} \tag{A.34}$$

To find the state space equations for x_5 and x_6 as the average values of the circuit variables, the dc coefficients must be derived using the circuit differential equations.

$$\begin{cases} \dfrac{d}{dt}\langle i_L \rangle_0 = \dfrac{1}{L}\left(\langle v_{in} \rangle_0 - \dfrac{1}{n}\left[(1 - \langle u \rangle_0)\langle v_C \rangle_0 - \langle u \rangle_1 \langle v_C \rangle_{-1} - \langle u \rangle_{-1} \langle v_C \rangle_1 \right] \right), \\ \dfrac{d}{dt}\langle v_C \rangle_0 = -\dfrac{1}{C}\left(\dfrac{\langle v_C \rangle_1}{R} - \dfrac{1}{n}\left[(1 - \langle u \rangle_0)\langle i_L \rangle_0 - \langle u \rangle_1 \langle i_L \rangle_{-1} - \langle u \rangle_{-1} \langle i_L \rangle_1 \right] \right), \end{cases} \tag{A.35}$$

$$\begin{cases} \dot{x}_5 = \dfrac{1}{L}\langle v_{in} \rangle_0 - \dfrac{1-d}{nL} x_6 + \dfrac{\sin 2\pi d}{n\pi L} x_3 - \dfrac{1-\cos 2\pi d}{n\pi L} x_4 \\ \dot{x}_6 = \dfrac{-1}{RC} x_6 + \dfrac{1-d}{nC} x_5 - \dfrac{\sin 2\pi d}{n\pi C} x_1 + \dfrac{1-\cos 2\pi d}{n\pi C} x_2 \end{cases} \tag{A.36}$$

Thus, a new set of state space equations are obtained whose state vector is $\mathbf{x} = [x_1\ x_2\ \ldots\ x_6]^T$.

$$\dot{\mathbf{x}} = \mathbf{A}\mathbf{x} + \mathbf{B}\mathbf{u} \tag{A.37}$$

and $\mathbf{u}$ is derived from the input voltage by $\mathbf{u} = \left[\mathrm{Re}\{\langle v_{in} \rangle_1\} \quad \mathrm{Im}\{\langle v_{in} \rangle_1\} \quad \langle v_{in} \rangle_0 \right]^T$

State space matrices A and B for the resulted state space model can be calculated as

$$\mathbf{A}=\begin{bmatrix} 0 & \omega & -(1-d)/nL & 0 & 0 & \sin(2\pi d)/2n\pi L \\ -\omega & 0 & 0 & -(1-d)/nL & 0 & -(1-\cos(2\pi d))/2n\pi L \\ (1-d)/nC & 0 & -1/RC & \omega & -\sin(2\pi d)/2n\pi C & 0 \\ 0 & (1-d)/nC & -\omega & -1/RC & (1-\cos(2\pi d))/2n\pi C & 0 \\ 0 & 0 & \sin(2\pi d)/n\pi L & -(1-\cos(2\pi d))/n\pi L & 0 & -(1-d)/nL \\ -\sin(2\pi d)/n\pi C & (1-\cos(2\pi d))/n\pi C & 0 & 0 & (1-d)/nC & -1/RC \end{bmatrix}$$

$$\mathbf{B}=\begin{bmatrix} 1/nL & 0 & 0 \\ 0 & 1/nL & 0 \\ 0 & 0 & 0 \\ 0 & 0 & 0 \\ 0 & 0 & 1/nL \\ 0 & 0 & 0 \end{bmatrix} \tag{A.38}$$

Providing a time-invariant large signal state space model, we can use software packages like Matlab/ Simulink to implement and control the resulted nonlinear system.

A.2 Buck converter/mode

Figure A-5 shows the schematic diagram of the studied buck converter topology. The foregoing analysis can be used for the buck mode of the studied bidirectional converter as well. The circuit differential equations are expressed by

$$\begin{cases} L\dfrac{di_L(t)}{dt}=\dfrac{1}{n}u(t)v_{in}(t)-v_C(t) \\ C\dfrac{dv_C(t)}{dt}=i_L(t)-\dfrac{v_C(t)}{R} \end{cases} \tag{A.39}$$

where $u(t)=\begin{cases}1, & 0<t<dT \\ 0, & dT<t<T\end{cases}$

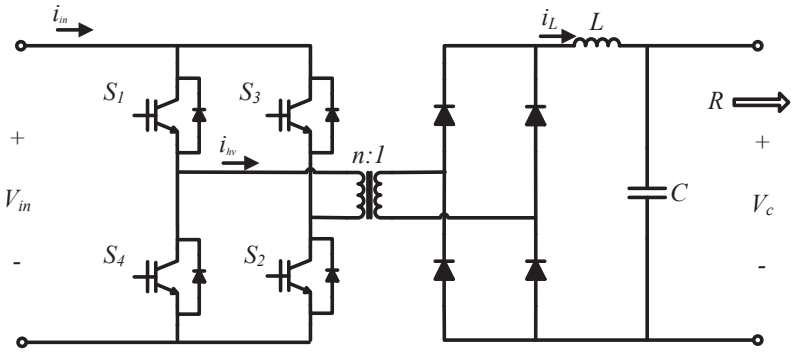

Figure A-5. Topology of an isolated full bridge buck converter

Figure A-6 shows the PWM gating signals in order to have the switching function,

u(t), as expressed in (A.39). *D* and T_S are duty cycle and switching period, respectively. During the on-time of either pair of switches, which lasts for $D \cdot T_S$, electric energy is transferred to the low voltage side and stored in the inductor. Then, during the dead time between the gating pulses, which lasts for $(1\text{-}D) \cdot T_S$, the energy stored in the inductor is discharged so that the energy stored in the inductor can be balanced.

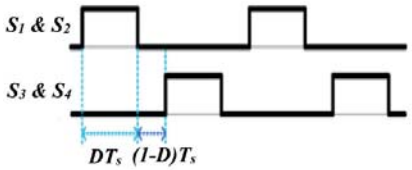

Figure A-6. Timing of the PWM gating signals for the full bridge buck converter [71]

A.2.1 Small signal average value model

In order to find the small signal model, the similar steps to the previous subsection are taken. By averaging over one switching period of (A.39), we will have

$$\begin{cases} L\dfrac{d\langle i_L(t)\rangle}{dt} = d(t)\left\langle \dfrac{1}{n}v_{in}(t) - v_C(t)\right\rangle + d'(t)\langle -v_C(t)\rangle \\ C\dfrac{d\langle v_C(t)\rangle}{dt} = \langle i_L(t)\rangle - \dfrac{\langle v_C(t)\rangle}{R} \\ \langle i_{in}\rangle = d(t)\langle i_{hv}\rangle \end{cases} \tag{A.40}$$

Separating the DC values from the small signal values of the variables, we obtain

$$\begin{cases} L\dfrac{d\hat{i}_L}{dt} = -\hat{v}_C + \dfrac{D}{n}\hat{v}_{in} + \dfrac{V_{in}}{n}\hat{d} \\ C\dfrac{d\hat{v}_C}{dt} = \hat{i}_L - \dfrac{1}{R}\hat{v}_C \\ \hat{i}_{in} = \dfrac{D}{n}\hat{i}_L + \dfrac{I_L}{n}\hat{d} \end{cases} \tag{A.41}$$

$$\frac{D}{n}V_{in} - DV_C + (-D')V_C = 0; \quad \boxed{V_C = \frac{D}{n}V_{in}} \tag{A.42}$$

$$I_L - \frac{V_C}{R} = 0; \quad \boxed{I_L = \frac{1}{R}V_C} \tag{A.43}$$

According to small signal equations (A.41), the small signal ac equivalent circuit for the isolated buck converter is derived in Figure A-7.

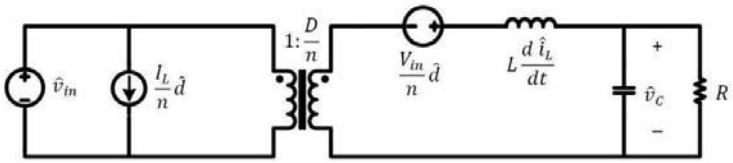

Figure A-7. Small signal ac equivalent circuit for the isolated buck converter

The buck converter can also be shown in the form of block diagram which is similar to how the boost converter was represented in Figure A-4, but with different formulations for the transfer functions. The transfer functions for the buck converter are calculated using the small signal equivalent circuit of Figure A-7.

$$G_{vv}(s)=\frac{D}{n}\frac{1}{1+\frac{L}{R}s+LCs^2} \tag{A.44}$$

$$G_{vd}(s)=\frac{V_{in}}{n}\frac{1}{1+\frac{L}{R}s+LCs^2} \tag{A.45}$$

$$Z_{out}(s)=\frac{Ls}{1+\frac{L}{R}s+LCs^2} \tag{A.46}$$

$$Z_{in}(s)=\frac{n^2R}{D^2}\frac{1+\frac{L}{R}s+LCs^2}{RCs+1} \tag{A.47}$$

$$G_{id}(s)=\frac{DV_C}{n^2R}\left(1+\frac{RCs+1}{1+\frac{L}{R}s+LCs^2}\right) \tag{A.48}$$

$$G_{ii}(s)=\frac{D}{n}\frac{1}{1+\frac{L}{R}s+LCs^2} \tag{A.49}$$

We can use the block diagram with the above transfer functions of the buck converter for small signal analysis of the system, and also for design the controllers utilizing linear control theory. In order to find the large signal models we will do the similar

steps to what we did for the boost converter in subsection A.1.2.

A.2.2 Nonlinear state space average model

The state space average model can be expressed in a nonlinear form to be appropriate for system level analysis. The state space equations can be derived by expanding equations (A.39).

$$\begin{cases} \begin{bmatrix} \frac{di_L(t)}{dt} \\ \frac{dv_C(t)}{dt} \end{bmatrix} = \begin{bmatrix} 0 & -\frac{1}{L} \\ \frac{1}{C} & -\frac{1}{RC} \end{bmatrix} \begin{bmatrix} i_L(t) \\ v_C(t) \end{bmatrix} + \begin{bmatrix} \frac{1}{nL} \\ 0 \end{bmatrix} v_{in}(t) \qquad for \quad 0 < t < dT, \\ \begin{bmatrix} \frac{di_L(t)}{dt} \\ \frac{dv_C(t)}{dt} \end{bmatrix} = \begin{bmatrix} 0 & -\frac{1}{L} \\ \frac{1}{C} & -\frac{1}{RC} \end{bmatrix} \begin{bmatrix} i_L(t) \\ v_C(t) \end{bmatrix} + \begin{bmatrix} 0 \\ 0 \end{bmatrix} v_{in}(t) \qquad for \quad dT < t < T, \end{cases} \tag{A.50}$$

We can see that the circuit can be expressed by two sets of state space equations for two states of switching. By averaging over the switching period these two sets of equations will be combined in a single set of state space equation.

$$\begin{bmatrix} \frac{di_L(t)}{dt} \\ \frac{dv_C(t)}{dt} \end{bmatrix} = \mathbf{A} \begin{bmatrix} i_L(t) \\ v_C(t) \end{bmatrix} + \left(d(t)\mathbf{B_1} + \left(1 - d(t)\right)\mathbf{B_2} \right) v_{in}(t) \tag{A.51}$$

where the matrices are as follow:

$$\mathbf{A} \triangleq \begin{bmatrix} 0 & -\frac{1}{L} \\ \frac{1}{C} & -\frac{1}{RC} \end{bmatrix}, \quad \mathbf{B_1} \triangleq \begin{bmatrix} \frac{1}{nL} \\ 0 \end{bmatrix}, \quad \mathbf{B_2} \triangleq \begin{bmatrix} 0 \\ 0 \end{bmatrix}$$

(A.51) represents the nonlinear state space average model of the buck converter. In order to model the ripples for higher accuracy, we will derive the generalized state space average modeling.

A.2.3 Generalized average modeling

The first step for deriving the generalized average model is to take the Fourier series from the circuit differential equations of the buck converter (A.39). It is done using the

same definitions and formulations as for the boost converter in subsection A.1.3.

$$\begin{cases} \dfrac{d}{dt}\langle i_L\rangle_1 + j\omega\langle i_L\rangle_1 = -\dfrac{1}{L}\left(\langle v_C\rangle_1 - \dfrac{1}{n}\left[\langle u\rangle_1\langle v_{in}\rangle_0 + \langle u\rangle_0\langle v_{in}\rangle_1\right]\right), \\ \dfrac{d}{dt}\langle v_C\rangle_1 + j\omega\langle v_C\rangle_1 = \dfrac{1}{C}\left(\langle i_L\rangle_1 - \dfrac{\langle v_C\rangle_1}{R}\right), \end{cases} \tag{A.52}$$

$$\begin{cases} \dot{x}_1 + j\dot{x}_2 + j\omega x_1 - \omega x_2 = -\dfrac{1}{L}\left(\dot{x}_3 + j\dot{x}_4 - \dfrac{1}{n}\left[\dfrac{j}{2\pi}\left(e^{-j2\pi d} - 1\right)\langle v_{in}\rangle_0 + d\langle v_{in}\rangle_1\right]\right), \\ \dot{x}_3 + j\dot{x}_4 + j\omega x_3 - \omega x_4 = \dfrac{1}{C}\left(x_1 + jx_2 - \dfrac{x_3 + jx_4}{R}\right), \end{cases} \tag{A.53}$$

Therefore, the first four state variables can be found by the following equation.

$$\begin{cases} \dot{x}_1 = \omega x_2 - \dfrac{1}{L}x_3 + \dfrac{\sin 2\pi d}{2n\pi L}\langle v_{in}\rangle_0 + \dfrac{d}{nL}Re\left\{\langle v_{in}\rangle_1\right\} \\ \dot{x}_2 = -\omega x_1 - \dfrac{1}{L}x_4 - \dfrac{1-\cos 2\pi d}{2n\pi L}\langle v_{in}\rangle_0 + \dfrac{d}{nL}Im\left\{\langle v_{in}\rangle_1\right\} \\ \dot{x}_3 = \omega x_4 + \dfrac{1}{C}x_1 - \dfrac{1}{RC}x_3 \\ \dot{x}_4 = -\omega x_3 + \dfrac{1}{C}x_2 - \dfrac{1}{RC}x_4 \end{cases} \tag{A.54}$$

To find the state space equations for x_5 and x_6 as the average values of the circuit variables, the dc coefficients must be derived using the circuit differential equations.

$$\begin{cases} \dfrac{d}{dt}\langle i_L\rangle_0 = -\dfrac{1}{L}\left(\langle v_C\rangle_0 - \dfrac{1}{n}\left[\langle u\rangle_0\langle v_{in}\rangle_0 + \langle u\rangle_1\langle v_{in}\rangle_{-1} + \langle u\rangle_{-1}\langle v_{in}\rangle_1\right]\right), \\ \dfrac{d}{dt}\langle v_C\rangle_0 = \dfrac{1}{C}\left(\langle i_L\rangle_0 - \dfrac{\langle v_C\rangle_0}{R}\right), \end{cases} \tag{A.55}$$

$$\begin{cases} \dot{x}_5 = -\dfrac{1}{L}x_6 + \dfrac{d}{nL}\langle v_{in}\rangle_0 + \dfrac{\sin 2\pi d}{n\pi L}Re\left\{\langle v_{in}\rangle_1\right\} - \dfrac{1-\cos 2\pi d}{n\pi L}Im\left\{\langle v_{in}\rangle_1\right\} \\ \dot{x}_6 = \dfrac{1}{C}x_5 - \dfrac{1}{RC}x_6 \end{cases} \tag{A.56}$$

Therefore, the new set of state space equations whose state vector is $\mathbf{x} = [x_1\ x_2\ \ldots\ x_6]^T$ is obtained by

$$\dot{\mathbf{x}} = \mathbf{\mathring{A}}\mathbf{x} + \mathbf{B}\mathbf{u} \tag{A.57}$$

where **u** is derived from the input voltage by

$$\mathbf{u} = \left[\mathrm{Re}\left\{ \langle v_{in} \rangle_1 \right\} \quad \mathrm{Im}\left\{ \langle v_{in} \rangle_1 \right\} \quad \langle v_{in} \rangle_0 \right]^T$$

And state space matrices A and B can be calculated by

$$\mathbf{A} = \begin{bmatrix} 0 & \omega & -1/L & 0 & 0 & 0 \\ -\omega & 0 & 0 & -1/L & 0 & 0 \\ 1/C & 0 & -1/RC & \omega & 0 & 0 \\ 0 & 1/C & -\omega & -1/RC & 0 & 0 \\ 0 & 0 & 0 & 0 & 0 & -1/L \\ 0 & 0 & 0 & 0 & 1/C & -1/RC \end{bmatrix} \tag{A.58}$$

$$\mathbf{B} = \begin{bmatrix} D/nL & 0 & \left(\sin 2\pi d\right)/2n\pi L \\ 0 & D/nL & -\left(1-\cos 2\pi d\right)/2n\pi L \\ -\left(1-\cos \pi d\right)/2n\pi L & -\left(1-\cos \pi d\right)/2n\pi L & -\left(1-\cos \pi d\right)/2n\pi L \\ 0 & 0 & 0 \\ \left(\sin 2\pi d\right)/n\pi L & -\left(1-\cos 2\pi d\right)/n\pi L & D/nL \\ -\left(1-\cos \pi d\right)/2n\pi L & -\left(1-\cos \pi d\right)/2n\pi L & -\left(1-\cos \pi d\right)/2n\pi L \end{bmatrix} \tag{A.59}$$

B
System Parameters

B.1 Electrical subsystems

The synchronous generator model is based on Park's equivalent circuit [128] with the following parameters.

TABLE B. I
PARAMETERS OF THE WOUND-ROTOR SYNCHRONOUS GENERATOR

$S = 300\ kVA$	$V = 320/460\ V$	$J = 3.35\ kg.m^2$	$r_s = 16.6\ m\Omega$,
$r_{fd} = 5.245\ m\Omega$	$L_{lfd} = 0.68\ mH$	$L_{ls} = 16.8\ mH$	$L_{md} = 5.85\ mH$,
$L_{mq} = 5.05\ mH$	$r'_{kd1} = 0.1526\ \Omega$	$L'_{lkd1} = 3.404\ mH$	$L'_{lkq1} = 3.404\ mH$,
$r'_{kq1} = 40.57\ m\Omega$	$p = 2$ pole pairs		
The Voltage Regulator-Exciter Parameters:			
$K_P = 0.4$	$K_I = 0.2$	$T_{fb} = 0.01\ s$	$T_{ff} = 1\ ms$

The induction motor is modeled in synchronously rotating dq reference frame [128] using the following parameters.

TABLE B. II
PARAMETERS OF THE INDUCTION MOTOR

$P = 400\ hp$	$V = 320/460\ V$	$p = 4$ poles	$J = 4.1\ kg.m^2$
$r_s = 7.6\ m\Omega$	$r'_r = 4.6\ m\Omega$	$L_{ls} = 0.15\ mH$	$L'_{lr} = 0.15\ mH$
$L_M = 5.2\ mH$			

TABLE B. III
PARAMETERS OF THE FUEL CELL MODULE

Cell no. = 130 cells	V_{nom} = 90 V	I_{nom} = 1333 A
I_{max} = 2250 A	T=700℃	P = 119.9 kW

TABLE B. IV
PARAMETERS OF THE LI-ION BATTERY BANK / ESS

In dynamic simulations (Chapter 0):			
$V_{full} = 93.1\ V$	$V_{nom} = 80\ V$	$Capacity = 5\ kAh$	
In efficiency analysis (Chapter 00):			
$V_{full} = 93.1\ V$	$V_{nom} = 80\ V$	$Capacity = 1\ kAh$	
$R_{bid} = 205\ m\Omega$	$R_{ess} = 0.3\ \Omega$	$P_{l0} = 100\ W$	$R_b = 0.8\ m\Omega$

TABLE B. V
ADDITIONAL PARAMETERS OF THE BIDIRECTIONAL CONVERTER FOR EFFICIENCY ANALYSIS

The Low-Voltage Side:			
$r_L = 3\ m\Omega$	$r_{C1} = 5\ m\Omega$	$r_T = 3\ m\Omega$	$R_{S,on} = 0.6\ m\Omega$
$R_{D,on} = 1.2\ m\Omega$	$C_O = 50\ nF$	$V_{D,fw} = 1.2\ V$	
The High-Voltage Side:			
$r_{C2} = 0.34\ \Omega$	$R_{S,on} = 2.9\ m\Omega$		
$R_{D,on} = 0.05\ m\Omega$	$C_O = 2.3\ nF$	$V_{D,fw} = 0.8\ V$	

B.2 Mechanical subsystems

TABLE B. VI
SPECIFIC FUEL CONSUMPTION OF DIESEL ENGINES AGAINST MECHANICAL POWER

SFC (gr/kWh)	**85 kW**	**150 kW**	**220 kW**	**300 kW**
Fixed speed	242	224	204.3	206
Variable speed	219	206.4	197	206

TABLE B. VII
QUADRATIC FUNCTION COEFFICIENTS OF FUEL CONSUMPTION AGAINST ELECTRICAL POWER

Coefficients	$\mathbf{C_0}$ (gr/h)	**a** (gr/kWh)	**b** (gr/kWh/kW)
Fixed speed	12761.7	92.38	0.235
Variable speed	8488.1	115.65	0.202

TABLE B. VIII
PROPELLER PARAMETERS

$K_T = -0.1060$	$K_Q = -0.0186$
$D = 0.5\ m$	$\rho = 1024\ kg/m^3$

TABLE B. IX
DIESEL ENGINE PARAMETERS

$P_m = 300\ kW$	$n_m = 30\ rps$
$N = 6$	$K_y = 1.5e6$
PI controller parameters of the governor:	
$K_P = 0.0077$	$K_I = 0.0165$

C

Loss Analysis of the Bidirectional Converter in Boost Mode

Assuming the inductor current is ripple-free, the transistors conduction losses of the bidirectional converter for boost mode are obtained by

$$p_{Sw,on} = \begin{cases} (2R_{S,on} \| 2R_{S,on}) i_L^2, & (0 \le t \le DT) \\ 2R_{S,on} i_L^2, & (DT \le t \le T) \end{cases} \tag{C.1}$$

Taking an average over the switching period, we have

$$P_{Sw,on} = R_{S,on} I_L^2 D + 2R_{S,on} I_L^2 (1-D) = (2-D) R_{S,on} I_L^2. \tag{C.2}$$

Assuming that the transistor output capacitance is linear, we calculate the switching losses by

$$P_{Sw,sw} = 4\left(\frac{f_{sw}}{2}\right) C_O V_{SM}^2 = \frac{1}{2} f_{sw} C_O \frac{V_{hv}^2}{n^2}. \tag{C.3}$$

The following equations hold for the diode conduction losses over a switching period.

$$p_D = \begin{cases} 0, & (0 \le t \le DT) \\ 2V_{fw} i_{hv} + 2R_{D,on} i_{hv}^2, & (DT \le t \le T) \end{cases} \tag{C.4}$$

Taking an average over the switching period, it yields

$$P_D = 2V_{fw}I_{hv} + 2R_{D,on}I_{hv,rms}^2 = 2V_{fw}\frac{P_{hv}}{V_{hv}} + 2R_{D,on}\left(\frac{P_{hv}}{V_{hv}\sqrt{1-D}}\right)^2. \quad \text{(C.5)}$$

The resistive losses of the passive elements are obtained by

$$P_L = r_L I_{L,rms}^2 = r_L\left(\frac{nP_{hv}}{(1-D)V_{hv}}\right)^2. \quad \text{(C.6)}$$

$$P_{C1} = r_{C1}I_{C1,rms}^2 = r_{C1}\left(\frac{DP_{hv}}{(1-D)V_{hv}}\right)^2. \quad \text{(C.7)}$$

$$P_{C2} = r_{C2}I_{C2,rms}^2 = r_{C2}\left(\frac{DV_{lv}}{\sqrt{12}f_{sw}L}\right)^2. \quad \text{(C.8)}$$

$$P_T = r_T I_{T,rms}^2 = r_T\left(\frac{nP_{hv}}{V_{hv}\sqrt{1-D}}\right)^2. \quad \text{(C.9)}$$

D

Analytical Support for Derivation of the Fuel Consumption

In order to derive and simplify the relation of the ship fuel consumption, the principle of energy balance over charge-discharge cycles is used. This appendix presents the primary equations of the fuel consumption that are used in the analysis in section 3.2.

D.1 The energy balance of the dc bus

The energy balance of the dc bus over a charge-discharge cycle yields

$$\int_{T_c} P_{bus}(t)dt = \int_{T_{ch}} P_{bus}(t)dt + \int_{T_{dis}} P_{bus}(t)dt = 0. \tag{D.1}$$

$$\text{where } P_{bus}(t) = \begin{cases} P_{s,k+1}(t) - P_L(t) - P_{l,ess}^{ch}(t) & 0 \le t < D_s T_c \\ P_{s,k}(t) - P_L(t) - P_{l,ess}^{dis}(t) & D_s T_c \le t < T_c \end{cases} \tag{D.2}$$

Replacing (D.2) in (D.1), equations (D.3) and (D.4) are obtained.

$$\int_{T_{ch}} [P_{s,k+1}(t) - P_L(t)]dt - \int_{T_{ch}} P_{l,ess}^{ch}(t)dt + \int_{T_{dis}} [P_{s,k}(t) - P_L(t)]dt - \int_{T_{dis}} P_{l,ess}^{dis}(t)dt = 0. \tag{D.3}$$

$$\int_{T_{ch}} P_{s,k+1}(t)dt + \int_{T_{dis}} P_{s,k}(t)dt = \int_{T_{ch}} P_L(t)dt + \int_{T_{dis}} P_L(t)dt + \int_{T_{ch}} P_{l,ess}^{ch}(t)dt + \int_{T_{dis}} P_{l,ess}^{dis}(t)dt. \tag{D.4}$$

where the losses of the energy storage system are obtained by using (3.16) which yields

$$\begin{cases} P_{l,ess}^{ch}(t) = \dfrac{R_{ess}}{V_{bus}^2}(P_{s,k+1}(t) - P_L(t))^2. \\ P_{l,ess}^{dis}(t) = \dfrac{R_{ess}}{V_{bus}^2}(P_{s,k}(t) - P_L(t))^2. \end{cases} \tag{D.5}$$

The constant term of the ESS losses in (3.16) constitutes a power loss of 100W. This constant value is considered as an additional load to the system loading so that only the second-order term will remain in the fuel consumption analysis.

In order to obtain (3.23) from (3.21) the following relations have been used. Similar relations hold for $P_{s,k}$.

$$\int_{T_{ch}} P_{s,k+1}^2(t)dt = P_{sa,k+1}^2 + \int_{T_{ch}} (P_{s,k+1}(t) - P_{sa,k+1})^2 dt. \tag{D.6}$$

$$\int_{T_{ch}} (P_{s,k+1}(t) - P_{sa,k+1})^2 dt = \int_{T_{ch}} \alpha_{k+1}^2 (P_L(t) - P_{La})^2 dt = \alpha_{k+1}^2 T_{ch} R_{eq}^2. \tag{D.7}$$

$$\int_{T_{ch}} (P_{s,k+1}(t) - P_{sa,k+1})(P_L(t) - P_{La})dt = \int_{T_{ch}} \alpha_{k+1}(P_L(t) - P_{La})^2 dt = \alpha_{k+1} T_{ch} R_{eq}^2. \tag{D.8}$$

$$\begin{aligned} a_{k+1}\int_{T_{ch}} P_{s,k+1}(t)dt + a_k \int_{T_{dis}} P_{s,k}(t)dt = aP_{La}(T_{ch} + T_{dis}) + aT_{ch}\frac{R_{ess}}{V_{bus}^2}[(P_{sa,k+1} - P_{La})^2 + \\ R_{eq}^2(1 - 2\alpha_{k+1} + \alpha_{k+1}^2)] + aT_{dis}\frac{R_{ess}}{V_{bus}^2}[(P_{sa,k} - P_{La})^2 + R_{eq}^2(1 - 2\alpha_k + \alpha_k^2)]. \end{aligned} \tag{D.9}$$

D.2 The energy balance of the ESS

The energy balance of the ESS over a charge-discharge cycle is used to find (3.25) by using the following relations.

$$\Delta E_{ch} + \Delta E_{dis} = 0. \tag{D.10}$$

$$\begin{aligned} \Delta E_{ch} = \int_{T_{ch}} [P_{s,k+1}(t) - P_L(t)]dt - \int_{T_{ch}} P_{l,ess}^{ch}(t)dt = \\ T_{ch}\{P_{sa,k+1} - P_{La} - \frac{R_{ess}}{V_{bus}^2}[(P_{sa,k+1} - P_{La})^2 + R_{eq}^2(1 - \alpha_{k+1})^2]\}. \end{aligned} \tag{D.11}$$

$$\Delta E_{dis} = \int_{T_{dis}} [P_{s,k}(t) - P_L(t)]dt - \int_{T_{dis}} P_{l,ess}^{dis}(t)dt = \\ T_{dis}\{P_{sa,k} - P_{La} - \frac{R_{ess}}{V_{bus}^2}[(P_{sa,k} - P_{La})^2 + R_{eq}^2(1-\alpha_k)^2]\}. \quad \text{(D.12)}$$

References

[1] T. J. McCoy, "Trends in ship electric propulsion," *Proceedings of the IEEE Power Engineering Society Transmission and Distribution Conference,* vol. 1, pp. 343-346, 2002.

[2] A. K. Adnanes, "Maritime electrical installations and diesel electricpropulsion," *ABB AS Marine,* 2003.

[3] G. Seenumani, H. Peng, and J. Sun, "A reference governor-based hierarchical control for failure mode power management of hybrid power systems for all-electric ships," *Journal of Power Sources,* vol. 196, pp. 1599-1607, 2/1/ 2011.

[4] N. H. Doerry and J. C. Davis, "Integrated power system for marine applications," *Naval Engineers Journal,* vol. 106, pp. 77-90, 1994.

[5] M. Bash, R. R. Chan, J. Crider, C. Harianto, J. Lian, J. Neely*, et al.*, "A Medium Voltage DC Testbed for ship power system research," in *IEEE Electric Ship Technologies Symposium*, 2009, pp. 560-567.

[6] R. Nilsen and I. Sorfonn, "Hybrid power generation systems," in *13th European Conference on Power Electronics and Applications*, 2009.

[7] B. Zahedi and L. E. Norum, "Modeling and Simulation of All-Electric Ships with Low Voltage DC Hybrid Power Systems," *IEEE Trans. on Power Electronics,* vol. 28, pp. 4525-4537, 2013.

[8] J. Hansen, J. Lindtjørn, and K. Vanska, "Onboard DC Grid for enhanced DP operation in ships," presented at the Dynamic Positioning Conference, 2011.

[9] J. F. Hansen, J. O. Lindtjorn, U. U. Odegaard, and T. A. Myklebust, "Increased operational performance of OSVs by Onboard DC Grid," presented at the 4th International Conference on Technology and Operation of Offshore Support Vessels, 2011.

[10] S. Chiniforoosh, J. Jatskevich, A. Yazdani, V. Sood, V. Dinavahi, J. A. Martinez*, et al.*, "Definitions and applications of dynamic average models for analysis of power systems," *IEEE Transactions on Power Delivery,* vol. 25, pp. 2655-2669, 2010.

[11] J. M. Apsley, A. González-Villaseñor, M. Barnes, A. C. Smith, S. Williamson, J. D. Schuddebeurs*, et al.*, "Propulsion drive models for full electric marine propulsion systems," *IEEE Transactions on Industry Applications,* vol. 45, pp. 676-684, 2009.

[12] A. Emadi, "Modeling and analysis of multiconverter dc power electronic systems using the generalized state-space averaging method," *IEEE Transactions on Industrial Electronics,* vol. 51, pp. 661-668, 2004.

[13] K. Hochkirch and V. Bertram, "Options for fuel saving for ships," *MareForum: Maritime Transportation of Energy,* 2010.

[14] P. Thounthong, S. Raël, and B. Davat, "Energy management of fuel cell/battery/supercapacitor hybrid power source for vehicle applications," *Journal of Power Sources,* vol. 193, pp. 376-385, 2009.

[15] M. Bash, R. R. Chan, J. Crider, C. Harianto, J. Lian, J. Neely*, et al.*, "A medium voltage DC testbed for ship power system research," *IEEE Electric Ship Technologies Symposium, ESTS 2009,* pp. 560-567, 2009.

[16] R. R. Chan, Y. Lee, S. D. Sudhoff, and E. L. Zivi, "Evolutionary optimization of power electronics based power systems," *IEEE Transactions on Power Electronics,* vol. 23, pp. 1907-1917, 2008.

[17] J. S. Lai and D. J. Nelson, "Energy management power converters in hybrid electric and fuel cell vehicles," *Proceedings of the IEEE,* vol. 95, pp. 766-777, 2007.

[18] J. F. Hansen, J. O. Lindtjorn, U. U. Odegaard, and T. A. Myklebust, "Increased operational performance of OSVs by onboard dc Grid," *Presented at the 4th International Conference Technol. Oper. Offshore Support Vessels,* 2011.

[19] R. W. Erickson and D. Maksimovic, *Fundamentals of Power Electronics,* 2001.

[20] B. Zahedi, O. C. Nebb, and L. E. Norum, "An isolated bidirectional converter modeling for hybrid electric ship simulations," *Proc. IEEE Transp. Electrification Conf. Expo.,* 2012.

[21] B. Zahedi and L. E. Norum, "Modeling, analysis and control of an isolatedboost converter for system level studies," *Proc. Aegean Conf. ElectricMach. Power Electron.,* 2011.

[22] S. R. Sanders, J. M. Noworolski, X. Z. Liu, and G. C. Verghese, "Generalized averaging method for power conversion circuits," *IEEE Transactions on Power Electronics,* vol. 6, pp. 251-259, 1991.

[23] J. Zhang, J. S. Lai, and W. Yu, "Bidirectional DC-DC converter modeling and unified controller with digital implementation," *Conference Proceedings - IEEE Applied Power Electronics Conference and Exposition - APEC,* pp. 1747-1753, 2008.

[24] P. J. Barrre, A. Bouscayrol, P. Delarue, E. Dumetz, F. Giraud, J. P. Hautier*, et al.*, "Inversion-based controlof electromechanical systems using causal graphical descriptions," *InProc. IEEE 32nd Annu. Conf. Ind. Electron.,* pp. 5276-5281, 2006.

[25] P. C. Krause and T. A. Lipo, "ANALYSIS AND SIMPLIFIED REPRESENTATIONS OF RECTIFIER-INVERTER INDUCTION MOTOR DRIVE," *IEEE-Trans on Power Apparatus & Systems,* vol. PAS-88, pp. 588-596, 1969.

[26] H. A. Peterson and P. C. Krause, "A direct and quadrature-axis representation of a parallel AC and DC power system," *IEEE Transactions on Power Apparatus and Systems,* vol. PAS-85, pp. 210-225, 1966.

[27] S. Chiniforoosh, H. Atighechi, A. Davoudi, J. Jatskevich, A. Yazdani, S. Filizadeh*, et al.*, "Dynamic average modeling of front-end diode rectifier loads considering discontinuous conduction mode and unbalanced operation," *IEEE Transactions on Power Delivery,* vol. 27, pp. 421-429, 2012.

[28] J. Jatskevich, S. D. Pekarek, and A. Davoudi, "Parametric average-value model of synchronous machine-rectifier systems," *IEEE Transactions on Energy Conversion,* vol. 21, pp. 9-18, 2006.

[29] S. D. Sudhoff and O. Wasynczuk, "Analysis and average-value modeling of line-commutated converter. Synchronous machine systems," *IEEE Transactions on Energy Conversion,* vol. 8, pp. 92-99, 1993.

[30] S. D. Sudhoff, K. A. Corzine, H. J. Hegner, and D. E. Delisle, "Transient and dynamic average-value modeling of synchronous machine fed load-commutated converters," *IEEE Transactions on Energy Conversion,* vol. 11, pp. 508-514, 1996.

[31] I. Jadrić, D. Borojević, and M. Jadrić, "Modeling and control of a synchronous generator with an active DC load," *IEEE Transactions on Power Electronics,* vol. 15, pp. 303-311, 2000.

[32] C. T. Rim, N. S. Choi, G. C. Cho, and G. H. Cho, "Complete DC and AC analysis of three-phase controlled-current PWM rectifier using circuit D-Q transformation," *IEEE Transactions on Power Electronics,* vol. 9, pp. 390-396, 1994.

[33] J. F. Hansen, A. K. Ådnanes, and T. I. Fossen, "Mathematical Modelling of Diesel-Electric Propulsion Systems for Marine Vessels," *Mathematical and Computer Modelling of Dynamical Systems,* vol. 7, pp. 323-355, 2001.

[34] R. Izadi-Zamanabadi and M. Blanke, "A ship propulsion system as a benchmark for fault-tolerant control," *Control Engineering Practice,* vol. 7, pp. 227-239, 1999.

[35] R. Ferreiro, M. Haro, and F. J. Velasco, "Trends on modeling techniques applied on ship's propulsion system monitoring," *Journal of Maritime Research,* vol. 2, pp. 87-104, 2005.

[36] T. I. Fossen, *Handbook of Marine Craft Hydrodynamics and Motion Control,* 2011.

[37] "Marine Systems Simulator (MSS), Norwegian University of Science and Technology [Online]. Available: http://www.marinecontrol.org."

[38] O. N. Smogeli, "Control of marine propellers: From normal to extreme conditions," PhD Dissertation, Marine Technology, Norwegian University of Science and Technology, 2006.

[39] T. A. Pedersen, "Bond Graph Modeling of Marine Power Systems," PhD Dissertation, Marine Technology, Norwegian University of Science and Technology, 2009.

[40] O. C. Nebb, B. Zahedi, J. O. Lindtjorn, and L. E. Norum, "Increased fuel efficiency in ship LVDC power distribution systems," *Proc. IEEEVehicle Power Propul. Conf.,* 2012.

[41] "GNC Lab [Online]. Available: http://www.itk.ntnu.no/ansatte/Fossen_Thor/GNC/cybership2.htm."

[42] S. De Breucker, E. Peeters, and J. Driesen, "Possible applications of pluginhybrid electric ships," *Proc. IEEE Electric Ship Technol. Symp.,* pp. 560-567, 2009.

[43] E. Ovrum and G. Dimopoulos, "A validated dynamic model of the first marine molten carbonate fuel cell," *Applied Thermal Engineering,* vol. 35, pp. 15-28, 2012.

[44] E. Fontell, "Wartsila fuel cell development program," *Proc. 8th Annu. Green Ship Technol. Conf.,* 2011.

[45] H. Kakigano, Y. Miura, and T. Ise, "Distribution voltage control for DC microgrids using fuzzy control and gain-scheduling technique," *IEEE Transactions on Power Electronics,* vol. 28, pp. 2246-2258, 2013.

[46] A. M. Roslan, K. H. Ahmed, S. J. Finney, and B. W. Williams, "Improved instantaneous average current-sharing control scheme for parallel-connected inverter considering line impedance impact in microgrid networks," *IEEE Transactions on Power Electronics,* vol. 26, pp. 702-716, 2011.

[47] A. Ådnanes, *Maritime electrical installations and diesel electric propulsion*. Oslo: ABB AS Marine, 2003.

[48] J. Apsley, A. Gonzalez-Villasenor, M. Barnes, A. Smith, S. Williamson, J. Schuddebeurs*, et al.*, "Propulsion drive models for full electric marine propulsion systems," *IEEE Trans. on Industry Applications,* vol. 45, pp. 676-684, 2009.

[49] P. Mitra and G. Venayagamoorthy, "An adaptive control strategy for DSTATCOM applications in an electric ship power system," *IEEE Transactions on Power Electronics,* vol. 25, pp. 95-104, 2010.

[50] M. C. Trummel and A. F. Burke, "Development history of the hybrid test vehicle," *IEEE Transactions on Vehicular Technology,* vol. 32, pp. 7-14, 1983.

[51] S. Barsali, M. Ceraolo, and A. Possenti, "Techniques to control the electricity generation in a series hybrid electrical vehicle," *IEEE Trans. on Energy Conversion,* vol. 17, pp. 260-266, 2002.

[52] S. Williamson, M. Lukic, and A. Emadi, "Comprehensive drive train efficiency analysis of hybrid electric and fuel cell vehicles based on motor-controller efficiency modeling," *IEEE Trans. on Power Electronics,* vol. 21, pp. 730-740, 2006.

[53] A. Payman, S. Pierfederici, and F. Meibody-Tabar, "Energy management in a fuel cell/supercapacitor multisource/multiload electrical hybrid system," *IEEE Transactions on Power Electronics,* vol. 24, pp. 2681-2691, 2009.

[54] C. C. Chan, a. Bouscayrol, and K. Chen, "Electric, Hybrid, and Fuel-Cell Vehicles: Architectures and Modeling," *IEEE Transactions on Vehicular Technology,* vol. 59, pp. 589-598, 2010.

[55] J. Popović-Gerber, J. A. Oliver, N. Cordero, T. Harder, J. A. Cobos, M. Hayes*, et al.*, "Power electronics enabling efficient energy usage: Energy savings potential and technological challenges," *IEEE Transactions on Power Electronics,* vol. 27, pp. 2338-2353, 2012.

[56] S. D. Breucker, E. Peeters, and J. Driesen, "Possible applications of Plug-in Hybrid Electric Ships," in *IEEE Electric Ship Technologies Symposium*, 2009, pp. 310-317.

[57] I.-Y. Chung, W. Liu, M. Andrus, K. Schoder, D. a. Cartes, and M. Steurer, "Integration of a bi-directional dc-dc converter model into a large-scale system simulation of a shipboard MVDC power system," in *IEEE Electric Ship Technologies Symposium*, 2009, pp. 318-325.

[58] F. Dupriez-Robin, L. Loron, F. Claveau, and P. Chevrel, "Design and optimization of an hybrid sailboat by a power modeling approach," in *IEEE Electric Ship Technologies Symposium*, 2009, pp. 270-277.

[59] O. C. Nebb, B. Zahedi, J. O. Lindtjorn, and L. E. Norum, "Increased fuel efficiency in ship LVDC power distribution systems," in *Vehicle Power and Propulstion Conference*, 2012, pp. 564-568

[60] B. J. Vartdal and C. Chryssakis, "Potential Benefits of Hybrid Powertrain Systems for Various Ship Types," in *International Scientific Conference on Hybrid and Electric Vehcicles*, 2011, pp. 1-12.

[61] (2012) Jaguar, A big cat far from becoming extinct. *MARITIME BY HOLLAND*. 40-45.

[62] R. J. Wai, S. J. Jhung, J. J. Liaw, and Y. R. Chang, "Intelligent optimal energy management system for hybrid power sources including fuel cell and battery," *IEEE Transactions on Power Electronics,* vol. 28, pp. 3231-3244, 2013.

[63] O. Laldin, M. Moshirvaziri, and O. Trescases, "Predictive algorithm for optimizing power flow in hybrid ultracapacitor/battery storage systems for light electric vehicles," *IEEE Transactions on Power Electronics,* vol. 28, pp. 3882-3895, 2013.

[64] S. Lu, S. Hillmansen, and C. Roberts, "A power-management strategy for multiple-unit railroad vehicles," *IEEE Transactions on Vehicular Technology,* vol. 60, pp. 406-420, 2011.

[65] Y. L. Murphey, J. Park, Z. Chen, M. L. Kuang, M. A. Masrur, and A. M. Phillips, "Intelligent hybrid vehicle power control part I: Machine learning of optimal vehicle power," *IEEE Transactions on Vehicular Technology,* vol. 61, pp. 3519-3530, 2012.

[66] S. Barsali, C. Miulli, and A. Possenti, "A control strategy to minimize fuel consumption of series hybrid electric vehicles," *IEEE Trans. on Energy Conversion,* vol. 19, pp. 187-195, 2004.

[67] C. Mademlis, J. Xypteras, and N. Margaris, "Loss minimization in wound-field cylindrical rotor synchronous motor drives," *IEEE Transactions on Power Electronics,* vol. 13, pp. 288-296, 1998.

[68] J. Lai and D. Nelson, "Energy management power converters in hybrid electric and fuel cell vehicles," *Proceedings of the IEEE,* vol. 95, pp. 766-777, 2007.

[69] M. Yilmaz and P. T. Krein, "Review of battery charger topologies, charging power levels, and infrastructure for plug-in electric and hybrid vehicles," *IEEE Transactions on Power Electronics,* vol. 28, pp. 2151-2169, 2013.

[70] I. Y. Chung, W. Liu, D. A. Cartes, S. H. Cho, and H. K. Kang, "Controller optimization for bidirectional power flow in Medium-Voltage DC power systems," *Journal of Electrical Engineering and Technology,* vol. 6, pp. 750-759, 2011.

[71] I. Y. Chung, W. Liu, K. Schoder, and D. A. Cartes, "Integration of a bi-directional DC-DC converter model into a real-time system simulation of a shipboard medium voltage DC system," *Electric Power Systems Research,* vol. 81, pp. 1051-1059, 2011.

[72] M. K. Kazimierczuk, *Pulse-Width Modulated DC-DC Power Converters*, 1 ed.: Wiley, 2008.

[73] A. P. Schmidt, M. Bitzer, A. W. Imre, and L. Guzzella, *Journal of Power Sources,* vol. 195, pp. 5071-5080, 2010.

[74] V. R. Subramanian, V. Boovaragavan, V. Ramadesigan, and M. Arabandi, *Journal of the Electrochemical Society,* vol. 156, pp. A260-A271, 2009.

[75] C. Y. Wang and V. Srinivasan, *Journal of Power Sources,* vol. 110, pp. 364-376, 2002.

[76] X. Hu, S. Li, and H. Peng, "A comparative study of equivalent circuit models for Li-ion batteries," *Journal of Power Sources,* vol. 198, pp. 359-367, 2012.

[77] O. Tremblay, L. A. Dessaint, and A. I. Dekkiche, "A Generic Battery Model for the Dynamic Simulation of Hybrid Electric Vehicles," in *Vehicle Power and Propulsion Conference, 2007. VPPC 2007. IEEE*, 2007, pp. 284-289.

[78] R. D. Middlebrook, "Input filter considerations in design and application of switching regulators," *Proceedings of IEEE Industry Applications Society Annual Meeting,* pp. 366-382, 1976.

[79] R. D. Middlebrook, "Design techniques for preventing input-filter oscillations in switched-mode regulators," *Proc. Powercon,* vol. 5, pp. A3.1-A3.16, 1978.

[80] C. M. Wildrick, F. C. Lee, B. H. Cho, and B. Choi, "A method of defining the load impedance specification for a stable distributed power system," *IEEE Trans. Power Electron.,* vol. 10, pp. 280-285, 1995.

[81] S. D. Sudhoff and S. F. Glover, "Modeling techniques, stability analysis, and design criteria for DC power systems with experimental validation," *SAE Trans. J. Aerosp.,* pp. 52-67, 1998.

[82] S. D. Sudhoff and S. F. Glover, "Admittance space stability analysis of power electronic systems," *IEEE Transactions on Aerospace and Electronic Systems,* vol. 36, pp. 965-973, 2000.

[83] S. D. Sudhoff and J. M. Crider, "Advancements in generalized immittance based stability analysis of DC power electronics based distribution systems," in *IEEE Electric Ship Technologies Symposium*, 2011, pp. 207-212.

[84] A. Emadi, B. Fahimi, and M. Ehsani, "On the concept of negative impedance instability in the more electric aircraft power systems with constant power loads," *Presented at the 34th Intersociety Energy Conversion Engineering Conference,* 1999.

[85] A. Emadi, A. Khaligh, C. H. Rivetta, and G. A. Williamson, "Constant power loads and negative impedance instability in automotive systems: Definition, modeling, stability, and control of power electronic converters and motor drives," *IEEE Transactions on Vehicular Technology,* vol. 55, pp. 1112-1125, 2006.

[86] R. McNeal and M. Belkhayat, "DC link stabiliy design tool," *IEEE Electric Ship Technologies Symposium,* pp. 288-293, 2007.

[87] B. P. Loop, S. D. Sudhoff, S. H. Zak, and E. L. Zivi, "Estimating regions of asymptotic stability of power electronics systems using genetic algorithms," *IEEE Transactions on Control Systems Technology,* vol. 18, pp. 1011-1022, 2010.

[88] M. Belkhayat, R. Cooley, and A. Witulski, "Large signal stability criteria for distributed systems with constant power loads," *In Proceeding of IEEE Power Electronics Specialists Conference,* vol. 2, pp. 1333-1338, 1995.

[89] A. Griffo, J. Wang, and D. Howe, "Large signal stability analysis of DC power system with constant power loads," *IEEE Vehicle Power and Propulsion Conference,* pp. 1-6, 2008.

[90] C. J. Sullivan, S. D. Sudhoff, E. L. Zivi, and S. H. Zak, "Methods of optimal lyapunov function generation with application to power electronic converters and systems," *IEEE Electric Ship Technologies Symposium,* pp. 267-274, 2007.

[91] D. Marx, S. Pierfederici, B. Nahid-Mobarakeh, and B. Davat, "Contribution to determination of domain of attraction in power systems: Application to drives with input filter," *In the Proceeding of Iindustrial Application Society,* pp. 1-8, 2009.

[92] D. Marx, P. Magne, B. Nahid-Mobarakeh, S. Pierfederici, and B. Davat, "Large signal stability analysis tools in DC power systems with constant power loads and variable power loads-A review," *IEEE Transactions on Power Electronics,* vol. 27, pp. 1773-1787, 2012.

[93] S. D. Sudhoff, K. A. Corzine, S. F. Glover, H. J. Hegner, and H. N. Robey Jr, "DC link stabilized field oriented control of electric propulsion systems," *IEEE Transactions on Energy Conversion,* vol. 13, pp. 27-33, 1998.

[94] P. Liutanakul, S. Pierfederici, and F. Meibody-Tabar, "DC-link capacitor reduction of a controlled rectifier supplying N inverter-motor drive systems by compensating the load variations," *PESC Record - IEEE Annual Power Electronics Specialists Conference,* vol. 2, pp. 1298-1303, 2004.

[95] L. Harnefors and K. Pietiläinen, "Inverter DC-link stabilizing control with improved voltage sag ride-through capability," *Presented at the Eur. Conf. Power Electron. Appl.,* 2005.

[96] H. Mosskull, J. Galić, and B. Wahlberg, "Stabilization of induction motor drives with poorly damped input filters," *IEEE Transactions on Industrial Electronics,* vol. 54, pp. 2724-2734, 2007.

[97] X. Liu, A. J. Forsyth, and A. M. Cross, "Negative input-resistance compensator for a constant power load," *IEEE Transactions on Industrial Electronics,* vol. 54, pp. 3188-3196, 2007.

[98] A. M. Rahimi, G. A. Williamson, and A. Emadi, "Loop-cancellation technique: A novel nonlinear feedback to overcome the destabilizing effect of constant-power loads," *IEEE Transactions on Vehicular Technology,* vol. 59, pp. 650-661, 2010.

[99] E. Jamshidpour, B. Nahid-Mobarakeh, P. Poure, S. Pierfederici, F. Meibody-Tabar, and S. Saadate, "Distributed active resonance suppression in hybrid DC power systems under unbalanced loads conditions," *IEEE Trans. Power Electron.,* vol. 28, pp. 1833-1842, 2013.

[100] P. Liutanakul, A. B. Awan, S. Pierfederici, B. Nahid-Mobarakeh, and F. Meibody-Tabar, "Linear stabilization of a dc bus supplying a constant power load: A general design approach," *IEEE Transactions on Power Electronics,* vol. 25, pp. 475-488, 2010.

[101] G. O. Kalcon, G. P. Adam, O. Anaya-Lara, S. Lo, and K. Uhlen, "Small-signal stability analysis of multi-terminal VSC-based DC transmission systems," *IEEE Transactions on Power Systems,* vol. 27, pp. 1818-1830, 2012.

[102] N. R. Chaudhuri, R. Majumder, B. Chaudhuri, and J. Pan, "Stability analysis of VSC MTDC grids connected to multimachine AC systems," *IEEE Transactions on Power Delivery,* vol. 26, pp. 2774-2784, 2011.

[103] N. Bottrell, M. Prodanovic, and T. C. Green, "Dynamic stability of a microgrid with an active load," *IEEE Transactions on Power Electronics,* vol. 28, pp. 5107-5119, 2013.

[104] S. Anand and B. G. Fernandes, "Reduced-order model and stability analysis of low-voltage dc microgrid," *IEEE Transactions on Industrial Electronics,* vol. 60, pp. 5040-5049, 2013.

[105] A. Fuchs, M. Imhof, T. Demiray, and M. Morari, "Stabilization of large power systems using vsc-hvdc and model predictive control," *IEEE Transactions on Power Delivery,* vol. 29, pp. 480-488, 2014.

[106] X. Lu, K. Sun, J. M. Guerrero, J. C. Vasquez, and L. Huang, "State-of-charge balance using adaptive droop control for distributed energy storage systems in DC microgrid applications," *IEEE Transactions on Industrial Electronics,* vol. 61, pp. 2804-2815, 2014.

[107] Y. A. R. I. Mohamed, A. A. A. Radwan, and T. K. Lee, "Decoupled reference-voltage-based active DC-link stabilization for PMSM drives with tight-speed regulation," *IEEE Transactions on Industrial Electronics,* vol. 59, pp. 4523-4536, 2012.

[108] A. A. A. Radwan and Y. A. R. I. Mohamed, "Linear active stabilization of converter-dominated DC microgrids," *IEEE Transactions on Smart Grid,* vol. 3, pp. 203-216, 2012.

[109] W. J. Lee and S. K. Sul, "DC-link voltage stabilization for reduced DC-link capacitor inverter," *IEEE Transactions on Industry Applications,* vol. 50, pp. 404-414, 2014.

[110] J. Lago and M. L. Heldwein, "Operation and control-oriented modeling of a power converter for current balancing and stability improvement of DC active distribution networks," *IEEE Transactions on Power Electronics,* vol. 26, pp. 877-885, 2011.

[111] S. R. Sanders and G. C. Verghese, "Lyapunov-based control for switched power converters," *IEEE Transactions on Power Electronics,* vol. 7, pp. 17-24, 1992.

[112] A. B. Awan, B. Nahid-Mobarakeh, and S. Pierfederici, "Nonlinear stabilization of a DC-bus supplying a constant power load," *Conf. Rec. IEEE IAS Annu. Meeting,* pp. 1-8, 2009.

[113] A. B. Awan, S. Pierfederici, B. Nahid-Mobarakeh, and F. Meibody-Tabar, "Active stabilization of a poorly damped input filter supplying a constant power load," *2009 IEEE Energy Conversion Congress and Exposition, ECCE 2009,* pp. 2991-2997, 2009.

[114] P. Magne, S. Pierfederici, and B. Nahid-Mobarakeh, "DC-link voltage large signal stabilization and transient control using a virtual capacitor," *Proc. Ind. Appl. Soc.,* pp. 1-8, 2010.

[115] T. Hu, "A nonlinear-system approach to analysis and design of power-electronic converters with saturation and bilinear terms," *IEEE Transactions on Power Electronics,* vol. 26, pp. 399-410, 2011.

[116] S. R. Huddy and J. D. Skufca, "Amplitude death solutions for stabilization of dc microgrids with instantaneous constant-power loads," *IEEE Transactions on Power Electronics,* vol. 28, pp. 247-253, 2013.

[117] P. Magne, B. Nahid-Mobarakeh, and S. Pierfederici, "General active global stabilization of multiloads DC-power networks," *IEEE Transactions on Power Electronics,* vol. 27, pp. 1788-1798, 2012.

[118] T. Takagi and M. Sugeno, "Fuzzy identification of systems and its applications to modeling and control," *IEEE Transactions on Systems, Man and Cybernetics,* vol. 15, pp. 116-132, 1985.

[119] Y. Blanco, W. Perruquetti, and P. Borne, "Stability and Stabilization of Nonlinear Systems and Takagi-Sugeno's Fuzzy Models," *Mathematical Problems in Engineering,* vol. 7, pp. 221-240, 2001.

[120] M. Zandi, A. Payman, J. P. Martin, S. Pierfederici, B. Davat, and F. Meibody-Tabar, "Flatness based control of a hybrid power source with fuel cell / supercapacitor / battery," *2010 IEEE Energy Conversion Congress and Exposition, ECCE 2010 - Proceedings,* pp. 1629-1634, 2010.

[121] J. M. Guerrero, J. C. Vasquez, J. Matas, L. G. De Vicuña, and M. Castilla, "Hierarchical control of droop-controlled AC and DC microgrids - A general approach toward standardization," *IEEE Transactions on Industrial Electronics,* vol. 58, pp. 158-172, 2011.

[122] T. M. Haileselassie and K. Uhlen, "Impact of DC Line Voltage Drops on Power Flow of MTDC Using Droop Control," *Power Systems, IEEE Transactions on,* vol. 27, pp. 1441-1449, 2012.

[123] H. Zhang, F. Mollet, C. Saudemont, and B. Robyns, "Experimental validation of energy storage system management strategies for a local DC distribution system of more electric aircraft," *IEEE Transactions on Industrial Electronics,* vol. 57, pp. 3905-3916, 2010.

[124] A. M. Rahimi and A. Emadi, "Active damping in DC/DC power electronic converters: A novel method to overcome the problems of constant power loads," *IEEE Transactions on Industrial Electronics,* vol. 56, pp. 1428-1439, 2009.

[125] A. M. Rahimi and A. Emadi, "Discontinuous-conduction mode DC/DC converters feeding constant-power loads," *IEEE Transactions on Industrial Electronics,* vol. 57, pp. 1318-1329, 2010.

[126] A. Kwasinski and C. N. Onwuchekwa, "Dynamic behavior and stabilization of DC microgrids with instantaneous constant-power loads," *IEEE Transactions on Power Electronics,* vol. 26, pp. 822-834, 2011.

[127] P. Kundur, *Power system stability and control*: Tata McGraw-Hill Education, 1994.

[128] P. C. Krause, O. Wasynczuk, and S. D. Sudhoff, *Analysis of Electric Machinery and Drive Systems,* 2002.